ADDIS ABABA UNIVERSITY

ADDIS ABABA INSTITUTE OF TECHNOLOGY

SCHOOL OF CIVIL AND ENVIRONMENTAL ENGINEERING

SIMULATION OF LOAD –DISPLACEMENT RESPONSE OF PILE FOUNDATION SUBJECTED TO LATERAL LOADS AT WOLAITA SODO ELECTRIC POWER TRANSMISSION CONVERTER STATION

A Thesis in Geotechnical Stream

By HIWOT AYELE

March, 2021

Addis Ababa

ADDIS ABABA UNIVERSITY

ADDIS ABABA INSTITUTE OF TECHNOLOGY

SCHOOL OF CIVIL AND ENVIRONMENTAL ENGINEERING

This is to certify that the thesis presented by Hiwot Ayele, entitled '**SIMULATION OF LOAD -DISPLACEMENT RESPONSE OF PILE FOUNDATION SUBJECTED TO LATERAL LOADS AT WOLAITA SODO ELECTRIC POWER TRANSMISSION CONVERTER STATION**' and submitted in partial fulfilment of the requirements for the degree of **Master of Science** complies with the regulation of the University and meets the acceptance standards with respect to originality and quality.

To be signed by the examining committee

Dr. Ing Henok Fikire	_____	_____
Advisor	Signature	Date
_____	_____	_____
Internal Examiner	Signature	Date
_____	_____	_____
External Examiner	Signature	Date
_____	_____	_____
Chair person	Signature	Date

Declaration

This thesis has not previously been submitted for a degree or diploma in any university. The thesis contains no material previously published or written by another person except where due reference is made in this thesis itself.

Hiwot Ayele	_____
Name	Signature

Addis Ababa, Ethiopia	March, 2021
Place	Date of Submission

This thesis has been submitted with my approval as a university advisor

Dr. Ing Henok Fikire	_____
Advisor's Name	signature

ACKNOWLEDGMENT

I would like to express my deep appreciation to my advisor, Dr.Ing Henok Fikre, for his continuous caring and valuable guidance in the preparation of this thesis.

I would also like to thank Dr. Atalay Ayele from the Institute of Geophysics, Space Science, and Astronomy.

Thanks my classmate Tequamwork Assefa, for her friendship constructive comments, and suggestions which helped with the good of the work of this thesis.

I want deeply thank my parents for their patience, love, and continuous presence.

Finally, my dearest husband Yosef Tsegaye deserves the biggest thanks for his encouragement and support

ABSTRACT

Chi-Chi earthquake in Taiwan and the Wenchuan earthquake in China are listed among the earthquakes which cause collapse of transmission tower. Currently, in Ethiopia, there is an electric transmission tower under construction on earthquake prone area, Wolaita Sodo. This transmission tower is expected to carry electric current up to Kenya. Considering the effects that are going to be incurred if foundation failure occurs, analyzing the effect of seismic loading will be vital for this project and further constructions.

In this thesis, a 3D FEM analysis using ABAQUS software was performed to study the lateral deflection of the foundation of the above mentioned electric transmission tower using a single pile subjected to dynamic loading. 15 m long pile with varying diameters of 0.8 m and 0.6 m, keeping other parameters constant has been considered.

For the seismic loading, probabilistic seismic hazard analysis (PSHA) has been performed for the specified area. Peak ground acceleration of 0.16 g and 0.233 g has been obtained from the seismic hazard analysis for design basis earthquake and Maximum considered earthquake respectively. Acceleration time history data has been obtained from PEER ground motion database.

Layered soil with Mohor-Coulomb soil model has been used. To consider the continuity of the ground, the infinite boundary has been used. Scaled acceleration time history has been applied at the base of the model.

The dynamic response of the piles resulted in deflections of 72.02 mm and 63.7 mm for 0.6 m and 0.8 m diameter piles respectively, which exceed the acceptable limits of recommendations. Increased pile size shows reduction in deflection and increment on soil resistance. The displacement of the pile while going from top to end shows reduction and this result agrees with literatures.

TABLE OF CONTENTS

LIST OF FIGURES

LIST OF TABLES

ABBREVIATION

A	Activity rate while using the logarithm of base 10
$AS08$	Abrhamson and Silva (2008)
BNWF	Beam on Non-linear Winkler Foundation
BWF	Beam on Winkler Foundation
BEM	Boundary Element Method
$CY08$	Chiou and Youngs (2008)
CDF	Cumulative distribution function
DBE	Design Basis Earthquake
DSHA	Deterministic Seismic Hazard Analysis
EBCS	Ethiopia Building Code Standards
E_p	Young's modulus of the pile
FEM	Finite Element Method
FDM	Finite Difference method
F_{HW}	Hanging-wall flag
FHWA	Federal Highway Administration
$f_M(m)$	Probability density function for earthquake magnitude
$F_M(m)$	Cumulative distribution function for earthquake magnitude
FM	Magnitude scaling
F_{NM}	Normal faulting flag
$f_R(r)$	PDF for distance
F_{RV}	Reverse faulting flag
GMPEs	Ground motion prediction equations
GSHAP	Global Seismic Hazard Assessment Program

IMs	Intensity Measures
I_p	Second moment of area
K_h	Coefficient of subgrade reaction
L_p	Pile length
M	Moment magnitude
MCE	Maximum Considered Earthquake
MAF	Mean Annual Frequency
M_j	Discretized magnitude
M_{max}	Upper bound of earthquake
M_{maxobs}	The largest historical earthquake
Mmin	The smallest magnitude of an earthquake
Mo	Moment applied to pile at surface
NGA	Next Generation
PDF	Probability density function
PEER	Pacific Earthquake Engineering Research
PGA	Peak ground acceleration
PSHA	Probabilistic seismic hazard analysis
Qo	Lateral load
R_{JB}	Joyner-Boore distance to the rupture plane
R_k	Discretized distance
R_{RUP}	The closest distance to the rupture plane
R_X	Site coordinate (km) measured perpendicular to the fault strike from the surface projection of the up-dip edge of the fault rupture, with the down-dip direction being positive.
R_Y	The closest distance from the site to the ruptured area shear strain
Spa (f1)	Spectral acceleration

SPSI	Soil-Pile-Structure Interaction
Vs	shear wave velocity
V_{S30}	Average shear wave velocity in the top 30 m (m/s)
Z1.0	Depth to shear wave velocity of 1.0 km/s (m)
Z_{HYP}	Hypocentral depth
Z_{TOR}	Depth to top of rupture

Symbols

α	Activity rate while using natural logarithm
β	The ratio of small to large magnitude while using natural logarithm
λ	The rake angle
λ_m	Rate of earthquakes with magnitudes greater than m
λ_s	Lame's constant
ΔM	Interval range of earthquake magnitude
ΔR	Interval range of distance
δ	Fault dip angle
ν	Poisson's ratio
ω	circular frequency

1D	One dimension
2D	Two dimension
3D	Three dimension

CHAPTER 1 - INTRODUCTION

1.1 Background

Pile foundations are used to transfer super-structural loads to underlying soil or rock. Mostly deep foundations are adopted when the load of the superstructures is heavy or the bearing capacity of the soil is very low. Pile foundations are safer than other foundation types for supporting structures in seismic prone areas. These days, pile foundations are the most implemented structure in Ethiopia due to increment in the construction of high rise buildings, transmission line towers, and long span and tall bridge structures, which have very large design loads. So, as the weight of the structure increases and the bearing capacity of the soil compromises the stability, deep foundation is used.

Piles are vertical members mostly subjected to axial loads. Even though the primary function is to transmit axial loads in most cases, every pile foundation has to withstand some lateral loads. For example, pile foundations in tall buildings and transmission towers often have to withstand wind force. Earthquake is the major causes of lateral forces in addition to the surrounding soil, and the water loads.

If the load acting on the pile is axial, it is transferred to the base of the pile and through the pile shaft as base resistance and shaft or skin friction, respectively. Laterally loaded piles transfer the load to the surrounding soil mass through the lateral resistance of soil. When lateral loads are applied on the pile, the pile tries to shift in the direction of the applied load, pressing against the soil. This will generate normal stress, shear stress, and strain in the soil. The external force is resisted by the soil resistance around the pile. Failure of short pile occurs when the lateral of the soil has been exceeded. In cases of long pile , the failure associated the moment at one or more points exceeds the moment of resistance and the failures takes place by formation of hinges along the pile length. This lateral deflection of pile depends on the soil resistance and the soil resistance in turn depends on the pile deflection and this interdependence is known as soil- pile interaction.

Ethiopia is susceptible to two types of natural hazards due to the presence of rift valley: earthquakes and volcanic eruptions. Earthquakes have been a regular occurrence in Ethiopia due to its location. Kinde (2002) cited Gouin (1979), estimates 15,000 tremors occurred in Ethiopia and the Horn of Africa in the

20th century, while another study by Kebede (1966, cited Kinde et.al.,2011) identified 16-recorded earthquakes of magnitude 6.5 and higher in Ethiopia in the same period.

Most earthquakes affect tens of square kilometers while the severest can destroy areas of 2500 km^2 or more (Bell, 2002). Therefore, structures built in the destructive region of earthquakes require an assessment of wave propagation effects.

.

In this study, probabilistic seismic hazard analysis has been performed at Wolaita Sodo area. Probabilistic seismic hazard analysis (Cornell, 1968) is widely used for evaluating the seismic risk at a certain site of an engineering project, and for estimation of seismic design loads. The main goal of PSHA is to predict ground motions by integrating the probabilities of all earthquake scenarios across locations and sizes of future earthquakes.

Design Basis Earthquake (DBE) and Maximum Considered Earthquake (MCE) are the two levels of earthquake ground motion analysis normally considered in pile design and analysis (Song, 2018). The maximum considered earthquake has 2% probability of exceedance in 50 years (a return period of 2475 years) while the design basis earthquake has 10% probability of exceedance in 50 years (a return period of 475 years). Public life safety and sustained functioning of the structure are the aims for the maximum considered earthquake and the design basis earthquake respectively.

Soil-pile interaction can be kinematic and /or inertial (Kramer, 1996) (Poulos, 2013). The inertial interaction is the phenomenon in which inertial forces developed in the structure by its own vibrations generate primarily base shears, bending moments, and axial loads which in turn cause deformations in the surrounding soil surrounding of foundation system. Kinematic interaction results from the propagating nature of seismic disturbances in the form of waves, which makes the soil motion at any given instant generally different from point to point. Design of pile foundation under seismic load should include the effect of ground motion and inertial load. For such cases, dynamic soil-pile interaction analysis becomes important to assess the dynamic response of pile foundation.

1.2 Problem Statement

The electric transmission towers are an important lifeline engineering structure. Up to now, most of research attention on transmission towers have been focused on the actions of static load and wind load (Li & Bai, 2006). Even though seismic load is significant than static and wind load, only a few studies considered earthquake load. Collapse of transmission tower was observed in previous large earthquakes such as the Chi-Chi earthquake in Taiwan and the Wenchuan earthquake in China. The reason behind the destruction of transmission tower was the main failure of foundation. This study investigate the response of pile foundation under seismic excitation by considering the effect of interaction.

1.3 Objectives

1.3.1 General Objective

The main objective of this study is to investigate the effect of seismic excitation on pile foundation embedded in layered soil considering soil-pile interaction.

1.3.2 Specific Objectives

- Analyzing lateral response of pile caused by the application of the scaled ground motion.
- Investigate the effect of pile diameter on pile response.

1.4 Limitations

For the thesis work, the following limitations were identified:

- Since there are no records of accelerograms for Ethiopian earthquakes, Pacific Earthquake Engineering Research Center (PEER) records are adapted for acceleration time history selection.
- When modeling the soil as a continuum, only the finite element method and solid elements will be considered.

1.5 Methodology

In this study, the finite element software ABAQUS is used for t model development and analysis. This software is reliable in representing the soil-pile system in three-dimensional domain and also it has the capability of modeling the behavior of soil continuum.

Proper techniques and literatures are reviewed in detail to model pile and surrounding soil, along with their mesh sizes, constitutive models to represent material behavior, soil-pile interface, dynamic input, damping, and boundary conditions. A single pile foundation of 15 m long with varying diameters of 0.6 m and 0.8 m has been considered. The pile sizes are taken from Wolaita Sodo Converter Station to support electric power transmission tower. Four layered soil with size of 20 times diameter of the pile and long 30 m has been modeled. Mohr-Coulomb soil model has been used for the soil. The soil properties have been taken from geotechnical investigation report of the specified project. Material damping has been incorporated and infinite boundary has been applied to consider the continuity effect of the ground.

Ground motion analysis was carried out in five stages. In the first step, seismic source has been identified. The second step defines magnitude of earthquake using recurrence relationship of Gutenberg and Richter (1944), path parameters, to identify the effect of distance from the source to the specific site, using Kaklamanos et al. (2011) equation and identification of site parameters. The third step estimates the earthquake effect, based on the selection of an appropriate attenuation relationship or empirical ground motion prediction equations. In this study, Chiou and Young (2008) Next Generation Attenuation equation was used as recommended by Ayele (2017) for East Africa Rift. The fourth step was used to determine the hazard curve and disaggregation of the hazard at Wolita Sodo area. The final step was the selection of ground motion using disaggregation results of magnitude and distance.

1.6 Scope of Research

Soil:

The soil considered in this study was obtained from a geotechnical investigation report carried out at Wolaita Sodo and Mohr-Coulomb model is used as constitutive model for all the soil layers.

Pile Foundation and Super Structure Loads:

The pile sizes are taken from Wolaita Sodo Converter Station to support electric power transmission tower and only two diameters of pile (0.6 m and 0.8 m) have been considered. The effect of length of pile has not been varied.

Seismic data:

The applied acceleration time history has been selected for the design basis earthquake only.

1.7 Significance of the Study

The study will help to understand the load-displacement response of piles in layered soil during earthquake shaking. It will provide reliable numerical modeling of the real behavior of soil-pile interaction subjected to seismic excitations, which will lead to safer and economical design of structures.

CHAPTER 2 LITERATURE REVIEW

2.1 Introduction

Pile foundations are slender elements, under a major structure, to transfer loads from the superstructure into competent soil layers. It is subjected to static and dynamic, lateral loading generated from the superstructure, lateral earth pressure, wind, waves, and earthquake, the effect of moving vehicles or ships, plants, and equipment. The major seismic hazards like seismic shaking and ground failure impose mainly lateral loads on the pile foundations.

The analysis of laterally loaded piles is more complex than the analysis of axially loaded piles. The capacity and response of laterally loaded piles are usually assessed through non-linear load transfer analysis, using load transfer (or 'p-y') curves appropriate for the soil type. The response of pile subjected to seismic excitation depends on the pile itself, mechanical properties of the surrounding soil, the interaction between superstructure, pile, and soil and the seismic input.

This chapter present analysis methods of pile subjected to dynamic lateral loads, soil-pile interaction problems, and finite element techniques applicable to model pile-soil interaction with seismic excitation input.

2.2 Seismic Wave Propagation

A definition of a wave is motion around at a state of equilibrium. The wave is produced in the soil due to tectonic movement, movement of fault, volcanoes, explosions, and earthquakes. Seismic waves, known as waves of energy travel from Earth layers and generated by strong earthquakes, Kramer (1996).

There are two main types of seismic waves, body waves, and surface waves. Body waves travel through the inside of the Earth, but surface waves are travel along the surface of the Earth like ripples on water and these waves are the result of interaction between body waves and the surficial earth material.

There are two types of body wave's compressional waves and shear waves whereas the surface waves are classified into Rayleigh waves and love waves. P wave propagation of compression and the fastest kind of seismic wave, and it travels through solids, liquids, or gases. S-wave is the propagation of shear deformation that arrives after the primary (P-wave). Rayleigh generates from coupled P and SV waves the particle motion is always in the vertical plane, and due to phase shift between P and SV the particle motion is elliptical and retrograde (counterclockwise) concerning the direction of propagation, Love waves move the ground from side to side in a horizontal plane parallel to Earth's surface, but at right angles to the direction of propagation; so the wave motion is horizontal and transverse. Require some kind of waveguide formed by the velocity gradient. In this thesis body –wave will be used, due to the fact in the Groningen situation the surface waves have not yet been measured for the relatively shallow earthquake (Kruse and Holscher, 2010).

2.3 Soil-Pile Interaction Analyses Approach

An earthquake geotechnical engineer faces numerous challenges in foundation design for seismic excitation because of the complexity of the problem. To handle this type of problem, the earthquake geotechnical engineer needs skills in soil mechanics, foundation engineering, and soil-pile-interaction.

Figure 2.1 shows the soil-pile-interaction problem and its key features. Since the forces that result from soil-pile-interaction govern structural response, these forces should be determined with accurate analyses. Soil-pile-interaction analyses can be carried out in two ways: either by modeling the structure and soil together with appropriate interface behavior as shown in Figure 2.1 or by using the principle of superposition as shown in Figure 2.2. The superposition approach has two steps that address two different mechanisms, kinematic and inertial interaction. This approach is based on the assumption that the system remains linear. Superposition is exactly valid for linear soil, pile, and structure (Whitman, 197). However, superposition is approximately valid for moderately nonlinear systems under engineering approximations, because pile deformations due to lateral loading transmitted from the structure vanish very rapidly with depth.

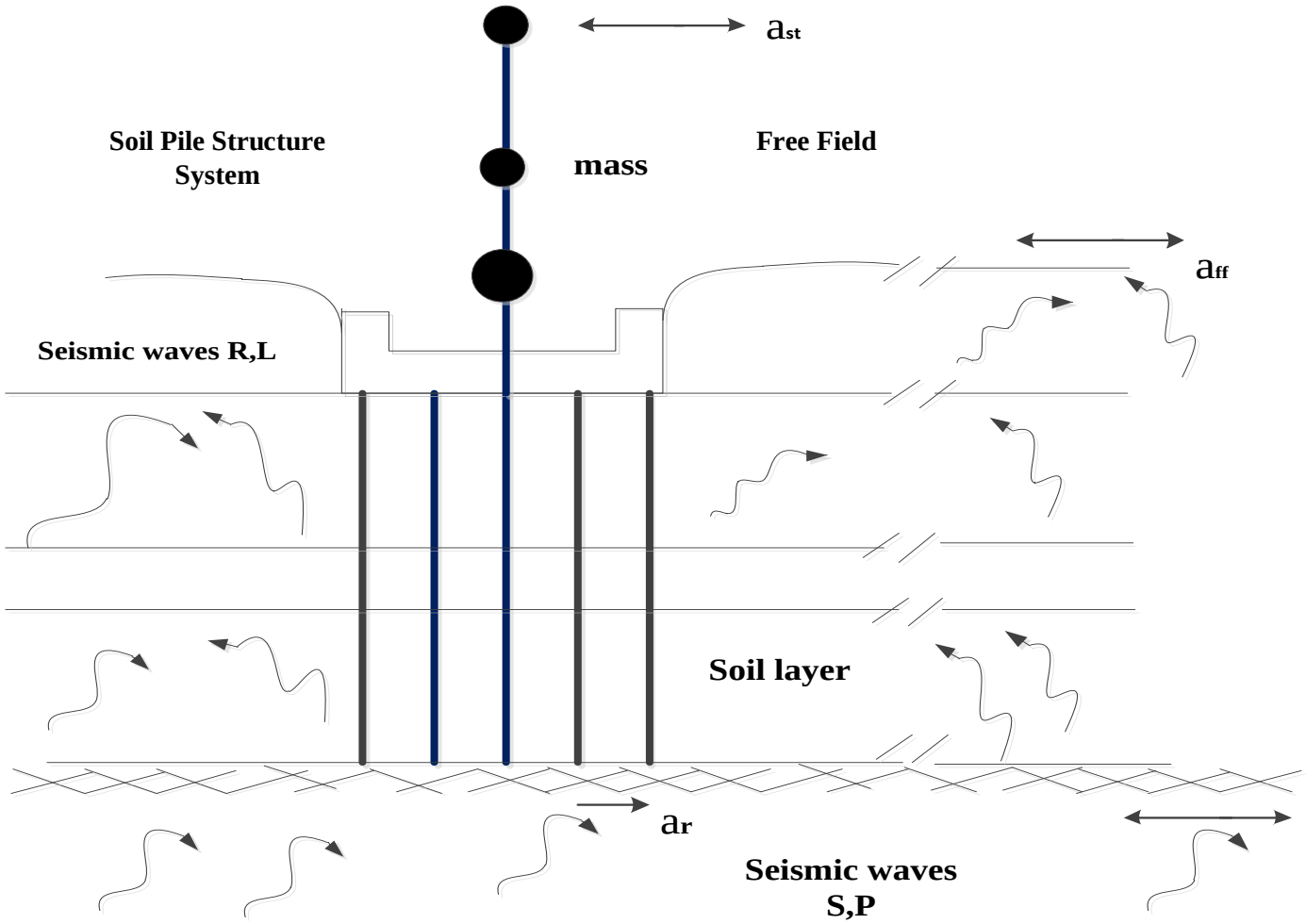

Figure 2.1: Sketch of soil-pile-interaction problems (after Gazetas and Mylonakis 1998).

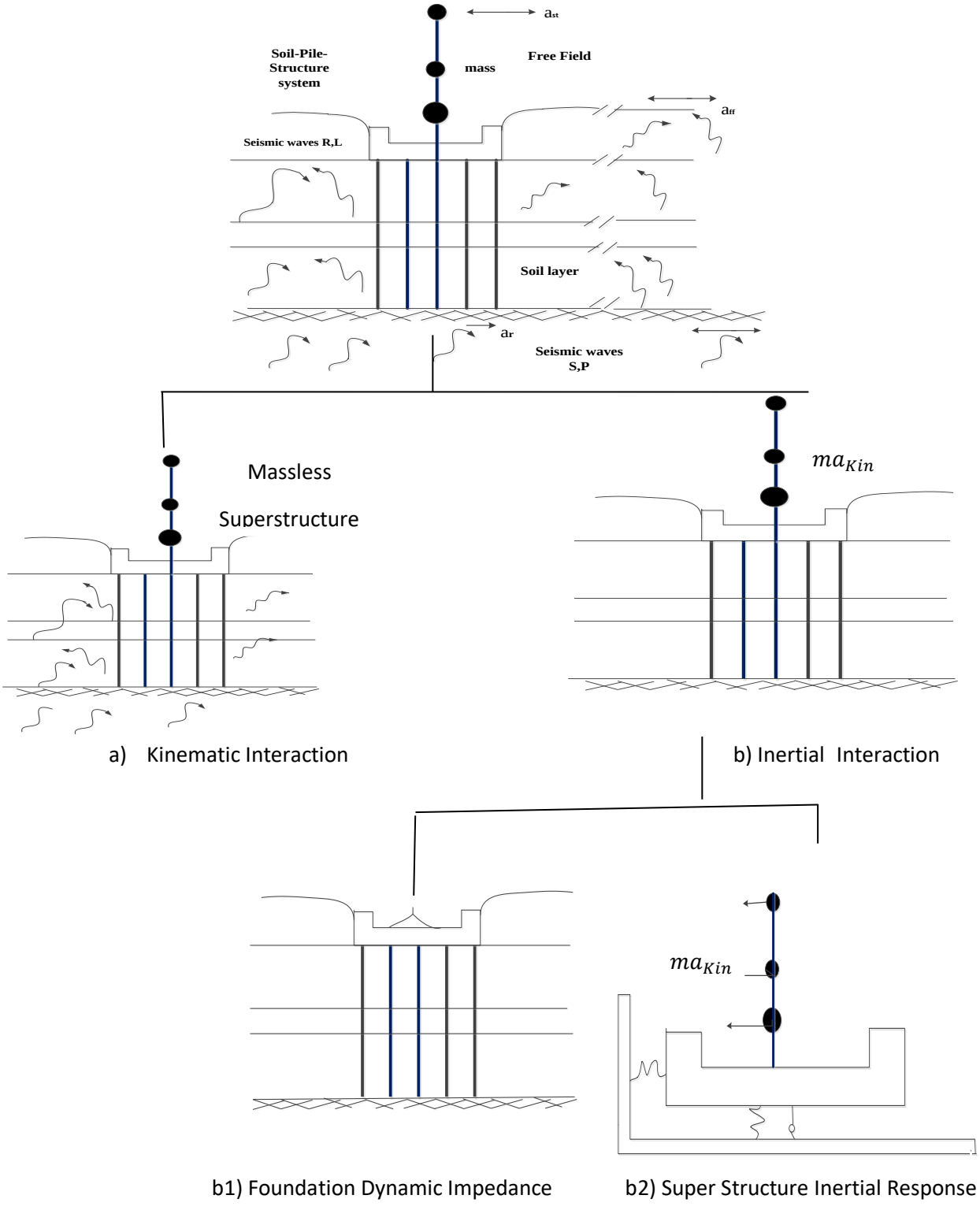

Figure 2.2: The superposition theorem for soil-pile-interaction problems a) kinematic interaction b) inertial interaction (after Gazetas and Mylonakis 1998).

2.3.1 Kinematic Interaction

In the absence of the superstructure, as shown in Figure 2.2 a, the motion of the foundation may be different from the free field motion, where "free field" refers to the motion of the surface soil that is far enough from the foundation such that the foundation does not affect the free-field motion. This difference is due to the kinematic interaction mechanism. The reasons for the observed differences are the presence of stiff foundations, wave inclination or incoherence, or foundation embedment. Kinematic effects are described by frequency dependent transfer functions. The transfer function is defined by the ratio of the foundation motion to the free field motion in the absence of a structure. Transfer functions are defined in the frequency domain. Wave passage through the foundation also generates stress in foundation elements. These stresses are termed "kinematic stresses".

2.3.2 Inertial Interaction

The motion at the foundation due to kinematic interaction forces the structure to oscillate. This, in turn, implies that the structure will produce inertial forces and overturning moments at its base. Due to this, the foundation and surrounding soil will get additional dynamic forces and displacements. This is due to the inertial interaction. The flexibility of the foundation support affects the acceleration within the structure. The flexibility of the foundation and the damping associated with foundation-soil interaction can be described by a frequency dependent foundation impedance function (dynamic impedance). The dynamic impedance can be simulated by the effects of a "spring" and a "dashpot" acting at the base of the structure in place of the foundation elements.

The above two mechanisms occur simultaneously with only a small time lag. In the two-step approach, the acceleration at the top of the foundation is obtained by modifying the free-field motion to account for kinematic effects. This motion, akin, is then used as an input motion for the analysis of inertial interaction. For computational convenience, the analysis of inertial interaction is further subdivided into two steps, as shown in Figures 2.2 b1 and 2.2 b2. First, a dynamic impedance function at the top of the foundation is computed for the pile-soil system. As a final step, the superstructure, supported on the spring and dashpot system is analyzed using a_{kin} as the input motion.

Typically, structural design engineers neglect the kinematic interaction. This is acceptable in some circumstances such as at low frequencies (Mamoon and Ahmad 1990) and for shallow foundations with vertically propagating shear waves or dilatational waves. However, Gazetas (1984) carried out analysis on flexible piles with low frequency loading and concluded that kinematic interaction is also important. In almost every seismic building code, structural response and foundation loads are computed by fixed base analysis; that is, neglecting soil-pile -interaction.

2.4 Pile Subjected to Under Dynamic Lateral Loads

This section explains the dynamic loading condition and the analysis methods of piles when exposed to dynamic loads. Dynamic load act on piles due to earthquake forces, wave forces, wind forces, and machine it may be transient or cyclic loading. This paper assumes the dynamic loads come from earthquake, the ground vibration is generated by an earthquake due to the upward transmission of seismic waves from a stiff soil layer to the soft soil layer.

The pile is exposed to kinematic loading and inertial loading by causes of earthquake: Kinematic loading is related to the deformation of the pile due to the effect of an earthquake. The deformation of the pile is occurring because of the stiffness difference between the soil and the pile. Secondly, there is inertial loading are induced in the piles because of the accelerations generated within the structure by the earthquake. Consideration is generally confined to lateral inertial forces and moments, which are assumed to be applied at the pile heads. Poulos (2013). The stiffness of the foundation influences the natural frequency of the structure, and, therefore, the susceptibility to resonance and dynamic amplification during cyclic loading.

2.5 Available Analysis Methods for Dynamic Lateral Loading of Piles

In this section, methods of modeling the dynamic behavior of a single pile under lateral loads are explained. These are Beam on Non-linear Winkler Foundation (BNWF), Continuum Methods, and Boundary Element Method (BEM), and Finite Element Method (FEM).

2.5.1 Winkler Model

In 1867, Winkler proposed this model, which was introduced as Beam on Winkler Foundation (BWF). This model characterizes the soil as a series of independent linearly elastic spring, soil-pile contact at any point along the pile length, there is a relationship between deflection and forces, and the contact stress at other points is independent.

(Hetenyi, 1946) presented analytical solutions for beams on a foundation with a fourth-order differential equation governing the beam deflection (Eq.2.1). The input parameters of the solution are the length and elastic modulus of the beam, the spring constant of the foundation (soil), and the magnitude and distribution of the applied load (Figure 2.3). At the end of the solution, shear force, bending moment, and deflection along the span of the beam can be found.

$$EI\frac{d^4y}{dx^4} + ky = q \qquad 2.1$$

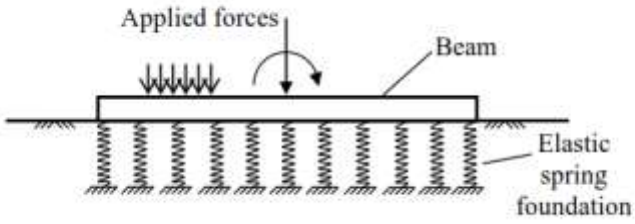

Figure 2.3: Beam on an elastic foundation

The beam-on-Winkler foundation approach can also be called the subgrade-reaction approach because the foundation spring constant can be related to the modulus of subgrade reaction of a soil mass (Terzaghi, 1955). Terzaghi suggested values of the subgrade modulus that can be used in the standard beam equation, which is used to compute bending moment and deflection.Vesic (1961) presented an elastic solution of infinite beams on elastic isotropic sub-grades acted upon by concentrated loads and obtaining the analytical solutions (contact pressure, shear force, bending moment, and deflection). He suggested the Winkler model is given an accurate result for long beams by comparing his solution with the Winkler method solutions. Therefore, the Winkler model gives an accurate result for the sub-grade reaction modulus under moderate and infinite length beams. Kagawa (1992) presented dimensional

analysis to evaluate factors affecting the sub-grade reaction modulus Kh and suggesting a procedure to obtain constant (average) soil reaction as a function of the Soil Young's Modulus which can be used for the analysis of the Beam Winkler Foundation.

Novak (1974) used generalized Winkler model to simulate the dynamic soil-pile interaction system. The analysis is done based on linear elasticity of the soil-pile system. The analytical approach is to establish the dimensionless parameters of the problem and obtain closed-form formulas for pile stiffness and damping. In Novak analysis, all components of the motion in a vertical plane were considered, i.e. horizontal and vertical translations and rotations of the pile head.

This model is assumed that both piles and soil can treat as nonlinear manner during the exciting, since the seventies, Matlock et al. (1978) extended the concept of BNWF to seismic analysis, develop the analysis of the dynamics program SPASM8, and explaining the use of p-y methods for the lateral stiffness of soil-pile model used for seismic analysis. Wang et al. (1998), Polam et al., 1998 and Hutchinson et al., 2004 were used p-y element models for dynamic analysis. According to p-y models, cyclic soil degradation should be using. For executing this analysis, the common linear modal analysis should be replaced by an iterative nonlinear time domain analysis, as expected non-linear response cannot be feasible by linear modal analysis (Brown et al., 2001).

Kagawa and Kraft (1980) developed a Nonlinear Dynamic Winkler Foundation model (BNWF) for soil-pile-structure interaction. This method was included the method to determine seismic p-y relationships and a liquefaction model that is appropriate to the pore pressure evaluation for earthquake-type irregular loadings. In Kagawa and Kraft (1981), the nonlinear soil model was formulated as an effective stress model, and cyclic degradation of soil resistance was governed by pore pressure generation.

The BNWF method is used for nonlinear Soil-Pile-Structure Interaction (SPSI) some authors have proposed that Winkler Model represents a continuum model on the assumption of soils is an isolated horizontal plane under a plane strain condition of stress. These solutions are considered a very good estimation of the real 3D behavior at very low frequencies relative to the fundamental resonant frequency, as explained by Nogami and Novak (1980). Nogami and Koganai (1988) developed a time-domain method to estimate the flexural response of linear single piles subjected to dynamic loads by

adopting Winkler assumption, the soil assumed as plane strain horizontal thin layer, with a series of springs and dashpots (as shown in Figure 2.4,2.5).

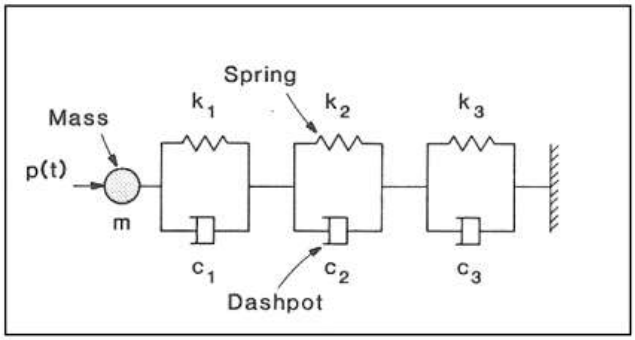

Figure 2.4: Winkler Soil Model for Lateral Pile Shaft Response (Nogami & Konagai, 1988)

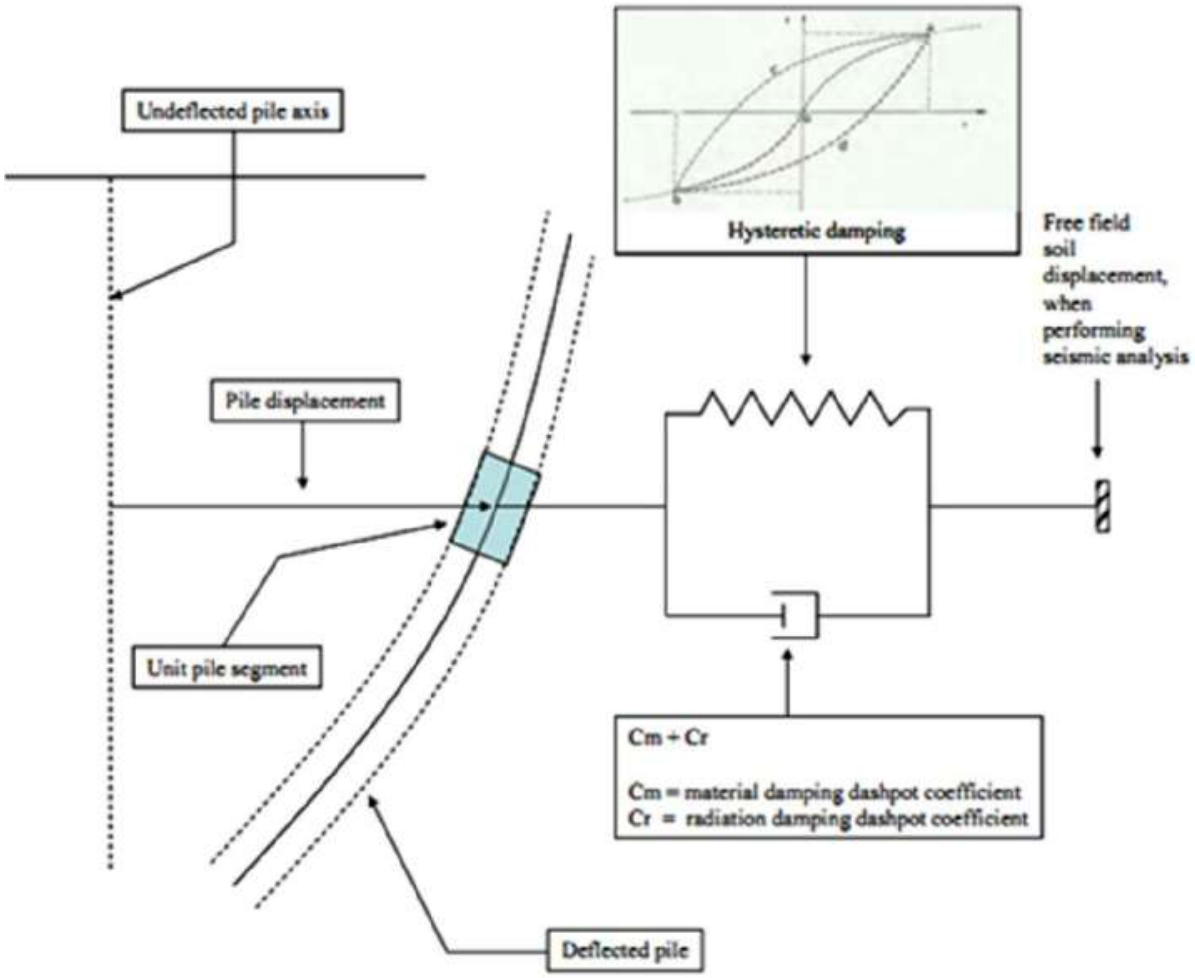

Figure 2.5: Beam on Nonlinear Winkler Foundation model with Different Damping Influences (Nogami & Konagai, 1988)

Nogami et al. (1992) proposed the nonlinear dynamic analysis for the soil-pile interaction model, by dividing the soil medium into two regions in the near field region around the pile shaft as shown in Figure 2.6. Where strong nonlinear soil response occurs, is modeled by a nonlinear spring and a gap element. The far-field region, where the behavior is linearly elastic, is modeled by the series of springs and dashpots presented by Nogami and Koganai (1988).

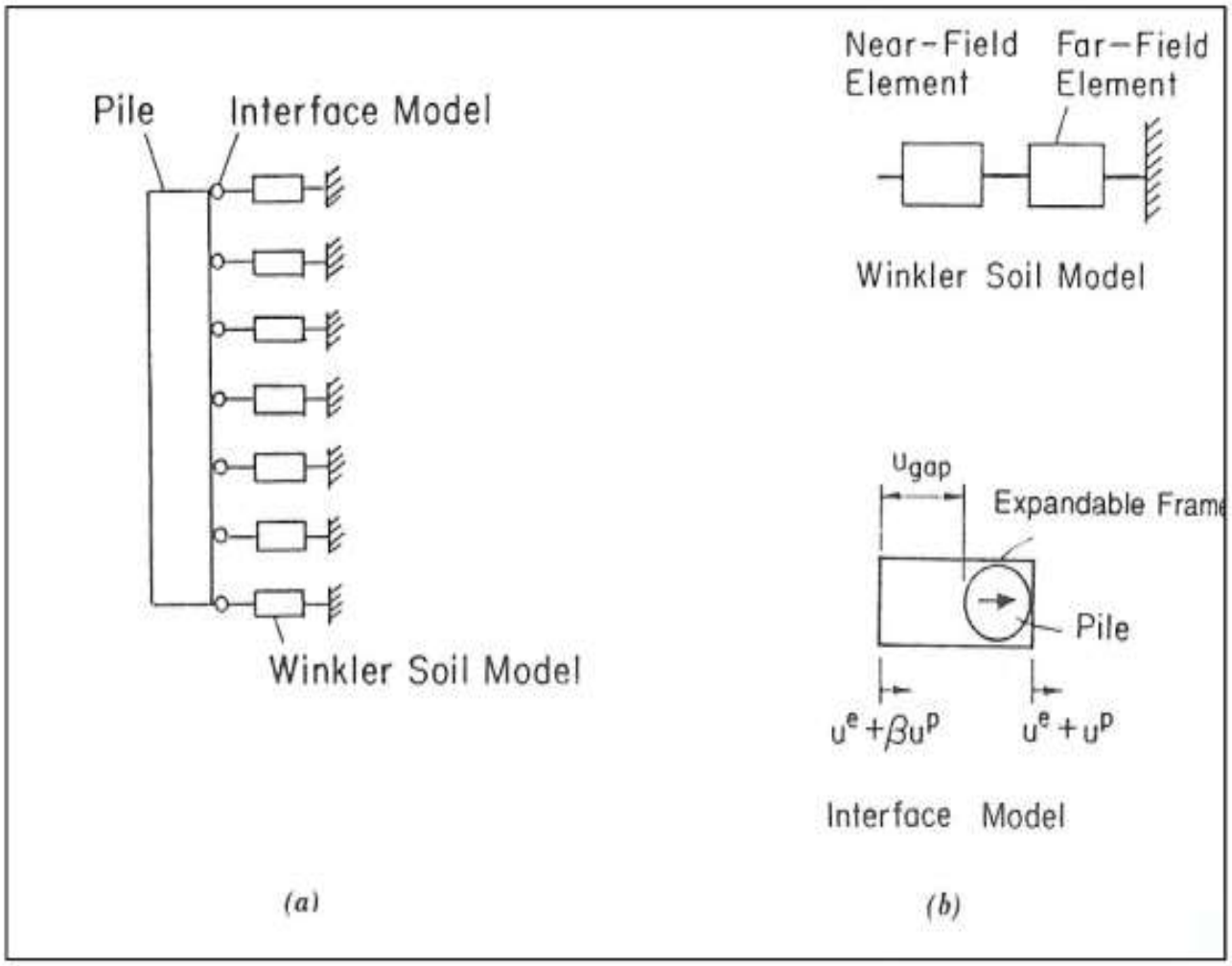

Figure 2.6: Schematic View of Soil-Pile Interaction Mode (Nogami, et al., 1992)

The major disadvantage of the beam on foundation method is the two-dimensional simplification of the soil-pile contact which ignores the radial and three-dimensional component of interaction.

2.5.1.1 p-y Curves

Design engineers often prefer to use the Beam-on-Dynamic-Winkler-Foundation (BDWF) model for design purposes rather than the FE method or elastic continuum solutions. BDWF methods use traditional semi- empirical p-y curves such as those developed by Matlock (1970) and Reese et al. (1974). These curves represent the nonlinear soil behavior by a series of nonlinear springs, where the *p* refers to soil pressure per unit length of pile and the *y* refers to deflection. The loading in the pile is traditionally applied as a factored static load at the pile-top. This review focuses on p-y curves developed within this approach that is, obtained from static tests. It is important to note, however, that pseudo-static loading may be correct for low frequency vibration design, but response may change significantly when seismic loading generates the introduction of soil nonlinearity, damping, and pile-soil interaction. Other authors (Naggar and Novak 1996, Brown et al. 2001) have developed p-y methods that can deal with dynamic loading.

Most of the existing standard p-y curves were developed based on full-scale lateral load tests on a relatively small range of pile diameters. However, Juirnarongrit (2002) showed that in dense weakly cemented sand, the pile diameter effect on the p-y curves at displacement levels below the ultimate soil resistance is insignificant. Bey5ond this range, an increment in the pile diameter increases the ultimate soil resistance. Existing p-y curves predict the response of the laterally loaded piles well in weakly cemented sand but are inappropriate for large diameter piles. These existing p-y curves have been incorporated into commercial programs such as COM624P (Wang and Reese 1993), LPILE (Reese et al. 2000), and FLPIER (University of Florida 1996). Deflection and moment along the pile can be found for a given load by using these commercial programs. The literature review presented herein focuses on the existing p-y curves for laterally loaded piles and methods to find p-y curves from numerical analysis.

2.5.2 Continuum Model

Continuum approach, analysis of laterally loaded piles are done by treating the surrounding soil of pile as a three-dimensional continuum. Continuum approach is attractive because the interaction of pile and surrounding soil is conceptually more attractive than the beam-on-foundation approach. After all, the interaction of the pile and the surrounding soil is in reality three dimensional. The main advantage of

continuum models is modeling the effect of radiation damping, the disadvantage of the model is only practicable for visco-elastic material.

This method is extremely useful to obtain a better understanding on the soil-pile interaction phenomenon and to obtain analytical expressions of parameters such as the sub-grade reaction modulus (Vesić, 1961), that can be used in the Winkler models.

Tajimi (1966) describes a dynamic soil-pile interaction solution based on elastic continuum theory. He used a linear Kelvin-Voigt visco-elastic stratum to model the soil and ignored the vertical components of the response.

In 1974, Novak developed an approximate continuum model to explain soil-pile interaction. The soil is assumed as a group of independent thin infinite horizontal layers that extended to infinity. As each plane is considered independent, this model may be viewed as a generalized Winkler model.

Nogami and Novak (1980) investigated the coefficients of dynamic soil reaction to pile motion treating the soil as a three-dimensional continuum, to compare with Winkler model (where the soil is modeled as discrete springs and dashpots).

One of the first applications of finite element analysis to piles was done by Yeigan and Wright (1973) who introduced two-dimensional nonlinear soil models to analyses elastic piles. They have used the model to develop the lateral soil resistance –displacement relationships (p-y curves) for pile foundations.

The advantage of the finite element approach is used in the analysis of the soil-pile interaction model of pile and pile groups with a superstructure response even if in dynamic loading conditions. The finite element is model the soil profile as 3-D and analyses the effect. Soil is treated as a continuum mass in the finite element method. Randolph (1981) presented the results of his parametric studies on the response of laterally loaded piles embedded in an elastic soil continuum. The finite element modeling result is fitted with algebraic equation solutions. Wu & Finn (1997) used a quasi-3D finite element program for the analysis of dynamic soil–pile–structure interaction. An eight-node brick element is used to represent the soil continuum, and a two-node beam element is used to simulate the piles.

Currently, the most useful continuum based method of analaysis available method. Several investigators are done different forms of the finite element method. Desai and Appel (1976) presented a three-dimensional finite element solution with interface elements for the laterally loaded pile problem. Kooijman and Vermeer (1988) used a quasi-dimensional analysis for the analysis of pile-soil contact on elastoplastic soil behavior. Bhowmik and Long (1991) developed two-dimensional and three-dimensional finite element models that used a bounding surface plasticity soil model and provided for soil-pile gapping. Brown and Shie (1991) used a three-dimensional finite element model to analyze the group effects on the modification of p-y curves. Bransby (1999) used two-dimensional finite element analysis to develop a p-y curve at different depths of infinitely long pile embedded in undrained soil, and the soil behavior linear elastic soil and power-law soil.

Bentley & El Naggar (2000) implemented a finite element model by modeling the soil as a homogeneous elastic medium and to evaluate the effect of soil they were using the Drucker-Prager failure criteria. They are applying the dynamic load in the horizontal direction at the bottom of the model, and discontinuity conditions at the pile-soil interface by introducing a contact element that enables to slippage gapping.

Bentley & El Naggar (2000) studied the effects of kinematic interaction on the input motion at the foundation level. The 3-D model used in their study is shown in Figure 2.7. In this study, they included pile-soil separation, slippage, soil plasticity, and 3-D wave propagation. By considering the symmetry one half of the actual model was developed in order to reduce the computing time. Kelvin elements were used to simulate the infinite soil medium. Soil was modelled as linear and elastoplastic material using the Drucker-Prager failure criterion. Liner elastic cylindrical piles were considered for this study. Two different types of soil-pile interfaces were considered either as perfectly bonded soil-pile interface and frictional interface. The Coulomb frictional model was used to incorporate the frictional interface behavior. Two recorded earthquake motions were used at the base of the model to simulate the seismic motion in the model. The authors have concluded that the elastic kinematic interaction for a single pile slightly amplifies the free field transfer function, i.e. the ratio of soil to bedrock motion.

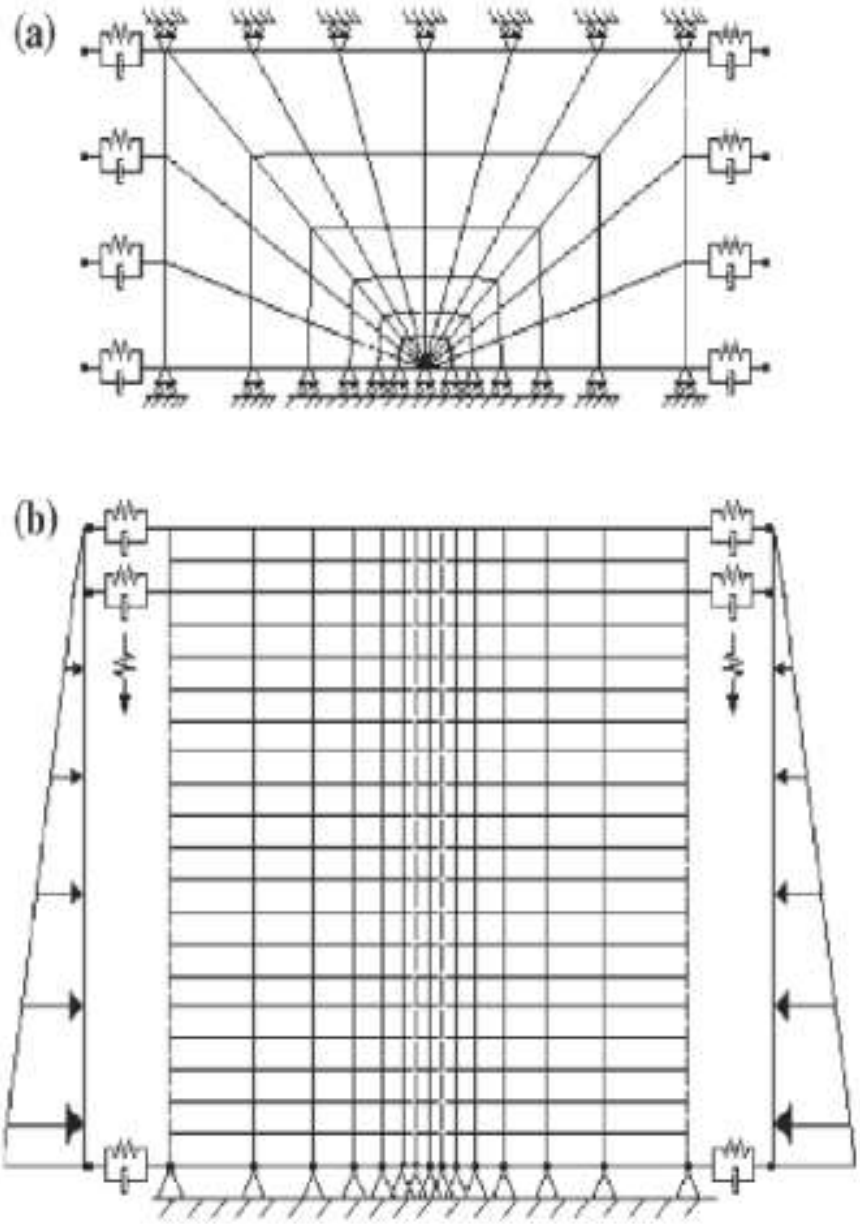

Figure 2.7: 3-D FEM model used by Bentley and Naggar [2000] a) Plan view b) Front cross sectional view

Maheshwari et al. (2004) used a 3D FE model to obtain the pile response under seismic excitation and a load applied to the pile cap and column base, considering the nonlinearity effects of the soil material and pile-soil interaction in the dynamic behavior of a single pile and pile groups. Figure 2.8 shows one of the FE mesh.

Boundary Element Method (BEM) has been used in the laterally loaded piles in evaluation. Ben Jamma and Shiojiri (2000) analyzed the dynamic behavior of a single pile embedded in an infinite half-space and the pile-soil system by the mixing of the finite element method and a hybrid thin layer element. Basile (2003) identify the advantage of the boundary element method for soil-pile interaction modeling and evaluation.

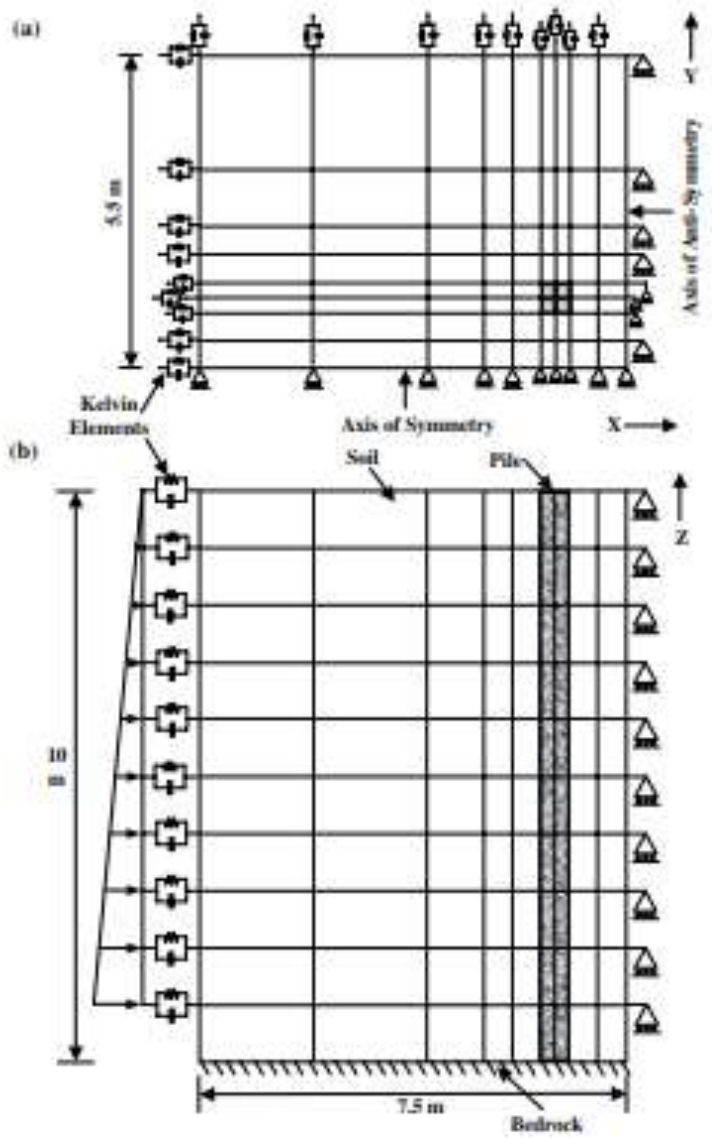

Figure 2.8: Finite element model for the pile group system: (a) Top plan (b) Front elevation with initial pressure distribution (Maheshwari et al., 2004);

2.6 Finite Element Method Applied to Soil-Pile Interaction Problems

The literature review on this section concentrated on finite element method applied to soil-pile interaction problems and the corresponding modelling techniques.

2.6.1 General Modelling Details

Mostly soil-pile interaction problems modeled by using finite element method were based on 3-dimensional technique. From this time almost all the studies used an eight-node brick element to model the soil. And also, piles were modeled using either 3-D beam elements or eight-node brick elements.

2.6.2 Boundary Conditions

In static analysis, the fixed boundary can be applied at small distance far from the interest area. However, in dynamic analysis, fixed boundary conditions cause the reflection of outward propagating waves, effectively deceiving energy inside the model. Larger size of soil model can minimize this problem because material damping will absorb most of the energy in the waves reflected from finite boundaries. However, the increase in model size implies an excessive increase in computational time and need extra memory.

To model, some special non-reflecting boundary conditions have to be defined at the lateral boundaries. This will account for the fact that in reality, the soil should have to be modeled as a semi-infinite medium. These types of boundary conditions are described below.

2.6.2.1 Quite Boundary

2.6.2.1.1 Viscous Elements (Dashpot Elements)

For the first time viscous elements were proposed by Lysmer and Kuhlemeyer (1969) for the dynamic analyses of shallow foundations. The dashpot is used instead of applying fixities in a certain direction and used to absorb energy reaching the boundary.

The use of viscous boundaries in ABAQUS is based on the method described by (Lysmer and Kuhlmeyer, 1969). The normal and shear stress components of the dashpot in perpendicular and tangential directions to the boundary can be calculated by Equation 2.2 and Equation 2.3.

$$\sigma_n = C_1 \rho_s V_p u_x \qquad 2.2$$

$$\tau = C_2 \rho_s V_s u_y \qquad 2.3$$

Where, ρ_s is the mass density of soil, V_p is the pressure wave velocity, V_p is the shear wave velocity, u_x is the normal particle velocities, u_y is the tangential particle velocities C_1 and C_2 are dimensionless parameters to modify the effect of the absorption. Viscous dashpots are used often in site response and soil-pile interaction problems (e.g., Rodriguez-Marek and Bray 2005, Wu and Finn 1997, among others).

2.6.2.1.2 Kelvin Elements

A Kelvin element consists of a spring and a dashpot attached in parallel is shown in Figure 2.9. Kelvin elements can be attached to a boundary in order to simulate an infinite medium during static and dynamic analyses.

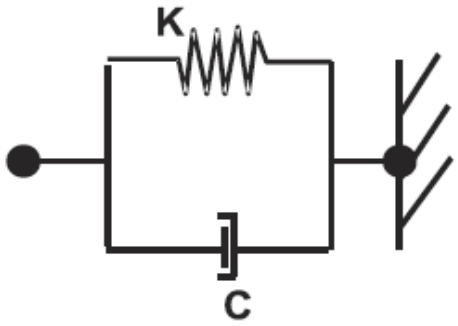

Figure 2.9: Kelvin element

The constants of the spring and dashpot of the kelvin element in the horizontal direction was calculated using the equation given by Novak and Mitwally (1988)

$$K_r^* = \frac{G}{r_o}[S_1(a_r, v, D) + iS_2(a_r, v, D)] \quad 2.4$$

Where K_r^* = total stifhess, G = soil shear modulus, r_o = distance to finite element boundary, S_1 and S_2 = dimensionless parameters, v = Poisson's ratio, a_r = dimensionless frequency ($a_r = \frac{r_o \omega}{V_s}$ where, ω is the angular frequency of excitation and V_s is the shear wave velocity of soil)

1. The medium is linear, homogeneous, and isotropic with hysteretic, frequency independent maternal damping.
2. The cylinder (pile) is circular, massless, and infinitely long and is welded to the medium.
3. The displacements are small and uniform along the cylinder; and
4. The vibration is harmonic.

The real and imaginary parts of Eq. 2.5 and 2.6 represent the stiffness and damping, respectively,

$$K_r = \frac{GS_1}{r_o} \quad 2.5$$

$$C_r = \frac{GS_2}{\omega r_o} \quad 2.6$$

2.6.2.1.3 Infinite Elements

Infinite elements are used in boundary value problems with unbounded boundaries (infinite medium) or problems with a smaller region of interest compared to the surrounding medium. Infinite elements are usually used in conjunction with finite elements. The behavior of the infinite element is similar to the behavior of the Kelvin element, but far nodes are not allowed to move. An infinite element behaves linearly. During static analyses, infinite elements will provide stiffness at the finite element model boundaries based on the model of Zienkiewicz et al. (1983). During the dynamic analysis, infinite elements will provide "quiet" boundaries at the finite element model boundaries based on the model of Lysmer and Kuhlemeyer (1969).

2.6.2.2 Free Field Boundary

Free field boundaries are normally used to determine the response of site and pile foundations subjected to seismic excitation. If the material damping of the soil is high, free field response can be achieved using a reasonably small distance from the structure to the edge of the model. However, when the material damping is low, free field responses are difficult to achieve with a limited distance from the model structure to the edge of the model. An alternative approach is to enforce the free-field motion in such a way that boundaries act as an absorbing mechanism. This can be modeled by coupling viscous dashpots between main model nodes to soil column nodes at the edges, which represents the free-field motion. The side boundary nodes of the main model and the soil column must have matching coordinates. However, this boundary condition only applies if the sides of the main model are vertical. This type of boundary condition has been used by researchers in seismic analysis of soil-pile interaction.

2.6.3 Soil-Pile Interface

The modeling of soil-pile interface give detail behaviors of the soil-pile system. The soil-pile interfaces are commonly modeled either as a perfectly bonded or as a frictional interface where soil-pile slipping and gapping may occur. Due to high computational time and convergence problem slipping and gapping interface is not applicable, most researchers consider a perfect bonding. Generally, Coulomb's law of friction is used to model slipping and gapping in FEM (Balendra, 2005). If the interface is in full contact, full transfer of shear stress is ensured. Plastic slipping will occur when the friction stress exceeds the minimum of a user specified maximum shear stress or the friction stress due to the normal stresses at the interface. Separation will occur when there is tension between soil and pile interface. Besides the Coulomb friction model, there are other proposed interface models available in the literature (Villaverde, 2009) (Desai, et al., 1984).

2.6.4 Numerical Accuracy and Stability

The numerical simulation of dynamic SSI is controlled by two main parameters. There are the spacing of the nodes of the finite element model (Δh) and the length of the time step Δt. Assuming that the numerical method converges toward the exact solution as Δt and Δh go toward zero the desired accuracy

of the solution can be obtained as long as sufficient computational resources are available. To represent a traveling wave of a given frequency accurately about 10 nodes per wavelength are required. Fewer than 10 nodes can lead to numerical damping as the discretization errors certain peaks of the wave (Jeremic & Preisig, 2005).

The recommended formula relating grid spacing (Δh), time step of analysis (Δt), smallest wave velocity of soil medium (v) and the highest relevant frequency (f_{max}) that is present in the model needs to be found by performing a Fourier analysis of the input motion as given in equation 2.7 and 2.8

$$\Delta h = \frac{v}{10\, f_{max}} \qquad 2.7$$

$$\Delta t = \frac{\Delta h}{V} \qquad 2.8$$

Where V is the highest wave velocity

2.6.5 Damping

If an un-damped structure is allowed to vibrate freely, the magnitude of the oscillation is constant. In reality, however, energy is dissipated by the structure's motion, and the magnitude of the oscillation decreases until the oscillation stops. Every non-conservative system shows some energy loss that is attributed to material nonlinearity, internal material friction, or external (mostly joint) frictional behavior. This energy dissipation is known as damping. Damping is usually assumed to be viscous or proportional to velocity. In soil dynamics two kinds of damping properties can be estimated which decline the wave; namely, material damping and geometrical damping.

2.6.5.1 Material Damping

All materials possess a form of internal damping that makes them dissipate energy when distorted. Therefore as a wave spreads out from its source, the transmitted energy and the displacement and stresses induced at points far from the source will be dramatically reduced. Material damping in dynamic calculation is caused by viscous properties of soil, friction, and the development of irreversible

strain. In the simulation of dynamic response of system, it is common practice to use Rayleigh damping in mathematical models to take care of the material damping:

$$[C] = \alpha[M] + \beta[K] \qquad 2.9$$

Where, $[C]$ Damping matrix, Mass matrix,$[M]$, Stiffness matrix, $[K]$, α, β are constants to be determined taking account the damping ratio and frequency of the first few modes.

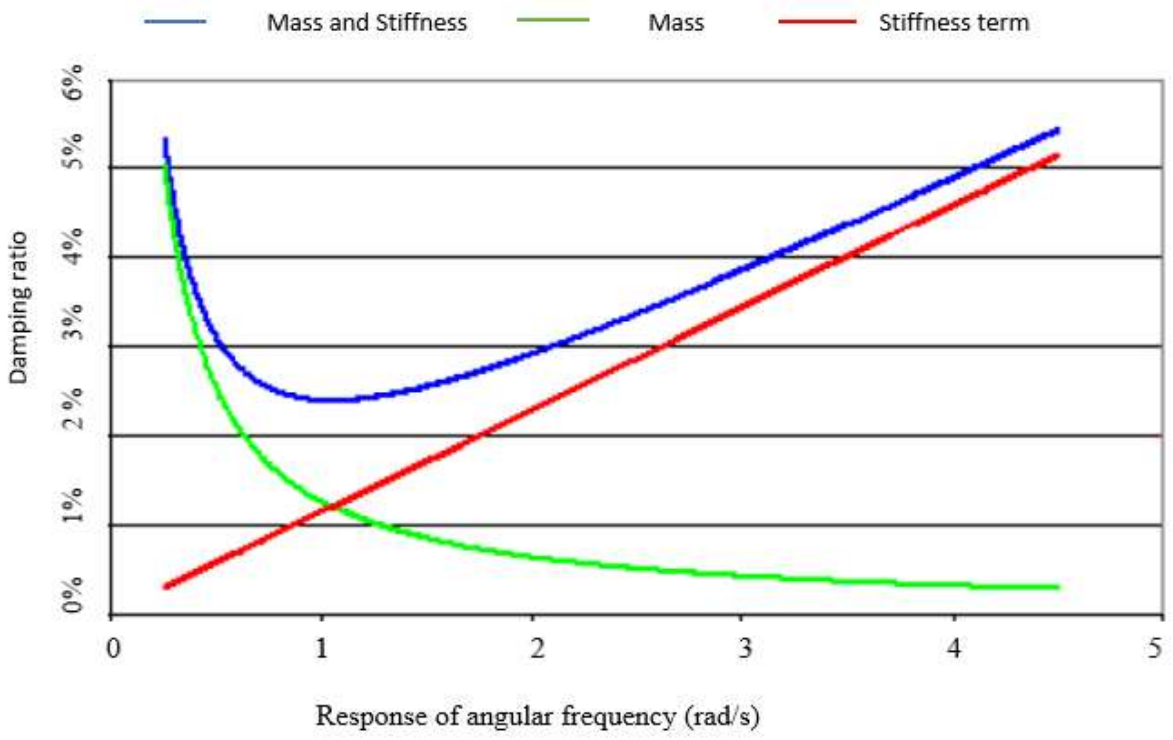

Figure 2.10: Contribution of mass and stiffness damping terms to the overall damping ratio (Balendra, 2005)

Figure 2.10 illustrates the contribution of mass and stiffness damping terms to the overall damping ratio. Here, the stiffness proportional term contributes damping that is linearly proportional to response frequency and the mass proportional term contributes damping that is inversely proportional to response frequency.

2.6.5.2 Geometric Damping

Generally, a wave propagates equally in all directions meaning that the volume of material affected simultaneously by the wave, increases with the distance traveled by the wave. The wave interacts or creates disturbance with volume of material and release a certain amount of energy and of course, this absorbed energy per unit volume get reduced with increasing distance from the source of the wave, and hence displacement amplitude and stress decrease accordingly. This type of damping due to the dispersion of wave energy over an increasing volume is known as geometric or radiation damping (Julyk, et al., 1993).

2.6.6 Selection of Mesh Size

The size of the mesh was mainly dependent on the loading conditions (static or dynamic) and the geometry of the piles. The mesh near to the pile is very fine to account for the severe stress gradients and plasticity encountered in the soil.

The selection of the dimensions of the discretized model and the element size was in agreement with the maximum wavelength (Kramer, 1996). They proposed that the maximum element size should satisfy in Equation 2.10

$$l_{max} = \frac{\lambda}{8} \sim \frac{\lambda}{5} \qquad 2.10$$

2.6.7 Soil Behavior

Constitutive behavior of soil model is important in soil-pile interaction analysis. Better results of finite element analysis are depending on the proper selection of constitutive models. Generally, there are two types of soil models that are used in finite element analyses of soils. They are linear elastic and elastic-plastic models such as Mohr-Coulomb, Drucker-Prager and Cam Clay.

2.6.7.1 Elastic Material Models

The elastic behavior can be linear and nonlinear. The linear elastic constitutive model (Hooke's law) is the most common model to approximate a material stress-strain relationship. Hooke's law relates the stress and strains through two constants, Young's modulus (E) and Poisson's ratio(v).

2.6.7.2 Elastic-Plastic Material Models

Elastic-plastic models provide a better representation of the real soil behavior. These models are based on the assumption that the principal directions of accumulated stress and the incremental plastic strain are coinciding. They require a yield function that separates elastic from elastic-plastic behavior and a plastic potential (or flow rule) which prescribes the direction of plastic straining. The two elastic-plastic material models which are commonly used to simulate soil behavior are explained below.

2.6.7.2.1 State of Stress Tensor

The state of stress for three-dimensional points is defined by a matrix containing nine stress components as shown in Figure 2.11. The nine components of the stress are represented by stress tensor (stress matrix). Stress tensor which can be defined as:

$$\sigma = \begin{bmatrix} \sigma_{xx} & \tau_{xy} & \tau_{xz} \\ \tau_{yx} & \sigma_{yy} & \tau_{yz} \\ \tau_{zx} & \tau_{zy} & \sigma_{zz} \end{bmatrix} \qquad 2.11$$

The shear stresses in the stress tensor have the following relationships due to static equilibrium as follows:

$$\tau_{yx} = \tau_{xy}; \tau_{zx} = \tau_{xz}; \tau_{yz} = \tau_{zy} \qquad 2.12$$

As a result the stress tensor is composed of six independent components. These components are called normal stresses $\sigma_{xx}, \sigma_{yy}, \sigma_{zz}$ and shear stress $\tau_{yx}, \tau_{zx}, \tau_{zy}$

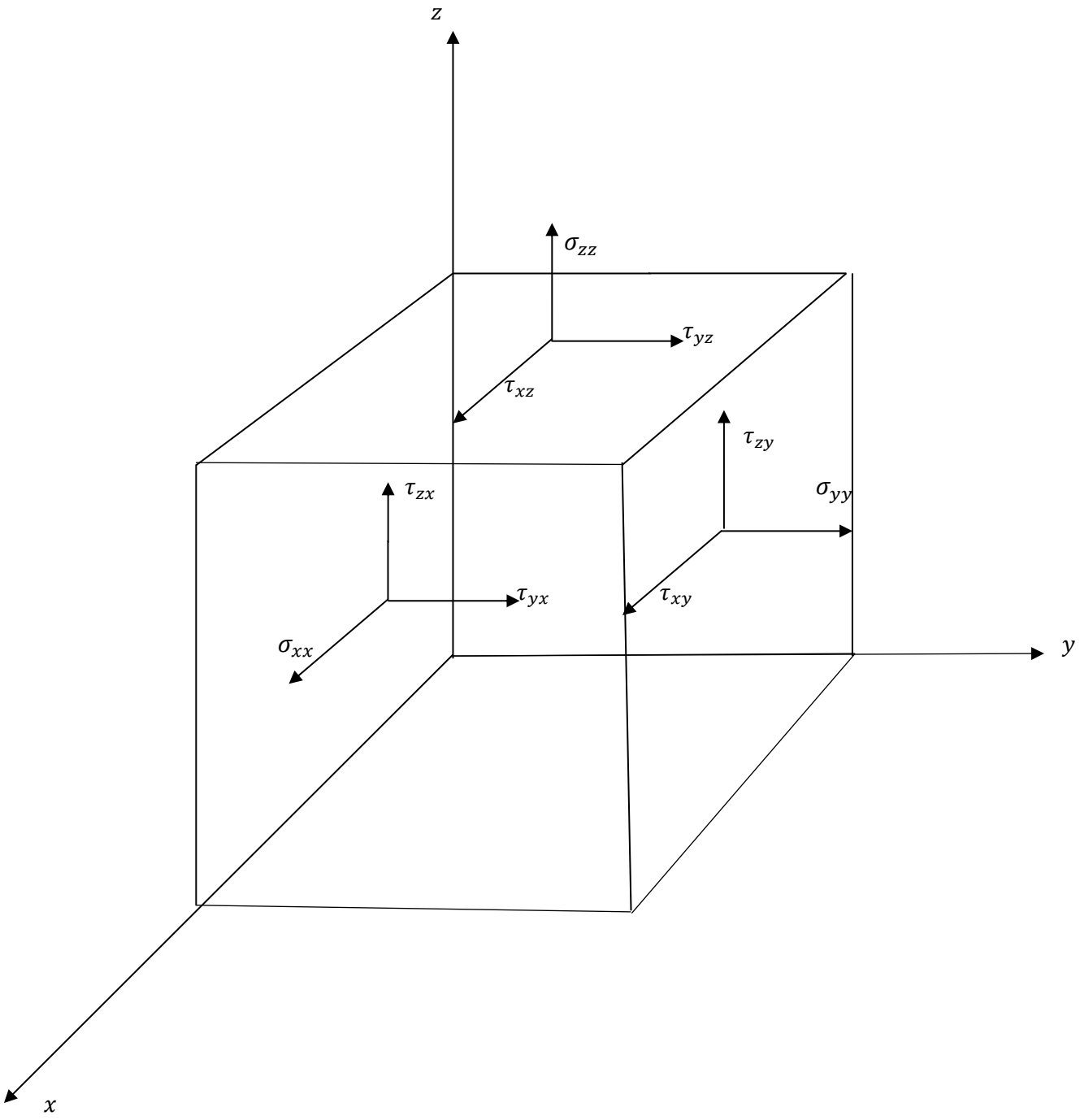

Figure 2.11: Stress state for three-dimensional elements

2.6.7.2.2 Principal Stresses

The state of stress at a point can also be defined in terms of principle stresses. σ_1, σ_2 , and σ_3. The principal stresses are related to the components of the stress tensor by the following equation:

$$\sigma^3 - I_1\sigma^2 + I_2\sigma + I_3 = 0 \qquad 2.13$$

Where I_1, I_2 and I_3 are known as the first, second, and third stress invariant respectively.

These stress invariants are defined as follows:

$$I_1 = \sigma_{xx} + \sigma_{yy} + \sigma_{zz}$$
$$I_2 = \sigma_{xx}\sigma_{yy} + \sigma_{yy}\sigma_{zz} + \sigma_{zz}\sigma_{xx} - \tau_{xy}^2 - \tau_{yz}^2 - \tau_{zx}^2$$
$$I_3 = \sigma_{xx}\sigma_{yy}\sigma_{zz} - \sigma_{xx}\tau_{yz}^2 - \sigma_{yy}\tau_{zx}^2 - \sigma_{zz}\tau_{xy}^2 - 2\tau_{yz}\tau_{zx}\tau_{xy} \qquad 2.14$$

The stress invariants can also be expressed in terms of principal stresses in the form of:

$$I_1 = \sigma_1 + \sigma_2 + \sigma_3$$
$$I_2 = \sigma_1\sigma_2 + \sigma_2\sigma_3 + \sigma_3\sigma_1$$
$$I_3 = \sigma_1\sigma_2\sigma_3 \qquad 2.15$$

2.6.7.2.3 Mean Stress and Deviatoric Stresses

The state of stress at a point tensor can be expressed as the sum of two other stresses: the mean stress (volumetric stress), p, which tends to change the volume of the stressed body; and the deviatoric stress which tends to distort it. The mean stress of a stressed point is defined as the average of normal stresses in three directions as:

$$p = \frac{1}{3}\left(\sigma_{xx}+\sigma_{yy} + \sigma_{zz}\right) = \frac{1}{3}(I_1) \qquad 2.16$$

The deviatoric components of the stress are defined by

$$s_{ij} = \sigma_{ij} - p\delta_{ij} \qquad 2.17$$

Where δ_{ij} is the Kronecker delta function defined as:

The three invariants of deviatoric stress are

$$J_1 = s_{kk} = 0$$

$$J_2 = \frac{1}{2} s_{ij} s_{ij} = \frac{1}{3}(2I_3 + I_1^2)$$

$$J_3 = \frac{1}{3} s_{ij} s_{jk} s_{ki} = \frac{1}{27}(27I_3 + 9I_1 I_2 + 2I_1^3) \qquad 2.18$$

It is noted that in the theory of soil plasticity, the most useful stress invariants are J_1, J_2 and J_3. Physically, I_1 indicates the effect of mean stress, J_2 represents the magnitude of shear stress, and J_3 determines the direction of shear stress. All these three quantities have a key role in the theory of elastic-plastic stress-strain relations. In soil mechanics (Roscoe and Burland, 1968; Muir Wood, 1990) the mean stress p is often used in pair with a generalized shear stress q defined as:

$$q = \frac{1}{\sqrt{2}}[(\sigma_1 - \sigma_2)^2 + (\sigma_2 - \sigma_3)^2 + (\sigma_3 - \sigma_1)^2]$$

$$= \sqrt{3J_2} \qquad 2.19$$

The stress invariants can also be interpreted geometrically in the principal stress space. The state of stress at material point *A* in the principal stress coordinate system is shown in Figure 2.12. The angle θ is called the Lode angle which is defined as:

$$\theta = -\frac{1}{3} sin^{-1}\left[\frac{3\sqrt{3}}{2}\frac{J_3}{J_2^{3/2}}\right] \qquad 2.20$$

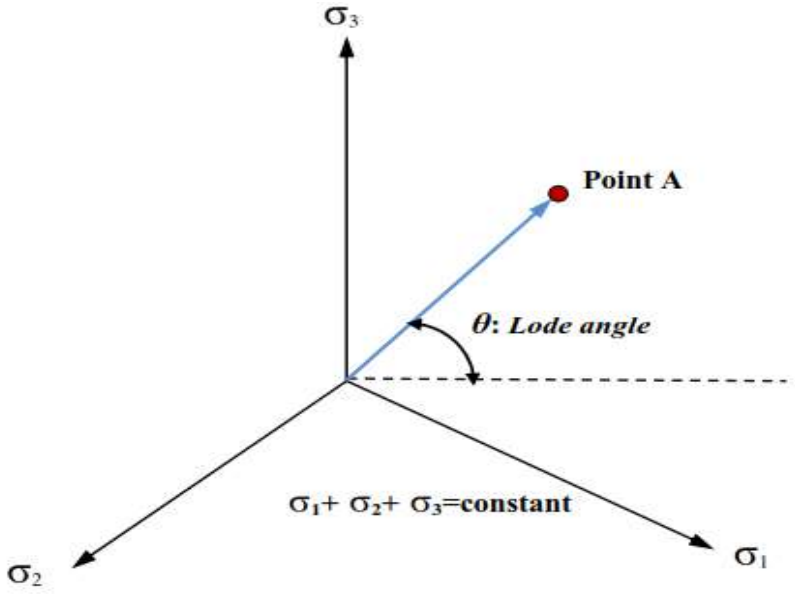

Figure 2.12: Lode angle on a deviatoric plane.

In terms of the mean stress p and the shear stress q, the principal stresses can be expressed as follows:

$$\sigma_1 = p + \frac{2}{3} q \, sin(\theta + 120^o)$$

$$\sigma_2 = p + \frac{2}{3} q \, sin(\theta)$$

$$\sigma_3 = p + \frac{2}{3} q \, sin(\theta - 120^o) \qquad 2.21$$

2.6.7.2.4 Mohr-Coulomb Model

The Mohr-Coulomb criterion is widely used in geotechnical applications. It is a criterion used to model the plastic behavior of soils. The yield criterion is expressed in terms of τ shear stress and σ_n normal stress acting on a plane. The model suggests that the yielding begins as long as the shear stress and the normal stress satisfy by Equation 2.22.

$$\tau = c + \sigma_n \, tan \, \emptyset \qquad 2.22$$

Here c is the cohesion and $\emptyset$ is the angle of internal friction angle.

The Mohr-Coulomb criterion and the involved parameters can be illustrated by plotting Mohr's circle for states of stress in terms of maximum and minimum principal stress. Figure 2.13 shows the Mohr-Coulomb criterion

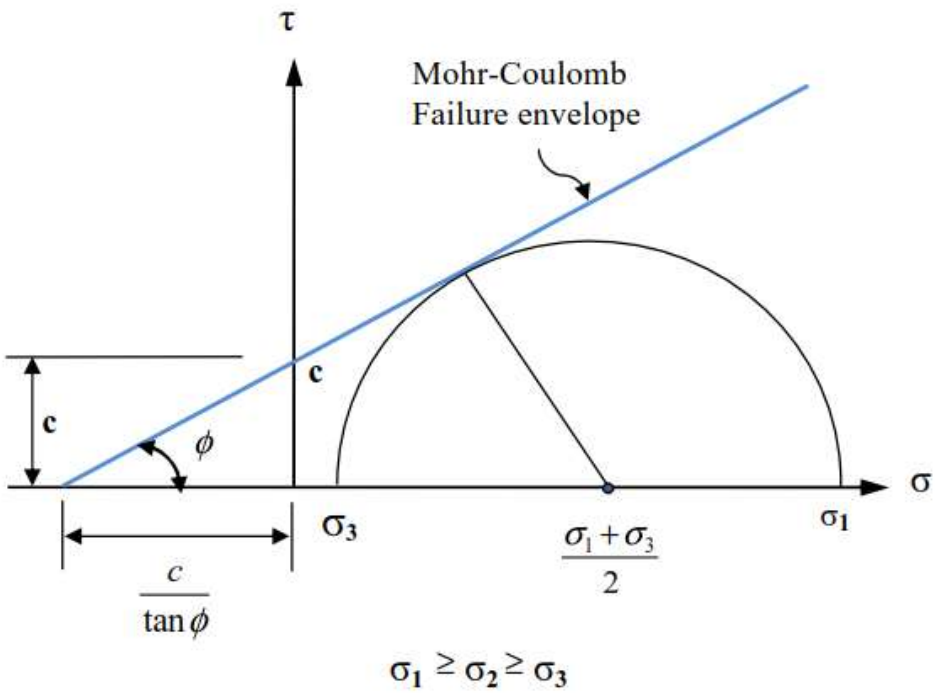

Figure 2.13: The Mohr-Coulomb failure envelope on σ-τ plane.

The yield criterion of the Mohr-Coulomb model can be defined as:

$$f = (\sigma_1 - \sigma_3) - (\sigma_1 + \sigma_3)\sin\emptyset - 2c\cos\emptyset = 0 For\ \sigma_1 \geq \sigma_2 \geq \sigma_3 \qquad 2.23$$

Where $\sigma_1, \sigma_2, \sigma_3$ are principal stresses, and σ_1 and σ_3 are maximum and minimum principal stresses (positive in tension). The Mohr-Coulomb failure model on $\sigma - \tau$ plane is shown in Figure 2.13 and the Mohr-Coulomb yield surface on deviatoric plane is shown in Figure 2.14. In terms of stress invariants and Lode's angle, the Mohr-Coulomb yield criterion takes the following form:

$$f = \sqrt{J_2} - \frac{m(\theta,\emptyset)sin\emptyset}{3} I_1 - m(\theta,\emptyset)c\ cos\ \emptyset = 0 \qquad 2.24$$

Where

$$m(\theta,\emptyset) = \frac{\sqrt{3}}{(\sqrt{3}\ cos\ \theta + sin\ \theta\ sin\ \emptyset)} \qquad 2.25$$

In the Mohr-Coulomb model, the plastic potential takes a very similar form of the yield function. In the plastic potential, instead of the friction angle, the dilation angle φ , is used as follows:

$$g = \sqrt{J_2} - \frac{m(\theta,\varphi)\ sin\ \varphi}{3} I_1 - m(\theta,\varphi).c.cos\ \varphi = 0 \qquad 2.26$$

Where

$$m\ (\theta,\varphi) = \frac{\sqrt{3}}{\sqrt{3}\ cos\ \theta + sin\ \theta\ sin\ \varphi} \qquad 2.27$$

If the flow rule is associated, then the yield criterion and the plastic potential coincides, which yields,

$$\varphi = \theta$$

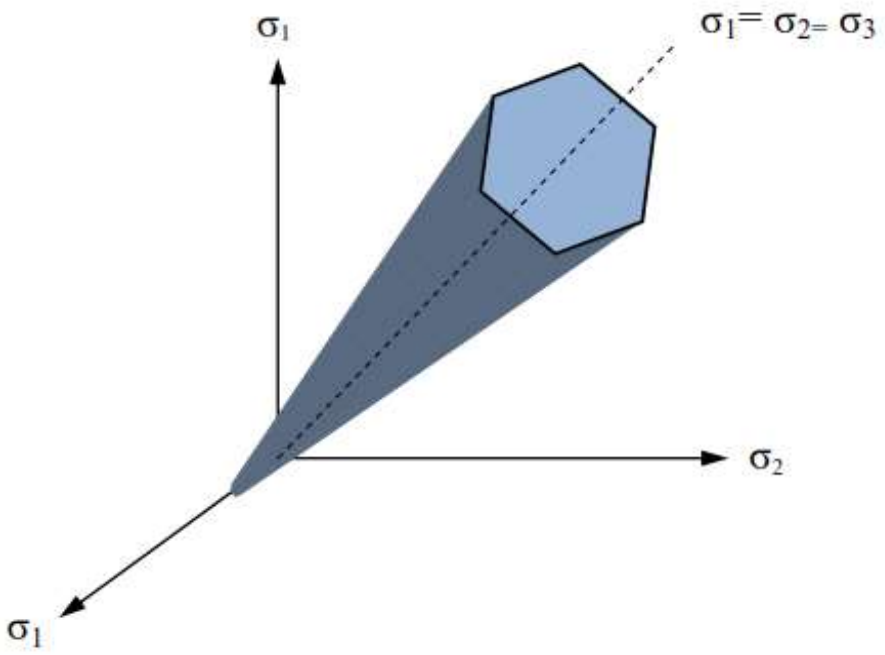

Figure 2.14: The Mohr-Coulomb yield criterion on a deviatoric plane

2.6.7.2.5 Drucker-Prager Model

The Drucker-Prager model was proposed by Drucker and Prager in 1952 for frictional soils. The yield criterion for the Drucker-Prager plasticity model is defined as,

$$f = q - p\,tan\,\phi - c = 0 \qquad 2.28$$

Where $q = \sqrt{3J_2}$ is the generalized shear stress, p $\frac{1}{3}(I_1)$ is the mean stress, ϕ is the friction angle of the material and, c is the cohesion of the material. The parameters ϕ and c can be matched with the Mohr-Coulomb material parameters c (cohesion) and ϕ (angle of internal friction). The Drucker-Prager yield surface is circular on devatoric plane and the three-dimensional yield surface which is a cone is shown in Figure 2.16. Figure 2.15 shows the comparison between yield surface of Mohr-Coulomb and Drucker-Prager models.

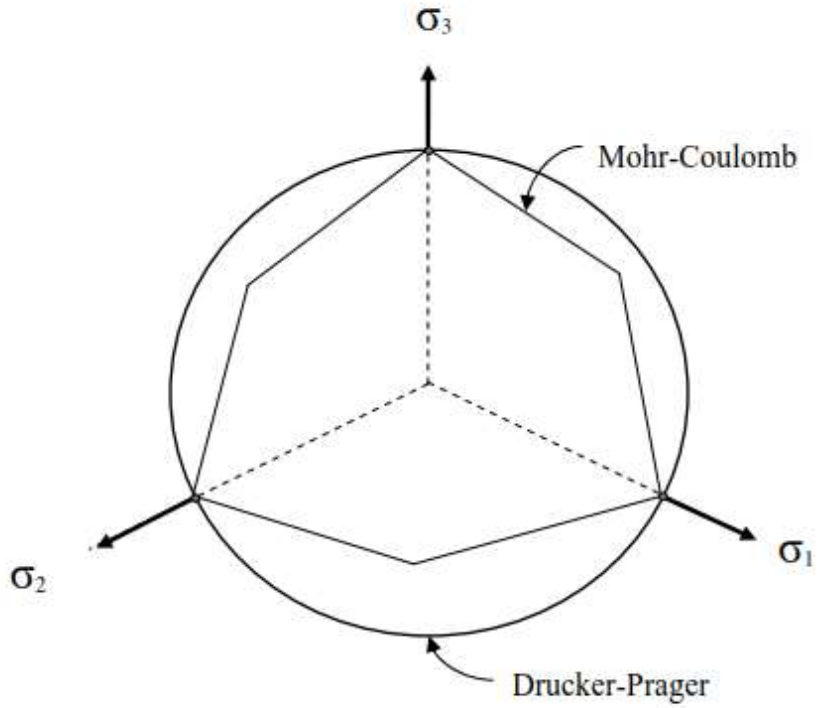

Figure 2.15: Mohr-Coulomb and Drucker-Prager yield surfaces on a deviatoric plane.

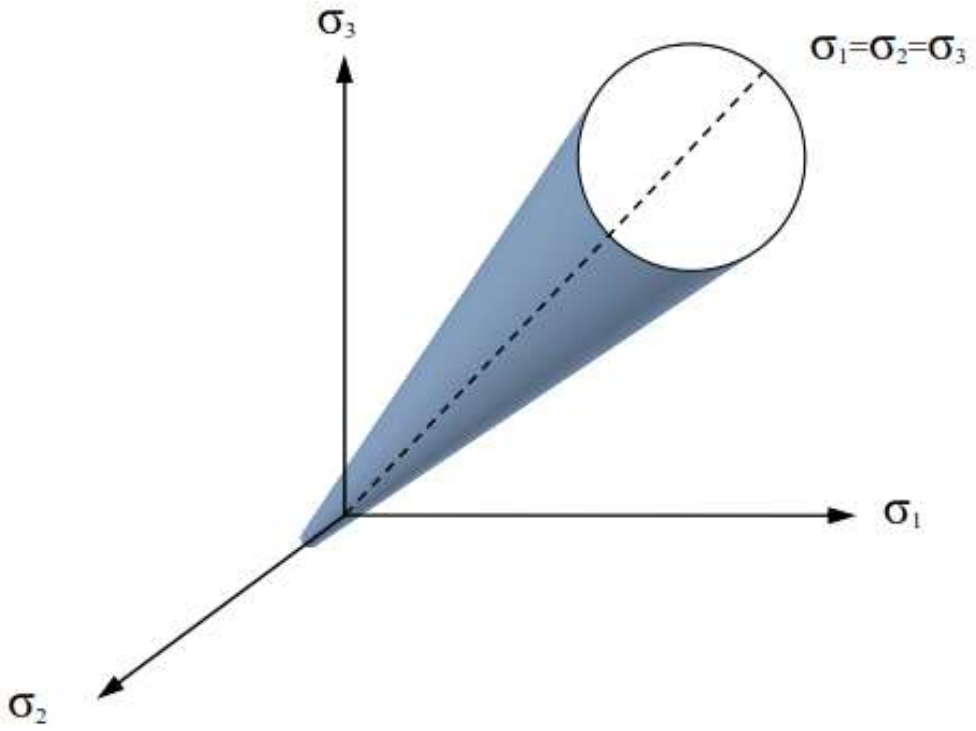

Figure 2.16: The Drucker-Prager failure surface on a deviatoric plane.

CHAPTER 3 GROUND MOTION ANALYSIS

3.1 Introduction

In Ethiopia, due to the development of construction such as high-rise buildings, suspension, tall bridge structures, transmission line towers, and dams. Such structures require a good ground motion estimation for a better seismic hazard assessment (Graves and Pitarka, 2010; Kieling et al. 2014; Viens et al. 2015).

Seismic hazard is an occurrence of ground shaking or ground failure due to earthquakes and it measures the probability of the site to experience high-intensity ground shaking, considering uncertainties in the size, fault type, location, and time of future earthquake.

There are two types of seismic hazard assessments to calculate ground motion for structural design; namely probabilistic seismic hazard analysis (PSHA) and deterministic seismic hazard analysis (DSHA). Most engineering designs use probabilistic seismic hazard analysis (PSHA) approach.

3.2 Seismic Hazard Analysis

Wolaita Sodo converter station is located 6.9°-7° E and 37.72°-38° N. On the Geotechnical investigation report of the Wolaita Sodo converter station there is no study on seismic analysis due to lack of the rupture depth and energy release depth. Wolaita Sodo converter station is located on the seismic hazard map in the range of 0.1g to 0.16g PGA value as shown Figure 3.1.

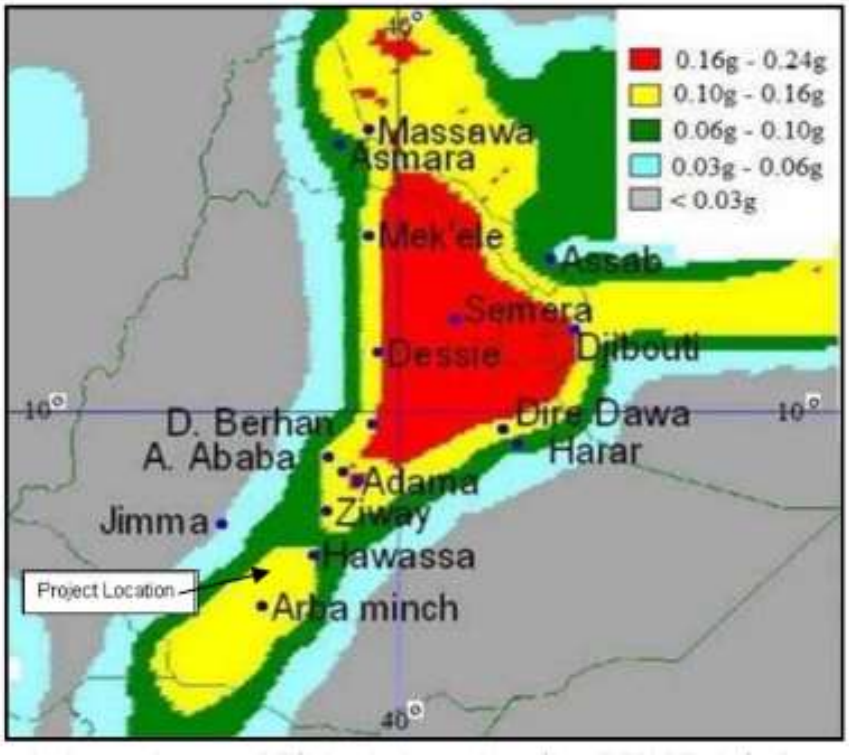

Figure 3.1: The seismic hazard map of Ethiopia based on the GSHAP data for a return period of 475 years (Worku, 2011)

3.2.1 Probabilistic Seismic Hazard Analysis (PSHA)

PSHA methodology was first proposed by (Benjamin & Cornell, 1970) to measure the seismic hazard at a site of interest in terms of a probability distribution. This method is evaluated by considering the possibility of occurrence of earthquakes concerning time, location, size, and magnitude. These methods aim to measure these uncertainties and combine them to develop a clear report of the distribution of future shaking that may occur at a site (Baker, 2008).

3.2.2 Deterministic Seismic Hazard Analysis (DSHA)

DSHA method is modeled for a specific earthquake, either assumed or realistic. The site ground motions are estimated deterministically, given the magnitude, source-to-site distance, and site condition. In this method, one or more earthquakes are specified by magnitude and location for the site.

3.3 Probabilistic Seismic Hazard Analysis

The main goal of PSHA is to evaluate the earthquake hazard in a probabilistic method. This method calculates the annual probability of exceeding the level of various grounds shaking at a site, for a range of intensity levels. Seismic hazard analysis is estimated by considering magnitude-recurrence rates, fault mechanism, source-to-site distance, site conditions (Baker, 2008). The output of seismic hazard analysis is a Hazard Curve (e.g., Figure 3.2), which describes the variation of the selected Intensity Measures (IM) versus its Mean Annual Frequency (MAF) of exceedance (Bommer & Bommer, 2006).

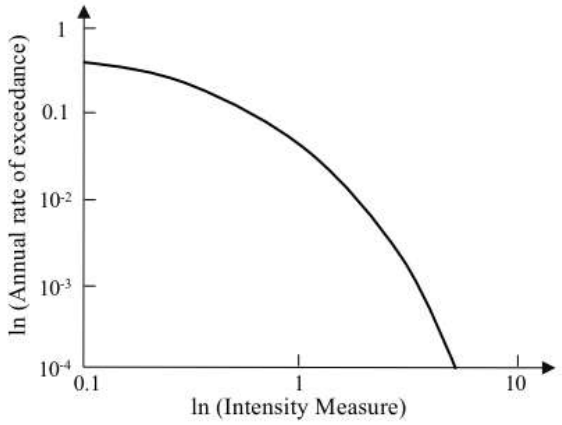

Figure 3.2: PGA hazard curve (Baker, 2008)

Ground motion prediction equations(GMPE) are usually developed by using empirical data of strong-motion data for average horizontal component ground motion are earthquake magnitude, source –site distance (R_{jb}) average shear wave velocity in the upper 30m (V_{S30}), basin depth parameter (Z_1), and style of faulting are important tools in seismic hazard analysis.

3.3.1 Source Parameters

3.3.1.1 Magnitude

Earthquake size is mostly characterized by seismic moment (or moment magnitude) because it is directly related to the amount of energy released in an earthquake. Magnitudes for this thesis are taken

from the study presented by (Ayele, 2017). The seismic design areas are located in the southwestern Ethiopia region at 6.9°-7° E and 37.72°-38° N.

The Gutenberg-Richter magnitude recurrence model better represents earthquake magnitude recurrence. Gutenberg-Richter magnitude distribution relates to the cumulative number of earthquakes λ_m magnitude recurrence relation model proposed by Gutenberg and Richter (1956) is

$$log(\lambda_m) = a - bM \qquad 3.1$$

Where λ_m is the rate of earthquakes with magnitudes greater than M. The constant a and b values are estimated from historical observations.

The constant "a" is associated with the seismicity of a given region (where 10a = annual number of earthquakes with M > 0). The b value defines the relative ratio of the number of small earthquakes to large earthquakes (Baker, 2008)

$$ln(\lambda_m) = \alpha - \beta M \qquad 3.2$$

The Gutenberg-Richter recurrence relationship governed by Equation (3.2) can also be expressed as where α=a ln 10 and β =b ln 10. The Gutenberg-Richter recurrence relationship (3.3)

The maximum possible magnitude is a critical parameter in seismic hazard analysis and its accurate evaluation is appropriate in earthquake engineering. Maximum magnitude (M_{max}) defines the upper limit of magnitude for a given seismic zone and is unknown. M_{max} is estimated from the largest observed earthquake (M_{maxobs}).

In general, M_{max} is estimated by adding an increment, Δm to the largest known magnitude (M_{maxobs}) in the source (Hall & Green , 1994); (Kijko, 2003). The value of M_{max} is taken from the study prepared by (Ayele, 2017) and the value of M_{max} has given 6.8 in the southwestern Ethiopia area.

(Ayele, 2017) give a constant b value 0.77, this value differs from the one obtained by a fitting curve. To be consistent with the upper bound earthquake magnitude, 7.2, (Ayele, 2017) b value is taken.

For Guttenberg-Richter recurrence law, magnitude distribution is expressed by an exponential distribution with probability density function (PDF) and cumulative distribution function CDF of the doubly-bounded (having minimum and maximum magnitude threshold) G-R model is given by (Kramer, 1996) as follows,

CDF

$$F_M(m) = \frac{1-10^{-b(m-m_{min})}}{1-10^{-b(m_{max}-m_{min})}}, \qquad m_{min} \le m \le m_{max} \qquad 3.3$$

PDF

$$f_M(m) = \frac{bln(10)10^{-b(m-m_{min})}}{1-10^{-b(m_{max}-m_{min})}}, \qquad m_{min} \le m \le m_{max} \qquad 3.4$$

$$= \frac{\beta 10^{-b(m-m_{min})}}{1-10^{-b(m_{max}-m_{min})}}$$

The probability of occurrence of a discrete magnitude

$$P(M = m_j) = F_M(m_{j+1}) - F_M(m_j) \qquad 3.5$$

Where, m_j is the discretized magnitude to $m_j < m_{j+1}$

Magnitudes are discretized in an equal interval of 0.1. If the discrete magnitudes are closely spaced, it gives a better approximation. The earthquake magnitudes spaced at intervals of 0.1 as shown in the first column cumulative distribution of the equivalent magnitude shown in the second column the probability of occurrence of the magnitude is shown in the third column.

Table 3.1 Probability of occurrence of discrete magnitudes

m_j	$F_M(m_j)$	$P(M = m_j)$
5	0.000	0.166
5.1	0.166	0.139
5.2	0.305	0.116
5.3	0.421	0.097
5.4	0.518	0.082
5.5	0.600	0.068
5.6	0.668	0.057
5.7	0.726	0.048
5.8	0.774	0.040
5.9	0.814	0.034
6	0.847	0.028
6.1	0.875	0.024
6.2	0.899	0.020
6.3	0.919	0.017
6.4	0.935	0.014
6.5	0.949	0.012
6.6	0.961	0.010
6.7	0.971	0.008
6.8	0.979	0.007
6.9	0.986	0.006
7	0.991	0.005
7.1	0.996	0.004
7.2	1.000	0.001

3.3.1.2 Style-of-Faulting

The consideration of the style of faulting affecting predicting parameters in GMPEs is now common. There are five general types of styles-of-faulting: reverse, reverse/oblique, strike-slip, normal/oblique, and normal. These are typically defined by the rake angle as shown in Figure 3.3. The rake is defined

as the relative movement of the hanging wall during an earthquake with respect to the footwall, measured in the plane of the fault. Rake angle present between the direction of slip on the fault plane and the strike. This angle is separate different styles of faulting but it is not the same for all models, the recent models show the following classification as shown Figure 3.3.

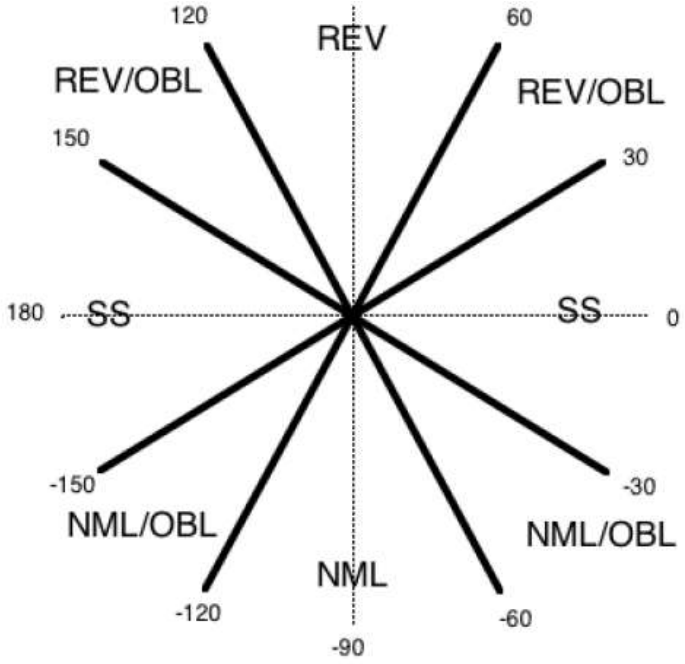

Figure 3.3: Style-of-Faulting in terms of the rake angle

3.3.1.3 Fault Dip Angle (δ)

The fault dip is the angle from the horizontal to the fault plane (see Figure 3.4). A vertical fault has a 90-degree dip. If the dip angle (δ) is not specified, it is estimated from the style of faulting (using the rake angle) from the guidelines explained in Kaklamanos et al. (2011) and modified (Chiou & Youngs, 2008) used in developing their NGA model.

Style of faulting	Dip angle (δ)
Strike − slip faulting	$\delta = 90°$
Normal faulting	$\delta = 50°$
Reverse faulting	$\delta = 40°$

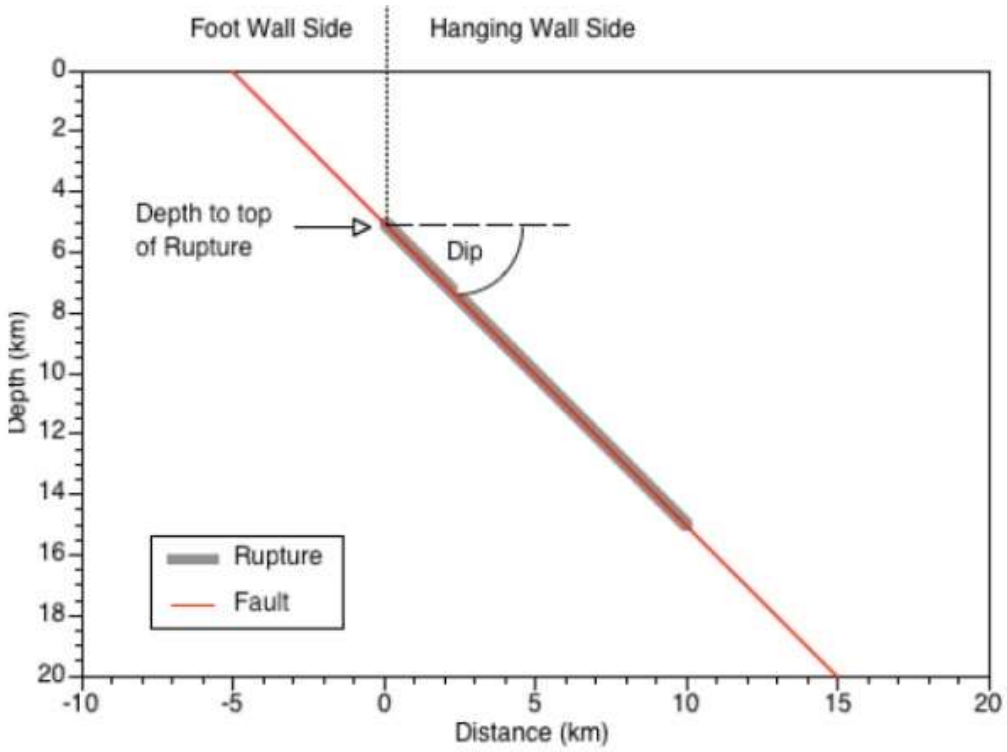

Figure 3.4: Hanging wall and footwall definitions for a buried rupture.

3.3.1.4 Down Dip Width

The average width of a rupture surface is measured in the down-dip direction. The down-dip rupture width (W) is estimated from the moment magnitude (M) and style of faulting by using the logarithmic relationships (Wells & Coppersmith, 1994)

$$W = 10 - 0.76 + 0.27M \quad for\ strike - slip\ events$$
$$W = 10 - 1.61 + 0.41M \quad for\ reverse\ events$$
$$W = 10 - 1.14 + 0.35M \quad for\ normal\ events \qquad 3.6$$

Table 3.2 Calculation of down-dip width of different fault types in each discrete magnitudes

Fault Type			**Down Dip Width**			
Strike-Slip			M	W strike	W reverse	W normal
SS	NF	RF	5	3.89	2.75	4.07
1	0	0	5.1	4.14	3.03	4.42
Normal			5.2	4.41	3.33	4.79
SS	NF	RF	5.3	4.69	3.66	5.19
0	1	0	5.4	4.99	4.02	5.62
Reverse			5.5	5.31	4.42	6.10
SS	NF	RF	5.6	5.65	4.85	6.61
0	0	1	5.7	6.01	5.33	7.16
			5.8	6.40	5.86	7.76
			5.9	6.81	6.44	8.41
			6	7.24	7.08	9.12
			6.1	7.71	7.78	9.89
			6.2	8.20	8.55	10.72
			6.3	8.73	9.40	11.61
			6.4	9.29	10.33	12.59
			6.5	9.89	11.35	13.65
			6.6	10.52	12.47	14.79
			6.7	11.19	13.71	16.03
			6.8	11.91	15.07	17.38
			6.9	12.68	16.56	18.84
			7	13.49	18.20	20.42
			7.1	14.35	20.00	22.13
			7.2	15.28	21.98	23.99

3.3.1.5 Depth to Top of Rupture

In the new Next Generation Attenuation model, the effect of depth of faulting included the depth-to-top of rupture as shown in Figure 3.4. This parameter is the depth to the top of the specific earthquake rupture and not the depth to the top of the fault itself.

Kaklamanos et al. (2010) estimated the depth to the top of rupture (Z_{TOR}) by using the hypocentral depth (Z_{HYP}), down-dip rupture width (W), and dip (δ), assuming that the hypocenter is located 60 percent down the fault width, as suggested by the result of Mai et al. (2005):

$$Z_{TOR} = max\ [(Z_{HYP} - 0.6W\ sin\ \delta),0] \qquad 3.7$$

The values of W and δ are estimated using the above-mentioned methods, and Z_{HYP} may be estimated using the linear relationship between Z_{HYP} and M (Scherbaum , et al., 2004) :

$$Z_{HYP} = 5.63 + 0.68M \quad for\ strike-slip\ events$$
$$Z_{HYP} = 11.24 - 0.2M \quad for\ reverse\ events$$
$$Z_{HYP} = 7.08 + 0.61M \quad for\ normal\ events \qquad 3.8$$

3.3.1.6 Aftershock Flag/Main Shock Flag

In the Next Generation Attenuation (NGA) there are different types of Ground motion Prediction Equations (GMPE) models, AS08 and CY08 models have included aftershock data in their GMPE. Chiou and Youngs (2008) including aftershock data due to it gives additional information to control the site response model coefficients. In their analysis, they found aftershocks tend to produce lower motions than main shocks with similar magnitudes and the style of faulting effects of aftershocks was weaker than main shocks.

Aftershock flag; equal to 1 for aftershocks and 0 for main shocks.

3.3.2 Path Parameters

3.3.2.1 Distance

At the time of earthquake rupture energy released in the form of stress waves, these stress waves travel away from the source of an earthquake and energy decreases with increasing distance from the source. The distance between the source of an earthquake and the site is interpreted in different ways.

Kaklamanos et al. (2011) derive an equation relating the three distance measures required to implement the NGA models. GMPE of Chiou and Youngs (2008) use this model, but the model is used for small distances; otherwise, the errors are large. They use source-to-site azimuth (α) to drive the distance equation. The definition of the source-to-site azimuth is shown in, Appendix A which is a plan view of the surface projection of the ruptured area. It has five example sites that are shown, along with their source-to-site azimuths and site coordinates. Sites 1, 2, and 4 are on the hanging wall side of the fault and have positive azimuths; sites 3 and 5 are on the footwall side of the fault and have negative azimuths. They proposed an approximated number of α If α is not specified based on the average value of the NGA flatfile, assign α to be 50° for sites on the hanging wall side of the fault (F_{HW} = 1) and −50° for sites on the footwall side of the fault (F_{HW} = 0).

R_{RUP}: - Closest distance (km) to the fault rupture plane, as shown in Appendix B.

R_{JB}: - Joyner-Boore distance - The shortest horizontal distance (km) to the surface projection of the rupture area. R_{JB} is the distance to the vertical projection of the fault rupture plane. R_{JB} is zero when located directly above the ruptured area. If the Joyner-Boore distance is less than 10 km it is define the station as a near-source as stated by Yamada et al (2007).

R_X: - The horizontal distance (km) to the fault trace or surface projection of the top of rupture plane. It is measured perpendicular to the fault (or the fictitious extension of the fault).

The site coordinates (R_X) are estimated by using a geometrical equation derived by Kaklamanos et al. (2011) and it depends on the site location, its fault strike, and the fault parameters found in Table 3.3.

Equatins for site coordinate, R_X

For vertical strike-slip faults (i.e., δ= 90°)

$R_X = R_{JB} \sin \alpha$ (for δ = 90°)

For non-vertical faults

Table 3.3 Equations for calculating RX

Azimuth angle	Additional specification	Case(s)	Equation for R_X
$0° \leqq \alpha \leqq 90°$ and	$R_{JB} / \tan\alpha / \leqq W\cos\delta$	2,8	$R_X = R_{JB} / \tan\alpha /$
$90° \leqq \alpha \leqq 180°$	$R_{JB} / \tan\alpha / \geq W\cos\delta$	3,9	$R_X = R_{JB} / \tan\alpha / \cos\left[\alpha - \sin^{-1}\left(\frac{W\cos\delta\cos\alpha}{R_{JB}}\right)\right]$
$\alpha = 90°$	$R_{IB} > 0$	6	$R_X = R_{JB} + W\cos\delta$
	$R_{IB} = 0$ and $R_{RUP} < Z_{TOR}\sec\delta$	5A	$R_X = \sqrt{R_{RUP}^2 + Z_{TOR}^2}$

Euations for rupture distance, R_{RUP}

R_{RUP} can be calculated from R_X

For vertical faults (δ=90°), the rupture distance, R_{RUP}, can be calculated by the Equations 3.9

$$R_{RUP} = \sqrt{R_{JB}^2 + Z_{TOR}^2} \qquad 3.9$$

For non-vertical faults (δ≠90°), the rupture distance, R_{RUP}, can be calculated by the Equations 3.10

$$R_X = \sqrt{{R'_{RUP}}^2 + R_Y^2} \qquad 3.10$$

Where

$$R'_{RUP} = \sqrt{R_X^2 + Z_{TOR}^2} \quad for \quad R_X \leq Z_{TOR} \tan\delta \qquad 3.11$$

$$R'_{RUP} = R_X \sin\delta + Z_{TOR} \cos \quad for \quad Z_{TOR}\tan\delta \leq R_X \leq Z_{TOR}\tan\delta + W\sec\delta \qquad 3.12$$

$$R'_{RUP} = \sqrt{(R_X - W\cos\delta)^2 + (Z_{TOR} + W\sin\delta)^2} \quad for \quad R_X \geq Z_{TOR}\tan\delta + W\sec\delta \qquad 3.13$$

R_Y is the closest distance from the site to the ruptured area, measured parallel to the strike

$$0 \qquad for\ \alpha = \pm\ 90° \qquad 3.14$$

$$RY = RJB \qquad for\ \alpha = 0°\ or\ \pm\ 180° \qquad 3.15$$

$$/\ R_X\ cot\ \alpha\ / \qquad Otherwise \qquad 3.16$$

Table 3.4 Calculation of Site coordinates (Rx) of different fault types in each discrete magnitudes

Fault type	**Dip angle**	M	W strike	W reverse	W normal	W cosδ Strike	W cosδ Reverse	W cosδ Normal
Strike	90°	5	3.89	2.75	4.07	0.00	2.11	2.62
Reverse	40°	5.1	4.14	3.03	4.42	0.00	2.32	2.84
Normal	50°	5.2	4.41	3.33	4.79	0.00	2.55	3.08
		5.3	4.69	3.66	5.19	0.00	2.80	3.33
A	50.0	5.4	4.99	4.02	5.62	0.00	3.08	3.61
Assume Rjb	18.0	5.5	5.31	4.42	6.10	0.00	3.38	3.92
		5.6	5.65	4.85	6.61	0.00	3.72	4.25
		5.7	6.01	5.33	7.16	0.00	4.09	4.60
		5.8	6.40	5.86	7.76	0.00	4.49	4.99
		5.9	6.81	6.44	8.41	0.00	4.93	5.41
		6	7.24	7.08	9.12	0.00	5.42	5.86
		6.1	7.71	7.78	9.89	0.00	5.96	6.35
		6.2	8.20	8.55	10.72	0.00	6.55	6.89
		6.3	8.73	9.40	11.61	0.00	7.20	7.47
		6.4	9.29	10.33	12.59	0.00	7.91	8.09
		6.5	9.89	11.35	13.65	0.00	8.69	8.77
		6.6	10.52	12.47	14.79	0.00	9.56	9.51
		6.7	11.19	13.71	16.03	0.00	10.50	10.31
		6.8	11.91	15.07	17.38	0.00	11.54	11.17
		6.9	12.68	16.56	18.84	0.00	12.68	12.11
		7	13.49	18.20	20.42	0.00	13.94	13.12
		7.1	14.35	20.00	22.13	0.00	15.32	14.23
		7.2	15.28	21.98	23.99	0.00	16.84	15.42

Table 3.5 Calculation of the closest distance to the rupture plane (RRup) for different fault types in each discrete magnitude

R_{ib}=18							
M	Ry reverse	Ry normal	Rrup', reverse	Rrup', normal	Rrup strike	Rrup rev	Rrup nor
5.0	12.58	12.81	17.29	18.12	20.59	21.38	22.19
5.1	12.67	12.91	17.37	18.21	20.59	21.50	22.32
5.2	12.78	13.02	17.45	18.31	20.59	21.63	22.46
5.3	12.89	13.13	17.54	18.41	20.59	21.76	22.62
5.4	13.02	13.25	17.63	18.53	20.59	21.91	22.78
5.5	13.15	13.39	17.73	18.65	20.59	22.08	22.95
5.6	13.30	13.53	17.85	18.78	20.59	22.26	23.14
5.7	13.46	13.68	17.97	18.92	20.59	22.45	23.34
5.8	13.63	13.84	18.10	19.06	20.59	22.66	23.56
5.9	13.82	14.02	18.25	19.22	20.59	22.89	23.79
6.0	14.02	14.20	18.40	19.39	20.59	23.13	24.04
6.1	14.24	14.40	18.57	19.57	20.59	23.40	24.30
6.2	14.47	14.61	18.75	19.76	20.59	23.69	24.57
6.3	14.73	14.83	18.94	19.96	20.59	23.99	24.87
6.4	14.99	15.06	19.15	20.18	20.59	24.32	25.18
6.5	15.28	15.31	19.37	20.40	20.59	24.67	25.51
6.6	15.58	15.56	19.60	20.64	20.59	25.04	25.85
6.7	15.90	15.83	19.84	20.88	20.59	25.42	26.21
6.8	16.22	16.11	20.09	21.14	20.59	25.82	26.58
6.9	16.56	16.39	20.35	21.40	20.59	26.23	26.95
7.0	16.90	16.68	20.61	21.66	20.59	26.65	27.34
7.1	17.23	16.97	20.86	21.92	20.59	27.05	27.72
7.2	17.54	17.25	21.09	22.18	20.59	27.43	28.10

3.3.2.2 Hanging-Wall / Footwall Wall

Somerville and Abrahamson (1995) and Abrahamson and Somerville (1996) proposed the "hanging wall" effect in which ground motions are higher in the hanging wall of reverse earthquakes. Reverse-faulting earthquake produced statistically significant higher motions than strike-slip earthquakes. Dipping faults have a hanging wall and a footwall as shown in Figure 3.5.

In PEER-NGA ground motion models, the source and path parameters allow separation between hanging wall and footwall of dipping faults, the ground motion at hanging wall sites have larger motion than that on footwall sites at the same seismogenic-distance (Somervill 2000).

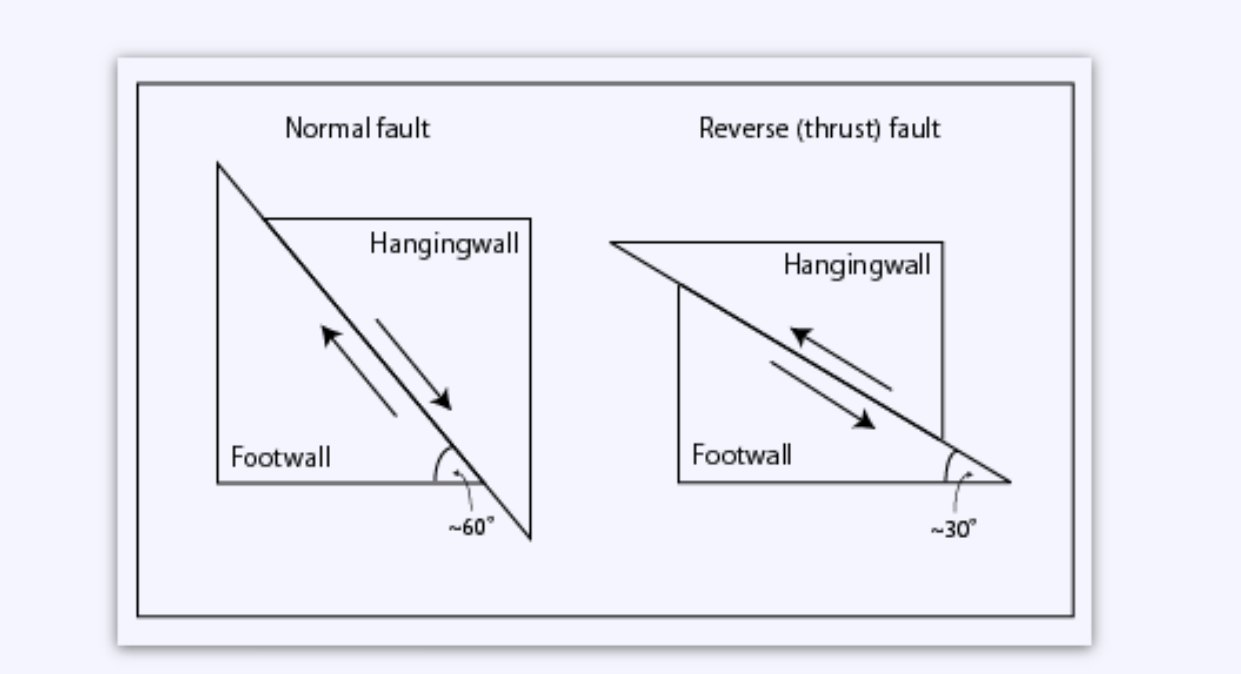

Figure 3.5: Fault types

3.3.3 Site Parameters

The time-averaged shear-wave velocity over a subsurface depth of 30 meters (VS30) is the primary site characteristic in the NGA models.

3.3.3.1 Site Classifications

Site classifications vary from country to country. The amplitude of the ground motion depends on the properties of the material through which waves propagate. Most of the new NGA model site classifications are based on the shear wave velocity in the top 30 m.

The options for site classification that can be chosen are different for various ground motion prediction equations; in this study, ground motion prediction equations are chosen that are suitable for Ethiopia as stated by (Ayele, 2017).

The shear wave velocity (Vs) of each soil or rock layer may be measured in-situ or, where applicable, estimated based on empirical correlations with other parameters (e.g. field or lab data). In-situ measurements of Vs using geophysical methods, where feasible, are relatively simple and preferred for estimating ground motions.

$$V_{S30} = \frac{30m}{\frac{D_1}{V_1} + \frac{D_2}{V_2} + \frac{D_3}{V_3} + \cdots \frac{D_n}{V_n}} \qquad 3.1$$

Where D is the layer thickness (m) and V is the shear wave velocity (m/s) for that layer.

3.3.3.2 Sediment Thickness

The effect of local site conditions is not completely represented by the shear wave velocity. Campbell (1989) found the parameter for depth to basement rock improved the predictive ability of empirical ground motion models. Another investigator had proposed that including basin depth leads to improved empirical ground motion models (e.g., Joyner 2000; Field 2000).

Chiou and Young (2008) add sediment thickness as a second site parameter. It defines the depth to a material (bedrock) with a shear-wave velocity (VS) of 1 km/sec or greater. They recommend using the following median relationship to estimate Z 1.0 from V_{S30}:

$$Z_{1.0} = exp\,[28.5 - \frac{3.82}{8} ln\,[V_{S30}^8 + 378.7^8] \qquad 3.18$$

3.4 Ground Motion Prediction Equations

Many empirical ground motion predictions (attenuation) equations have been developed over the years. Ground motion prediction equations (GMPEs) are used to measure ground-motion intensity, such as Peak Ground Acceleration (PGA) and spectral acceleration at the individual vibration period.

GMPEs are usually derived by using empirical data. Those data and the resulting GMPEs depend on three distinct different tectonic zones: shallow crustal earthquakes, subduction zones, and stable continental regions.

In 2008, the research project ended up with a complete database of strong ground motions recorded worldwide, and a set of peer-reviewed GMPEs (NGA-West1 models) was published for the horizontal ground motion component (Power et al., 2008). Slowly, NGA-west 1 PSHA models applicable outside California. Recent studies by Stafford et al. (2008), Scasserra et al. (2009), Shoja-Taheri et al. (2010), Bradley (2013), and Ayele (2017) tested the applicability of the NGA-West1 GMPEs for the Euro-Mediterranean Region, Italy, Iran, New Zealand, and East Africa rift. Scasserra et al. (2009) have taken a further attempt and modified the distance scaling of the NGA-West1 GMPEs by re-regressing the model coefficients related to the distance attenuation and the constant term for PGA, 0.2, 0.5, 1, and 2 second spectral periods. Bradley (2013) found that the Chiou and Youngs (2008) model performed better than the other NGA-West1 models in capturing the difference between small magnitude scaling of the NGA-West1 and New Zealand datasets, especially after the small magnitude model proposed by Chiou et al. (2010) was included. However, several other features of the Chiou and Youngs (2008) GMPE had to be adjusted for New Zealand and the coefficients of the modified model were provided by Bradley (2013). (Ayele, 2017) Adopted Chiou and Youngs (2008) model for East Africa rift for those seismic sources characterized by shallow crustal earthquakes.

In Ethiopia there is no recorded strong- motion data because of this, there are no estimated or proposed GMPEs based on strong motion data as explained (Ayele, 2017). In this thesis shallow crustal earthquake, GMPE of Chiou and Youngs (2008) model is used as (Ayele, 2017) recommended Chiou and Youngs (2008) attenuation model which seems to match the East African Rift.

$$ln(y_{refij}) = c_1 + c_{1a}F_{RVi} + c_1F_{NMi} + c_7(Z_{TORi} - 4)(1 - AS_i) +$$
$$c_{10} + c_{7a}(Z_{TORi} - 4)AS_i + c_2(M_i - 6) + \frac{c_2 - c_3}{c_n} ln(1 +$$
$$e^{c_n(c_m - M_i)} + c_4 ln(R_{Rupij} + c_5 cosh(c_6\, max(M_i - c_{HM,0}) +$$
$$c_{4a} - c_4 l\, n\left(\sqrt{C_{RB}{}^2 + R_{RUPij}{}^2}\right) +$$
$$(c_{\gamma 1}\frac{c_{\gamma 2}}{cosh(max(M_i - c_{\gamma 3}, 0}) R_{Rupij} +$$
$$c_9 F_{HWij}\, tanh\frac{R_{xij} cos^2\delta_i}{c_{9a}}\frac{\sqrt{R_{JBij}{}^2 + Z_{TORi}{}^2}}{R_{Rupij} + 0.001} \qquad 3.19$$

(David & Haiganoush, 1984) Cited Joyner and Boore (1981) first separated the aleatory variability into inter- and intra-event components by using a two-stage regression technique. Fukushima and Tanaka (1990) showed that failing to separate these components in typical multiple regression leads to an underestimation of the magnitude and distance dependency in GMPEs.

$$ln(yij) = lny_{refij} + \emptyset_1\, min\left(ln\frac{V_{s30j}}{1130}, 0\right) + \emptyset_2(e^{\emptyset_3(min(V_{s30j}, 1130) - 360) -}$$
$$e^{\emptyset_3(1130 - 360)}\, ln\left(\frac{y_{refij} e^{n_i + \emptyset_4}}{\emptyset_4}\right) + \emptyset_5 + \left(1 - \frac{1}{cosh\emptyset_6 max(0, Z_{1.0} - \emptyset_7)}\right) +$$
$$\frac{\emptyset_8}{cosh(0.15.max(0, Z_{1.0} - 15)} + \eta_i + \varepsilon_{ij}$$

3.20

Where;

M Moment magnitude

R_{RUP} The closest distance to the rupture plane (km)

R_{JB} Joyner-Boore distance to the rupture plane (km)

R_X Site coordinate (km) measured perpendicular to the fault strike from the surface projection of the up-dip edge of the fault rupture, with the down-dip direction being positive.

F_{HW} Hanging-wall flag: 1 for $R_X \geq 0$ and 0 for $R_X < 0$

δ Fault dip angle

Z_{TOR} Depth to top of rupture (km)

F_{RV} Reverse faulting flag: 1 for $30° \leq \lambda \leq 150°$ (combined reverse and reverse oblique), 0 otherwise; λ is the rake angle

F_{NM} Normal faulting flag: 1 for $-120° \leq \lambda \leq -60°$ (excludes normal-oblique), 0 otherwise.

AS Aftershock flag: 1 if the event is an aftershock, 0 otherwise

V_{S30} Average shear wave velocity in the top 30 m (m/s)

$Z_{1.0}$ Depth to shear wave velocity of 1.0 km/s (m).

Table 3.6 Coefficients used by Chiou and Youngs (2008) GMPE for estimating peak ground acceleration

Period-dependent coefficients

c1	-1.2687	c7	0.0512
c1a	0.1	c7a	0.086
c1b	-0.255	c9	0.79
Cn	2.996	c9a	1.5005
CM	4.184	c10	-0.3218
c5	6.16	cy1	-0.00804
c6	0.4893	Cy2	-0.00785

Period-independent coefficients

c2	1.06	CRB	50
c3	3.45	CHM	3
c4	-2.1	cy3	4
c4a	-0.5		

Coefficients of variance

τ1	0.3437	σ4	0.0663
τ2	0.2637	F inffered	1
σ1	0.4458	Fmeasure	0
σ2	0.3459	V_{S30}	557.0251
σ3	0.8		

Coefficients of site response

ϕ1	-0.4417	ϕ5	0.2289
ϕ2	-0.1417	ϕ6	0.014996
ϕ3	-0.00701	ϕ7	580
ϕ4	0.102151	ϕ8	0.07

Dip angle (δ)	
90	Fhw
40	1
50	

Hanging wall effect

Fhw	1

Strike Slip		
SS	NF	RF
1	0	0
Normal		
SS	NF	RF
0	1	0
Reverse		
SS	NF	RF
0	0	1

3.5 Effect of Earthquake Size

The effect of earthquake size is calculated in Table 3.7. The first three columns show the fault mechanism. The 4th & 5th columns show the symbols and the value coefficients of earthquake size.

In this thesis, the magnitude is discrete into 0.1 intervals from a minimum value of 5 to the maximum value of 7.2

Table 3.7 Earthquake magnitude scaling

Earthquake magnitude effect								
Strike Slip			c1	-1.2687	Mi	Strike Slip	Normal	Reverse
SS	NF	RF	c1a	0.1	5.0	-2.088	-2.343	-1.988
1	0	0	c1b	-0.255	5.1	-1.965	-2.220	-1.865
Normal			Cn	2.996	5.2	-1.847	-2.102	-1.747
SS	NF	RF	CM	4.184	5.3	-1.731	-1.986	-1.631
0	1	0	c7	0.0512	5.4	-1.618	-1.873	-1.518
Reverse			c2	1.06	5.5	-1.507	-1.762	-1.407
SS	NF	RF	c3	3.45	5.6	-1.397	-1.652	-1.297
0	0	1	Ztor	10	5.7	-1.288	-1.543	-1.188
					5.8	-1.180	-1.435	-1.080
					5.9	-1.072	-1.327	-0.972
					6.0	-0.965	-1.220	-0.865
					6.1	-0.858	-1.113	-0.758
					6.2	-0.751	-1.006	-0.651
					6.3	-0.645	-0.900	-0.545
					6.4	-0.539	-0.794	-0.439
					6.5	-0.432	-0.687	-0.332
					6.6	-0.326	-0.581	-0.226
					6.7	-0.220	-0.475	-0.120
					6.8	-0.114	-0.369	-0.014
					6.9	-0.008	-0.263	0.092
					7.0	0.098	-0.157	0.198
					7.1	0.204	-0.051	0.304
					7.2	0.310	0.055	0.410

3.6 Effect of Distance Path

The path function is calculated in Table 3.8. The first two columns show the path coefficient symbols and value. The 3rd column shows the discrete magnitude. 4th to 6th columns show the calculated values of R for different fault mechanisms.

Table 3.8 Distance path effect calculation

Distance path effect					
Coefficient		Mi	Strike	Reverse	Normal
c5	6.16	5	-2.25230	-2.27898	-2.30554
c6	0.4893	5.1	-2.31698	-2.34650	-2.37256
cy1	-0.00804	5.2	-2.38289	-2.41532	-2.44084
Cy2	-0.00785	5.3	-2.45001	-2.48540	-2.51034
c4	-2.1	5.4	-2.51830	-2.55674	-2.58103
c4a	-0.5	5.5	-2.58776	-2.62928	-2.65288
CRB	50	5.6	-2.65835	-2.70300	-2.72586
CHM	3	5.7	-2.73004	-2.77787	-2.79992
cy3	4	5.8	-2.80282	-2.85385	-2.87503
		5.9	-2.87667	-2.93090	-2.95116
		6	-2.95154	-3.00897	-3.02825
		6.1	-3.02743	-3.08801	-3.10627
		6.2	-3.10430	-3.16798	-3.18516
		6.3	-3.18213	-3.24882	-3.26489
		6.4	-3.26089	-3.33048	-3.34539
		6.5	-3.34056	-3.41287	-3.42661
		6.6	-3.42111	-3.49594	-3.50850
		6.7	-3.50251	-3.57960	-3.59099
		6.8	-3.58474	-3.66377	-3.67402
		6.9	-3.66778	-3.74834	-3.75753
		7	-3.75160	-3.83320	-3.84143
		7.1	-3.83617	-3.91821	-3.92565
		7.2	-3.92147	-4.00321	-4.01010

3.7 Effect of Hanging Wall

Table 3.9 Calculation of Hanging Wall effect

Hanging wall effect					
Dip angle (δ)	Hanging wall coefficient	Mi	Strike	Reverse	Normal
90	1	5	4.85619E-05	0.827083171	0.861795783
40		5.1	4.85619E-05	0.832278379	0.867279359
50		5.2	4.85619E-05	0.837886408	0.873106804
		5.3	4.85619E-05	0.843929744	0.879290042
		5.4	4.85619E-05	0.850430037	0.885839792
		5.5	4.85619E-05	0.857407576	0.89276523
		5.6	4.85619E-05	0.86488067	0.900073602
		5.7	4.85619E-05	0.872864911	0.907769792
		5.8	4.85619E-05	0.881372313	0.915855837
		5.9	4.85619E-05	0.890410315	0.92433037
		6	4.85619E-05	0.899980606	0.933187996
		6.1	4.85619E-05	0.910077765	0.942418575
		6.2	4.85619E-05	0.920687657	0.952006399
		6.3	4.85619E-05	0.931785518	0.961929224
		6.4	4.85619E-05	0.94333363	0.972157106
		6.5	4.85619E-05	0.955278409	0.982650977
		6.6	4.85619E-05	0.967546616	0.993360838
		6.7	4.85619E-05	0.980040226	1.004223377
		6.8	4.85619E-05	0.992629106	1.01515874
		6.9	4.85619E-05	1.005140022	1.026065944
		7	4.85619E-05	1.017339145	1.036816129
		7.1	4.85619E-05	1.028902485	1.047242164
		7.2	4.85619E-05	1.039362221	1.05712191

PGA calculated from the distance of 22m up to 29m Rupture distance, the R_{jb} distance of 18m, and magnitude of 5 up to 7.2 as shown in Table 3.10. The first column shows the magnitude, from 2nd to and 4th column shows the magnitude (Source) effect according to the style of faulting. From the 5th to 7th column shows the distance (path) effect, according to the style of faulting. The 8th, 9th, and 10th columns show the Hanging wall effect. The last three columns show the PGA values of Strike-Slip, Reverse, and Normal faults

Table 3.10 Peak ground acceleration

PGA															
	Magntude effect			Distance effect			Hanging Wall			$\ln(Y_{refij})=E_M+E_D+E_{HW}$			Y_{refij} in g		
M	Strike	Reverse	Normal	Strike	Reverse	Normal	Strike	Reverse	Normal	Strike	Reverse	Normal	Strike	Reverse	Normal
5	-2.088	-1.988	-2.343	-2.252	-2.279	-2.306	0.000	0.827	0.862	-4.340	-3.440	-3.787	0.013	0.032	0.023
5.1	-1.965	-1.865	-2.220	-2.317	-2.347	-2.373	0.000	0.832	0.867	-4.282	-3.379	-3.725	0.014	0.034	0.024
5.2	-1.847	-1.747	-2.102	-2.383	-2.415	-2.441	0.000	0.838	0.873	-4.229	-3.324	-3.669	0.015	0.036	0.025
5.3	-1.731	-1.631	-1.986	-2.450	-2.485	-2.510	0.000	0.844	0.879	-4.181	-3.273	-3.617	0.015	0.038	0.027
5.4	-1.618	-1.518	-1.873	-2.518	-2.557	-2.581	0.000	0.850	0.886	-4.136	-3.224	-3.568	0.016	0.040	0.028
5.5	-1.507	-1.407	-1.762	-2.588	-2.629	-2.653	0.000	0.857	0.893	-4.095	-3.179	-3.522	0.017	0.042	0.030
5.6	-1.397	-1.297	-1.652	-2.658	-2.703	-2.726	0.000	0.865	0.900	-4.055	-3.135	-3.478	0.017	0.043	0.031
5.7	-1.288	-1.188	-1.543	-2.730	-2.778	-2.800	0.000	0.873	0.908	-4.018	-3.093	-3.435	0.018	0.045	0.032
5.8	-1.180	-1.080	-1.435	-2.803	-2.854	-2.875	0.000	0.881	0.916	-3.983	-3.052	-3.394	0.019	0.047	0.034
5.9	-1.072	-0.972	-1.327	-2.877	-2.931	-2.951	0.000	0.890	0.924	-3.949	-3.013	-3.354	0.019	0.049	0.035
6	-0.965	-0.865	-1.220	-2.952	-3.009	-3.028	0.000	0.900	0.933	-3.916	-2.974	-3.315	0.020	0.051	0.036
6.1	-0.858	-0.758	-1.113	-3.027	-3.088	-3.106	0.000	0.910	0.942	-3.885	-2.936	-3.277	0.021	0.053	0.038
6.2	-0.751	-0.651	-1.006	-3.104	-3.168	-3.185	0.000	0.921	0.952	-3.856	-2.899	-3.240	0.021	0.055	0.039
6.3	-0.645	-0.545	-0.900	-3.182	-3.249	-3.265	0.000	0.932	0.962	-3.827	-2.862	-3.203	0.022	0.057	0.041
6.4	-0.539	-0.439	-0.794	-3.261	-3.330	-3.345	0.000	0.943	0.972	-3.799	-2.826	-3.167	0.022	0.059	0.042
6.5	-0.432	-0.332	-0.687	-3.341	-3.413	-3.427	0.000	0.955	0.983	-3.773	-2.790	-3.131	0.023	0.061	0.044
6.6	-0.326	-0.226	-0.581	-3.421	-3.496	-3.508	0.000	0.968	0.993	-3.747	-2.754	-3.096	0.024	0.064	0.045
6.7	-0.220	-0.120	-0.475	-3.503	-3.580	-3.591	0.000	0.980	1.004	-3.722	-2.719	-3.062	0.024	0.066	0.047
6.8	-0.114	-0.014	-0.369	-3.585	-3.664	-3.674	0.000	0.993	1.015	-3.699	-2.685	-3.028	0.025	0.068	0.048
6.9	-0.008	0.092	-0.263	-3.668	-3.748	-3.758	0.000	1.005	1.026	-3.675	-2.651	-2.994	0.025	0.071	0.050
7	0.098	0.198	-0.157	-3.752	-3.833	-3.841	0.000	1.017	1.037	-3.653	-2.618	-2.961	0.026	0.073	0.052
7.1	0.204	0.304	-0.051	-3.836	-3.918	-3.926	0.000	1.029	1.047	-3.632	-2.585	-2.929	0.026	0.075	0.053
7.2	0.310	0.410	0.055	-3.921	-4.003	-4.010	0.000	1.039	1.057	-3.611	-2.553	-2.898	0.027	0.078	0.055

Table 3.11 Summary of PGA for all considering normal fault

PGA Summary for normal fault																								
Distance		**Magnitude**																						
R_{jb}	18																							
R_X	R_{RUP}	5.00	5.10	5.20	5.30	5.40	5.50	5.60	5.70	5.80	5.90	6.00	6.10	6.20	6.30	6.40	6.50	6.60	6.70	6.80	6.90	7.00	7.10	7.20
15.27	22.19	0.01	0.01	0.01	0.01	0.02	0.02	0.02	0.03	0.03	0.03	0.04	0.04	0.05	0.05	0.06	0.06	0.07	0.08	0.08	0.09	0.10	0.10	0.11
15.38	22.32	0.01	0.01	0.01	0.01	0.02	0.02	0.02	0.03	0.03	0.03	0.04	0.04	0.05	0.05	0.06	0.07	0.07	0.08	0.08	0.09	0.10	0.10	0.11
15.51	22.46	0.01	0.01	0.01	0.01	0.02	0.02	0.02	0.03	0.03	0.03	0.04	0.04	0.05	0.05	0.06	0.07	0.07	0.08	0.09	0.09	0.10	0.11	0.11
15.65	22.62	0.01	0.01	0.01	0.01	0.02	0.02	0.02	0.03	0.03	0.03	0.04	0.04	0.05	0.06	0.06	0.07	0.07	0.08	0.09	0.09	0.10	0.11	0.12
15.79	22.78	0.01	0.01	0.01	0.01	0.02	0.02	0.02	0.03	0.03	0.04	0.04	0.05	0.05	0.06	0.06	0.07	0.07	0.08	0.09	0.09	0.10	0.11	0.12
15.95	22.95	0.01	0.01	0.01	0.01	0.02	0.02	0.02	0.03	0.03	0.04	0.04	0.05	0.05	0.06	0.06	0.07	0.08	0.08	0.09	0.10	0.10	0.11	0.12
16.12	23.14	0.01	0.01	0.01	0.01	0.02	0.02	0.02	0.03	0.03	0.04	0.04	0.05	0.05	0.06	0.06	0.07	0.08	0.08	0.09	0.10	0.10	0.11	0.12
16.30	23.34	0.01	0.01	0.01	0.01	0.02	0.02	0.02	0.03	0.03	0.04	0.04	0.05	0.05	0.06	0.06	0.07	0.08	0.08	0.09	0.10	0.11	0.11	0.12
16.50	23.56	0.01	0.01	0.01	0.01	0.02	0.02	0.02	0.03	0.03	0.04	0.04	0.05	0.05	0.06	0.07	0.07	0.08	0.09	0.09	0.10	0.11	0.12	0.13
16.70	23.79	0.01	0.01	0.01	0.01	0.02	0.02	0.02	0.03	0.03	0.04	0.04	0.05	0.05	0.06	0.07	0.07	0.08	0.09	0.09	0.10	0.11	0.12	0.13
16.92	24.04	0.01	0.01	0.01	0.01	0.02	0.02	0.02	0.03	0.03	0.04	0.04	0.05	0.05	0.06	0.07	0.07	0.08	0.09	0.10	0.10	0.11	0.12	0.13
17.16	24.30	0.01	0.01	0.01	0.01	0.02	0.02	0.02	0.03	0.03	0.04	0.04	0.05	0.06	0.06	0.07	0.08	0.08	0.09	0.10	0.11	0.11	0.12	0.13
17.41	24.57	0.01	0.01	0.01	0.01	0.02	0.02	0.03	0.03	0.03	0.04	0.04	0.05	0.06	0.06	0.07	0.08	0.08	0.09	0.10	0.11	0.12	0.13	0.14
17.67	24.87	0.01	0.01	0.01	0.01	0.02	0.02	0.03	0.03	0.03	0.04	0.04	0.05	0.06	0.06	0.07	0.08	0.09	0.09	0.10	0.11	0.12	0.13	0.14
17.95	25.18	0.01	0.01	0.01	0.01	0.02	0.02	0.03	0.03	0.03	0.04	0.05	0.05	0.06	0.06	0.07	0.08	0.09	0.10	0.10	0.11	0.12	0.13	0.14
18.24	25.51	0.01	0.01	0.01	0.01	0.02	0.02	0.03	0.03	0.04	0.04	0.05	0.05	0.06	0.07	0.07	0.08	0.09	0.10	0.11	0.11	0.12	0.13	0.15
18.55	25.85	0.01	0.01	0.01	0.01	0.02	0.02	0.03	0.03	0.04	0.04	0.05	0.05	0.06	0.07	0.07	0.08	0.09	0.10	0.11	0.12	0.13	0.14	0.15
18.87	26.21	0.01	0.01	0.01	0.02	0.02	0.02	0.03	0.03	0.04	0.04	0.05	0.05	0.06	0.07	0.08	0.08	0.09	0.10	0.11	0.12	0.13	0.14	0.15
19.20	26.58	0.01	0.01	0.01	0.02	0.02	0.02	0.03	0.03	0.04	0.04	0.05	0.05	0.06	0.07	0.08	0.09	0.09	0.10	0.11	0.12	0.13	0.14	0.16
19.54	26.95	0.01	0.01	0.01	0.02	0.02	0.02	0.03	0.03	0.04	0.04	0.05	0.06	0.06	0.07	0.08	0.09	0.10	0.11	0.11	0.12	0.13	0.15	0.16
19.88	27.34	0.01	0.01	0.01	0.02	0.02	0.02	0.03	0.03	0.04	0.04	0.05	0.06	0.06	0.07	0.08	0.09	0.10	0.11	0.12	0.13	0.14	0.15	0.16
20.22	27.72	0.01	0.01	0.01	0.02	0.02	0.02	0.03	0.03	0.04	0.04	0.05	0.06	0.06	0.07	0.08	0.09	0.10	0.11	0.12	0.13	0.14	0.15	0.17
20.56	28.10	0.01	0.01	0.01	0.02	0.02	0.02	0.03	0.03	0.04	0.04	0.05	0.06	0.07	0.07	0.08	0.09	0.10	0.11	0.12	0.13	0.14	0.16	0.17

For a given site the peak Ground motion (PGA) is calculated by considering site distance and magnitudes effect in the area of the site. The above effect is assumed to happen on some average probability per year to assess the risk to a structure from earthquake shaking. Lesser ground motions are relatively expected, large ground motions are much unexpected.

To calculate the probability of exceedance of a given earthquake it should be determined for every combination of discretized magnitude and distance of each source. The probability of a specific ground motion PGA exceeds a certain value x for a given magnitude *m* and distance *r* of the earthquake (Baker, 2008).

$$P(PGA > x \,/\, m, r) = 1 - \Phi(x) \qquad 3.21$$

$$P(PGA > x \,/\, m, r) = 1 - \Phi(\frac{ln\, x - \mu}{\delta}) \qquad 3.22$$

Where Φ is cumulative distribution function x exceedance, μ mean, and δ standard deviation.

(Martin & Perez, 2009) are used lognormal distribution to model engineering data. (Huyse & Stamatakos, 2003) They use lognormal distribution for low-probability ground motions and explained in the PSHA 10^{-6} is the smallest annual exceedance probabilities. In this thesis lognormal distribution is applicable exceedance vary from 0.05g to 0.8 g with adding about 0.05. See Table 3.12 and Table 3.13 for 0.05 and 0.8 exceedance respectively.

Table 3.12 Probability of PGA exceeding 0.05g for a given earth

P(PGA>x / m,r)= P(PGA>0.05 / m,r)																								
Distance		**Magnitude**																						
R_{jb}	18																							
R_X	**R_{Rup}**	5.00	5.10	5.20	5.30	5.40	5.50	5.60	5.70	5.80	5.90	6.00	6.10	6.20	6.30	6.40	6.50	6.60	6.70	6.80	6.90	7.00	7.10	7.20
15.27	22.19	0.01	0.02	0.04	0.06	0.09	0.13	0.18	0.22	0.28	0.33	0.38	0.43	0.48	0.53	0.58	0.62	0.66	0.69	0.72	0.75	0.77	0.80	0.82
15.38	22.32	0.01	0.02	0.04	0.06	0.10	0.13	0.18	0.23	0.28	0.33	0.39	0.44	0.49	0.54	0.58	0.62	0.66	0.70	0.73	0.75	0.78	0.80	0.83
15.51	22.46	0.01	0.02	0.04	0.07	0.10	0.14	0.18	0.23	0.28	0.34	0.39	0.44	0.49	0.54	0.59	0.63	0.67	0.70	0.73	0.76	0.78	0.81	0.83
15.65	22.62	0.01	0.02	0.04	0.07	0.10	0.14	0.18	0.23	0.29	0.34	0.39	0.45	0.50	0.55	0.59	0.63	0.67	0.70	0.74	0.76	0.79	0.81	0.83
15.79	22.78	0.01	0.02	0.04	0.07	0.10	0.14	0.19	0.24	0.29	0.34	0.40	0.45	0.50	0.55	0.60	0.64	0.68	0.71	0.74	0.77	0.79	0.82	0.84
15.95	22.95	0.01	0.02	0.04	0.07	0.10	0.14	0.19	0.24	0.29	0.35	0.40	0.46	0.51	0.56	0.60	0.64	0.68	0.72	0.75	0.77	0.80	0.82	0.84
16.12	23.14	0.01	0.02	0.04	0.07	0.10	0.15	0.19	0.24	0.30	0.35	0.41	0.46	0.52	0.56	0.61	0.65	0.69	0.72	0.75	0.78	0.80	0.83	0.85
16.30	23.34	0.01	0.02	0.04	0.07	0.11	0.15	0.20	0.25	0.30	0.36	0.41	0.47	0.52	0.57	0.62	0.66	0.69	0.73	0.76	0.78	0.81	0.83	0.85
16.50	23.56	0.01	0.02	0.04	0.07	0.11	0.15	0.20	0.25	0.31	0.36	0.42	0.48	0.53	0.58	0.62	0.66	0.70	0.73	0.76	0.79	0.81	0.84	0.86
16.70	23.79	0.01	0.03	0.05	0.07	0.11	0.15	0.20	0.26	0.31	0.37	0.43	0.48	0.53	0.58	0.63	0.67	0.71	0.74	0.77	0.79	0.82	0.84	0.86
16.92	24.04	0.01	0.03	0.05	0.07	0.11	0.16	0.21	0.26	0.32	0.37	0.43	0.49	0.54	0.59	0.64	0.68	0.71	0.75	0.78	0.80	0.82	0.85	0.87
17.16	24.30	0.01	0.03	0.05	0.08	0.11	0.16	0.21	0.26	0.32	0.38	0.44	0.49	0.55	0.60	0.64	0.68	0.72	0.75	0.78	0.81	0.83	0.85	0.87
17.41	24.57	0.01	0.03	0.05	0.08	0.12	0.16	0.21	0.27	0.33	0.39	0.44	0.50	0.55	0.60	0.65	0.69	0.73	0.76	0.79	0.81	0.83	0.86	0.88
17.67	24.87	0.01	0.03	0.05	0.08	0.12	0.16	0.22	0.27	0.33	0.39	0.45	0.51	0.56	0.61	0.66	0.70	0.73	0.77	0.79	0.82	0.84	0.86	0.88
17.95	25.18	0.01	0.03	0.05	0.08	0.12	0.17	0.22	0.28	0.34	0.40	0.46	0.51	0.57	0.62	0.66	0.70	0.74	0.77	0.80	0.83	0.85	0.87	0.89
18.24	25.51	0.01	0.03	0.05	0.08	0.12	0.17	0.22	0.28	0.34	0.40	0.46	0.52	0.58	0.63	0.67	0.71	0.75	0.78	0.81	0.83	0.85	0.87	0.89
18.55	25.85	0.01	0.03	0.05	0.08	0.12	0.17	0.23	0.29	0.35	0.41	0.47	0.53	0.58	0.63	0.68	0.72	0.75	0.79	0.81	0.84	0.86	0.88	0.90
18.87	26.21	0.01	0.03	0.05	0.08	0.12	0.17	0.23	0.29	0.35	0.41	0.48	0.53	0.59	0.64	0.68	0.73	0.76	0.79	0.82	0.84	0.86	0.88	0.90
19.20	26.58	0.01	0.03	0.05	0.08	0.13	0.18	0.23	0.29	0.36	0.42	0.48	0.54	0.60	0.65	0.69	0.73	0.77	0.80	0.83	0.85	0.87	0.89	0.90
19.54	26.95	0.01	0.03	0.05	0.08	0.13	0.18	0.24	0.30	0.36	0.43	0.49	0.55	0.60	0.65	0.70	0.74	0.77	0.80	0.83	0.85	0.87	0.89	0.91
19.88	27.34	0.01	0.03	0.05	0.09	0.13	0.18	0.24	0.30	0.37	0.43	0.49	0.55	0.61	0.66	0.70	0.75	0.78	0.81	0.84	0.86	0.88	0.90	0.91
20.22	27.72	0.01	0.03	0.05	0.09	0.13	0.18	0.24	0.30	0.37	0.44	0.50	0.56	0.61	0.67	0.71	0.75	0.79	0.82	0.84	0.86	0.88	0.90	0.92
20.56	28.10	0.01	0.03	0.05	0.09	0.13	0.18	0.24	0.31	0.37	0.44	0.50	0.56	0.62	0.67	0.72	0.76	0.79	0.82	0.85	0.87	0.89	0.91	0.92

Table 3.13 Probability of PGA exceeding 0.8g for a given earthquake

Distance		Magnitude																					
Rjb	18																						
RX	Rrup	5.00	5.10	5.20	5.30	5.40	5.50	5.60	5.70	5.80	5.90	6.00	6.10	6.20	6.30	6.40	6.50	6.60	6.70	6.80	6.90	7.00	7.10	7.20
15.27	22.19	0.00	0.00	0.00	0.00	0.00	0.00	0.00	0.00	0.00	0.00	0.00	0.00	0.00	0.00	0.00	0.00	0.00	0.00	0.00	0.01	0.01	0.01	0.01
15.38	22.32	0.00	0.00	0.00	0.00	0.00	0.00	0.00	0.00	0.00	0.00	0.00	0.00	0.00	0.00	0.00	0.00	0.00	0.00	0.00	0.01	0.01	0.01	0.01
15.51	22.46	0.00	0.00	0.00	0.00	0.00	0.00	0.00	0.00	0.00	0.00	0.00	0.00	0.00	0.00	0.00	0.00	0.00	0.00	0.00	0.01	0.01	0.01	0.01
15.65	22.62	0.00	0.00	0.00	0.00	0.00	0.00	0.00	0.00	0.00	0.00	0.00	0.00	0.00	0.00	0.00	0.00	0.00	0.00	0.01	0.01	0.01	0.01	0.01
15.79	22.78	0.00	0.00	0.00	0.00	0.00	0.00	0.00	0.00	0.00	0.00	0.00	0.00	0.00	0.00	0.00	0.00	0.00	0.00	0.01	0.01	0.01	0.01	0.01
15.95	22.95	0.00	0.00	0.00	0.00	0.00	0.00	0.00	0.00	0.00	0.00	0.00	0.00	0.00	0.00	0.00	0.00	0.00	0.00	0.01	0.01	0.01	0.01	0.01
16.12	23.14	0.00	0.00	0.00	0.00	0.00	0.00	0.00	0.00	0.00	0.00	0.00	0.00	0.00	0.00	0.00	0.00	0.00	0.00	0.01	0.01	0.01	0.01	0.01
16.30	23.34	0.00	0.00	0.00	0.00	0.00	0.00	0.00	0.00	0.00	0.00	0.00	0.00	0.00	0.00	0.00	0.00	0.00	0.00	0.01	0.01	0.01	0.01	0.02
16.50	23.56	0.00	0.00	0.00	0.00	0.00	0.00	0.00	0.00	0.00	0.00	0.00	0.00	0.00	0.00	0.00	0.00	0.00	0.00	0.01	0.01	0.01	0.01	0.02
16.70	23.79	0.00	0.00	0.00	0.00	0.00	0.00	0.00	0.00	0.00	0.00	0.00	0.00	0.00	0.00	0.00	0.00	0.00	0.01	0.01	0.01	0.01	0.01	0.02
16.92	24.04	0.00	0.00	0.00	0.00	0.00	0.00	0.00	0.00	0.00	0.00	0.00	0.00	0.00	0.00	0.00	0.00	0.00	0.01	0.01	0.01	0.01	0.01	0.02
17.16	24.30	0.00	0.00	0.00	0.00	0.00	0.00	0.00	0.00	0.00	0.00	0.00	0.00	0.00	0.00	0.00	0.00	0.00	0.01	0.01	0.01	0.01	0.02	0.02
17.41	24.57	0.00	0.00	0.00	0.00	0.00	0.00	0.00	0.00	0.00	0.00	0.00	0.00	0.00	0.00	0.00	0.00	0.00	0.01	0.01	0.01	0.01	0.02	0.02
17.67	24.87	0.00	0.00	0.00	0.00	0.00	0.00	0.00	0.00	0.00	0.00	0.00	0.00	0.00	0.00	0.00	0.00	0.00	0.01	0.01	0.01	0.01	0.02	0.02
17.95	25.18	0.00	0.00	0.00	0.00	0.00	0.00	0.00	0.00	0.00	0.00	0.00	0.00	0.00	0.00	0.00	0.00	0.01	0.01	0.01	0.01	0.01	0.02	0.02
18.24	25.51	0.00	0.00	0.00	0.00	0.00	0.00	0.00	0.00	0.00	0.00	0.00	0.00	0.00	0.00	0.00	0.00	0.01	0.01	0.01	0.01	0.02	0.02	0.02
18.55	25.85	0.00	0.00	0.00	0.00	0.00	0.00	0.00	0.00	0.00	0.00	0.00	0.00	0.00	0.00	0.00	0.00	0.01	0.01	0.01	0.01	0.02	0.02	0.03
18.87	26.21	0.00	0.00	0.00	0.00	0.00	0.00	0.00	0.00	0.00	0.00	0.00	0.00	0.00	0.00	0.00	0.00	0.01	0.01	0.01	0.01	0.02	0.02	0.03
19.20	26.58	0.00	0.00	0.00	0.00	0.00	0.00	0.00	0.00	0.00	0.00	0.00	0.00	0.00	0.00	0.00	0.00	0.01	0.01	0.01	0.01	0.02	0.02	0.03
19.54	26.95	0.00	0.00	0.00	0.00	0.00	0.00	0.00	0.00	0.00	0.00	0.00	0.00	0.00	0.00	0.00	0.01	0.01	0.01	0.01	0.02	0.02	0.03	0.03
19.88	27.34	0.00	0.00	0.00	0.00	0.00	0.00	0.00	0.00	0.00	0.00	0.00	0.00	0.00	0.00	0.00	0.01	0.01	0.01	0.01	0.02	0.02	0.03	0.03
20.22	27.72	0.00	0.00	0.00	0.00	0.00	0.00	0.00	0.00	0.00	0.00	0.00	0.00	0.00	0.00	0.00	0.01	0.01	0.01	0.01	0.02	0.02	0.03	0.03
20.56	28.10	0.00	0.00	0.00	0.00	0.00	0.00	0.00	0.00	0.00	0.00	0.00	0.00	0.00	0.00	0.00	0.01	0.01	0.01	0.01	0.02	0.02	0.03	0.04

3.8 Hazard Curve

A fundamental outcome of PSHA is the relationship between the probability of exceedance within a given time interval and a measure of seismic intensity, which is known as a seismic hazard curve. Intensity Measures (IMs) characterize ground motions. The ground motion record aims to measure the "intensity" of the ground motion. IMs include parameters such as PGA and spectral acceleration Spa (f1).

Hazard curves from each source are computed separately resulting in independent values of M, and R obtained for each dominant source. The combining effects of all magnitudes and distance distributions and probability expression of ground motion for a given source are combined to produce a report of the probability that given the occurrence of a seismic event with a magnitude of interest anywhere on the source, the site PGA will exceed an acceleration of interest (Hall & Green , 1994). A hazard curve combines all of the above information into one plot. This is computed in probability computations as:

$$P(PGA > x) = \iint P(PGA > x/m, r) f_M(m) f_R(r) dm dr \qquad 3.23$$

The hazard curves give the merged effects of all magnitudes and distances on the probability of exceeding the specified ground motion level. In the analysis, there is more than one source to measure the rate of PGA >x considering all sources and M_j/R_k denote the magnitude /distribution for the nth source. This analysis is contributed by the summation form of discretized distribution M_j/R_k will be discretized into ΔM and ΔR increments respectively

$$P(PGA > x) = \sum_{j=1}^{n_M} \sum_{K=1}^{n_R} P(PGA > x \mid m_{j,} r_k) P(M = m_j) P(R = r_k) \qquad 3.24$$

Where

$f_M(m)$ - PDF for earthquake magnitude

$f_R(r)$- PDF for distance

P (PGA> x| mj, rk) - from GMPE model

ΔM- is an interval range for discretized earthquake magnitude

ΔR- is an interval range for discretized distan

Table 3.14: Probability of PGA greater than 0.05

PGA>x = PGA>0.05																							
Distance		**Magnitude**																					
R_{jb}	18																						
R_X	**R_{Rup}**	5.00	5.10	5.20	5.30	5.40	5.50	5.60	5.70	5.80	5.90	6.00	6.10	6.20	6.30	6.40	6.50	6.60	6.70	6.80	6.90	7.00	7.10	7.20
15.27	22.19	0.00	0.00	0.00	0.00	0.00	0.03	0.00	0.00	0.00	0.00	0.00	0.00	0.00	0.00	0.00	0.00	0.00	0.00	0.00	0.00	0.00	0.00	0.00
15.38	22.32	0.00	0.00	0.00	0.00	0.00	0.03	0.00	0.00	0.00	0.00	0.00	0.00	0.00	0.00	0.00	0.00	0.00	0.00	0.00	0.00	0.00	0.00	0.00
15.51	22.46	0.00	0.00	0.00	0.00	0.00	0.03	0.00	0.00	0.00	0.00	0.00	0.00	0.00	0.00	0.00	0.00	0.00	0.00	0.00	0.00	0.00	0.00	0.00
15.65	22.62	0.00	0.00	0.00	0.00	0.00	0.03	0.00	0.00	0.00	0.00	0.00	0.00	0.00	0.00	0.00	0.00	0.00	0.00	0.00	0.00	0.00	0.00	0.00
15.79	22.78	0.00	0.00	0.00	0.00	0.00	0.03	0.00	0.00	0.00	0.00	0.00	0.00	0.00	0.00	0.00	0.00	0.00	0.00	0.00	0.00	0.00	0.00	0.00
15.95	22.95	0.00	0.00	0.00	0.00	0.00	0.03	0.00	0.00	0.00	0.00	0.00	0.00	0.00	0.00	0.00	0.00	0.00	0.00	0.00	0.00	0.00	0.00	0.00
16.12	23.14	0.00	0.00	0.00	0.00	0.00	0.03	0.00	0.00	0.00	0.00	0.00	0.00	0.00	0.00	0.00	0.00	0.00	0.00	0.00	0.00	0.00	0.00	0.00
16.30	23.34	0.00	0.00	0.00	0.00	0.00	0.04	0.00	0.00	0.00	0.00	0.00	0.00	0.00	0.00	0.00	0.00	0.00	0.00	0.00	0.00	0.00	0.00	0.00
16.50	23.56	0.00	0.00	0.00	0.00	0.00	0.04	0.00	0.00	0.00	0.00	0.00	0.00	0.00	0.00	0.00	0.00	0.00	0.00	0.00	0.00	0.00	0.00	0.00
16.70	23.79	0.00	0.00	0.00	0.00	0.00	0.04	0.00	0.00	0.00	0.00	0.00	0.00	0.00	0.00	0.00	0.00	0.00	0.00	0.00	0.00	0.00	0.00	0.00
16.92	24.04	0.00	0.00	0.00	0.00	0.00	0.04	0.00	0.00	0.00	0.00	0.00	0.00	0.00	0.00	0.00	0.00	0.00	0.00	0.00	0.00	0.00	0.00	0.00
17.16	24.30	0.00	0.00	0.00	0.00	0.00	0.04	0.00	0.00	0.00	0.00	0.00	0.00	0.00	0.00	0.00	0.00	0.00	0.00	0.00	0.00	0.00	0.00	0.00
17.41	24.57	0.00	0.00	0.00	0.00	0.00	0.04	0.00	0.00	0.00	0.00	0.00	0.00	0.00	0.00	0.00	0.00	0.00	0.00	0.00	0.00	0.00	0.00	0.00
17.67	24.87	0.00	0.00	0.00	0.00	0.00	0.04	0.00	0.00	0.00	0.00	0.00	0.00	0.00	0.00	0.00	0.00	0.00	0.00	0.00	0.00	0.00	0.00	0.00
17.95	25.18	0.00	0.00	0.00	0.00	0.00	0.04	0.00	0.00	0.00	0.00	0.00	0.00	0.00	0.00	0.00	0.00	0.00	0.00	0.00	0.00	0.00	0.00	0.00
18.24	25.51	0.00	0.00	0.00	0.00	0.00	0.04	0.00	0.00	0.00	0.00	0.00	0.00	0.00	0.00	0.00	0.00	0.00	0.00	0.00	0.00	0.00	0.00	0.00
18.55	25.85	0.00	0.00	0.00	0.00	0.00	0.04	0.00	0.00	0.00	0.00	0.00	0.00	0.00	0.00	0.00	0.00	0.00	0.00	0.00	0.00	0.00	0.00	0.00
18.87	26.21	0.00	0.00	0.00	0.00	0.00	0.04	0.00	0.00	0.00	0.00	0.00	0.00	0.00	0.00	0.00	0.00	0.00	0.00	0.00	0.00	0.00	0.00	0.00
19.20	26.58	0.00	0.00	0.00	0.00	0.00	0.04	0.00	0.00	0.00	0.00	0.00	0.00	0.00	0.00	0.00	0.00	0.00	0.00	0.00	0.00	0.00	0.00	0.00
19.54	26.95	0.00	0.00	0.00	0.00	0.00	0.04	0.00	0.00	0.00	0.00	0.00	0.00	0.00	0.00	0.00	0.00	0.00	0.00	0.00	0.00	0.00	0.00	0.00
19.88	27.34	0.00	0.00	0.00	0.00	0.00	0.04	0.00	0.00	0.00	0.00	0.00	0.00	0.00	0.00	0.00	0.00	0.00	0.00	0.00	0.00	0.00	0.00	0.00
20.22	27.72	0.00	0.00	0.00	0.00	0.00	0.04	0.00	0.00	0.00	0.00	0.00	0.00	0.00	0.00	0.00	0.00	0.00	0.00	0.00	0.00	0.00	0.00	0.00
20.56	28.10	0.00	0.00	0.00	0.00	0.00	0.04	0.00	0.00	0.00	0.00	0.00	0.00	0.00	0.00	0.00	0.00	0.00	0.00	0.00	0.00	0.00	0.00	0.00
		1.04																						

Table 3.15: Probability of PGA greater than 0.8

PGA>x = PGA>0.8																							
Distance		**Magnitude**																					
R_{jb}	18.0																						
R_X	**R_{Rup}**	5.0	5.1	5.2	5.3	5.4	5.5	5.6	5.7	5.8	5.9	6.0	6.1	6.2	6.3	6.4	6.5	6.6	6.7	6.8	6.9	7.0	7.1	7.2
15.3	22.2	0.0	0.0	0.0	0.0	0.0	0.0	0.0	0.0	0.0	0.0	0.0	0.0	0.0	0.0	0.0	0.0	0.0	0.0	0.0	0.0	0.0	0.0	0.0
15.4	22.3	0.0	0.0	0.0	0.0	0.0	0.0	0.0	0.0	0.0	0.0	0.0	0.0	0.0	0.0	0.0	0.0	0.0	0.0	0.0	0.0	0.0	0.0	0.0
15.5	22.5	0.0	0.0	0.0	0.0	0.0	0.0	0.0	0.0	0.0	0.0	0.0	0.0	0.0	0.0	0.0	0.0	0.0	0.0	0.0	0.0	0.0	0.0	0.0
15.6	22.6	0.0	0.0	0.0	0.0	0.0	0.0	0.0	0.0	0.0	0.0	0.0	0.0	0.0	0.0	0.0	0.0	0.0	0.0	0.0	0.0	0.0	0.0	0.0
15.8	22.8	0.0	0.0	0.0	0.0	0.0	0.0	0.0	0.0	0.0	0.0	0.0	0.0	0.0	0.0	0.0	0.0	0.0	0.0	0.0	0.0	0.0	0.0	0.0
16.0	23.0	0.0	0.0	0.0	0.0	0.0	0.0	0.0	0.0	0.0	0.0	0.0	0.0	0.0	0.0	0.0	0.0	0.0	0.0	0.0	0.0	0.0	0.0	0.0
16.1	23.1	0.0	0.0	0.0	0.0	0.0	0.0	0.0	0.0	0.0	0.0	0.0	0.0	0.0	0.0	0.0	0.0	0.0	0.0	0.0	0.0	0.0	0.0	0.0
16.3	23.3	0.0	0.0	0.0	0.0	0.0	0.0	0.0	0.0	0.0	0.0	0.0	0.0	0.0	0.0	0.0	0.0	0.0	0.0	0.0	0.0	0.0	0.0	0.0
16.5	23.6	0.0	0.0	0.0	0.0	0.0	0.0	0.0	0.0	0.0	0.0	0.0	0.0	0.0	0.0	0.0	0.0	0.0	0.0	0.0	0.0	0.0	0.0	0.0
16.7	23.8	0.0	0.0	0.0	0.0	0.0	0.0	0.0	0.0	0.0	0.0	0.0	0.0	0.0	0.0	0.0	0.0	0.0	0.0	0.0	0.0	0.0	0.0	0.0
16.9	24.0	0.0	0.0	0.0	0.0	0.0	0.0	0.0	0.0	0.0	0.0	0.0	0.0	0.0	0.0	0.0	0.0	0.0	0.0	0.0	0.0	0.0	0.0	0.0
17.2	24.3	0.0	0.0	0.0	0.0	0.0	0.0	0.0	0.0	0.0	0.0	0.0	0.0	0.0	0.0	0.0	0.0	0.0	0.0	0.0	0.0	0.0	0.0	0.0
17.4	24.6	0.0	0.0	0.0	0.0	0.0	0.0	0.0	0.0	0.0	0.0	0.0	0.0	0.0	0.0	0.0	0.0	0.0	0.0	0.0	0.0	0.0	0.0	0.0
17.7	24.9	0.0	0.0	0.0	0.0	0.0	0.0	0.0	0.0	0.0	0.0	0.0	0.0	0.0	0.0	0.0	0.0	0.0	0.0	0.0	0.0	0.0	0.0	0.0
17.9	25.2	0.0	0.0	0.0	0.0	0.0	0.0	0.0	0.0	0.0	0.0	0.0	0.0	0.0	0.0	0.0	0.0	0.0	0.0	0.0	0.0	0.0	0.0	0.0
18.2	25.5	0.0	0.0	0.0	0.0	0.0	0.0	0.0	0.0	0.0	0.0	0.0	0.0	0.0	0.0	0.0	0.0	0.0	0.0	0.0	0.0	0.0	0.0	0.0
18.5	25.8	0.0	0.0	0.0	0.0	0.0	0.0	0.0	0.0	0.0	0.0	0.0	0.0	0.0	0.0	0.0	0.0	0.0	0.0	0.0	0.0	0.0	0.0	0.0
18.9	26.2	0.0	0.0	0.0	0.0	0.0	0.0	0.0	0.0	0.0	0.0	0.0	0.0	0.0	0.0	0.0	0.0	0.0	0.0	0.0	0.0	0.0	0.0	0.0
19.2	26.6	0.0	0.0	0.0	0.0	0.0	0.0	0.0	0.0	0.0	0.0	0.0	0.0	0.0	0.0	0.0	0.0	0.0	0.0	0.0	0.0	0.0	0.0	0.0
19.5	27.0	0.0	0.0	0.0	0.0	0.0	0.0	0.0	0.0	0.0	0.0	0.0	0.0	0.0	0.0	0.0	0.0	0.0	0.0	0.0	0.0	0.0	0.0	0.0
19.9	27.3	0.0	0.0	0.0	0.0	0.0	0.0	0.0	0.0	0.0	0.0	0.0	0.0	0.0	0.0	0.0	0.0	0.0	0.0	0.0	0.0	0.0	0.0	0.0
20.2	27.7	0.0	0.0	0.0	0.0	0.0	0.0	0.0	0.0	0.0	0.0	0.0	0.0	0.0	0.0	0.0	0.0	0.0	0.0	0.0	0.0	0.0	0.0	0.0
20.6	28.1	0.0	0.0	0.0	0.0	0.0	0.0	0.0	0.0	0.0	0.0	0.0	0.0	0.0	0.0	0.0	0.0	0.0	0.0	0.0	0.0	0.0	0.0	0.0
Sum		0.0006																						

The above-mentioned probability expression gives the probability of exceedance of a given earthquake and does not take into consideration the probability occurrence of the earthquake. By the product of the annual occurrence rate of the earthquake and the probability of exceedance of the ground motion. To compute the probability of occurrence of an earthquake, rate of PGA>x by Equation 3.25.

$$\lambda(PGA > x) = \lambda(M_j > m_{min}) \sum_{j=1}^{n_M} \sum_{K=1}^{n_R} P(PGA > x | m_{j,} r_k) P(M = m_j) P(R = r_k) \qquad 3.25$$

Where λ (M > m_{min}) is the rate of occurrence of earthquakes greater than m_{min} from the source, and λ (PGA> x) is the rate of PGA > x.

For ground shaking more than one source of the site, the annual rate exceedance will be computed by the sum of the rates of PGA > x from each source, Equation 3.25 is modified as shown in Equation 3.26

Table 3.16 Annual rate of exceedance

$$\lambda(PGA > x) = \sum_{i=1}^{n_{source}} \lambda\,(M_j > m_{min}) \sum_{j=1}^{n_M} \sum_{K=1}^{n_R} P(PGA > x |\, m_{j,} r_k) P(M = m_j) P(R = r_k) \qquad 3.26$$

X	P(PGA>X)	$\lambda(M_j > m_{min})$	λ(PGA > x)
0.05	1.0407	0.0127	0.0132
0.1	0.2658	0.0127	0.0034
0.15	0.0993	0.0127	0.0013
0.2	0.0460	0.0127	0.0006
0.25	0.0245	0.0127	0.0003
0.3	0.0144	0.0127	0.0002
0.35	0.0091	0.0127	0.0001
0.4	0.0060	0.0127	0.0001
0.45	0.0042	0.0127	0.0001
0.5	0.0030	0.0127	0.0000
0.55	0.0022	0.0127	0.0000
0.6	0.0016	0.0127	0.0000
0.65	0.0013	0.0127	0.0000
0.7	0.0010	0.0127	0.0000
0.75	0.0008	0.0127	0.0000
0.8	0.0006	0.0127	0.0000

The hazard curve is a plot of the annual frequency of exceedance versus peak ground acceleration. The hazard curve for peak ground acceleration is shown in Figure 3.6.

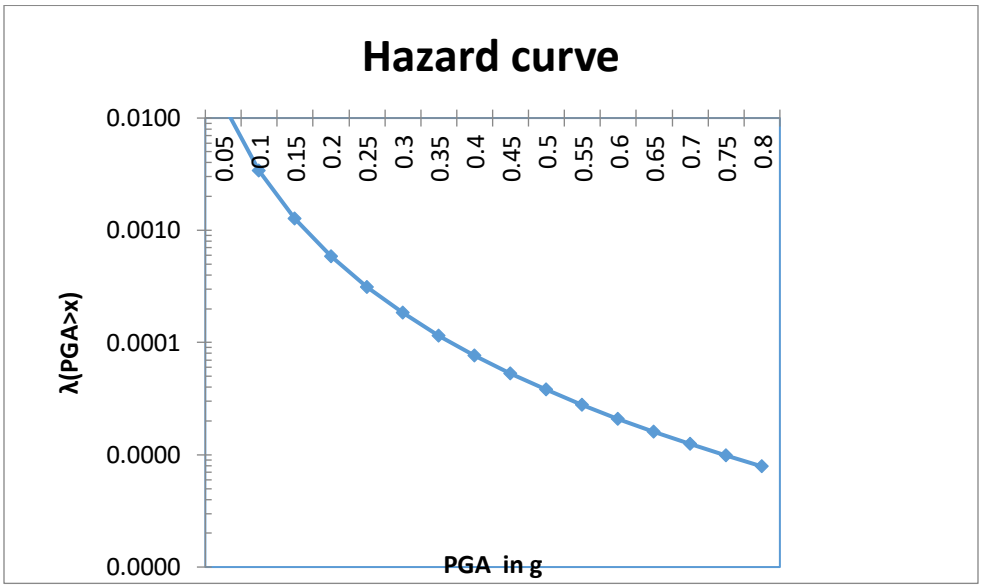

Figure 3.6: Hazard Curve for the specific site

3.9 Disaggregation of the Seismic Hazard

For each seismic source, PSHA accounts for all magnitudes and their relative probability of occurring within the defined range of Mmin to Mmax. Besides, for each source and M combination, all possible site-source distances are considered, along with their relative probabilities. Finally, for each magnitude and distance combination, make the most significant contributions to the seismic hazard to determine the maximum considered earthquake (PGA) is necessary to "deaggregate".

The resulting rate of exceedance values evaluated by integrating all contributions from several sources for each related magnitude and source-to-site distance is called the disaggregation of PSHA (also called deaggregation of PSHA). The disaggregation provides the contribution of earthquake events in terms of their Magnitude and distance. The disaggregation is the combined PDF of m and r conditioned upon exceedance of a specified significant intensity measure FHWA (2014).

The response spectra for 5% damping ratio obtained according to the NEHRP Guidelines for Seismic Rehabilitation of Buildings (FEMA-273) with the ground motions from National Seismic Hazard Mapping Project by the U.S. Geological Survey (USGS) for 50%, 10%, 5%, and 2% probability of exceedance in 50 years.

Song (2018) cited ACI 318-08 and ASCE 7-05 recommended the Maximum Considered Earthquake (MCE) for no collapse requirement and Design Basis Earthquake (DBE) for damage limitation requirement. 10% and 2% probability of exceedance in 50 years are the reference seismic actions that are used to describe design seismic action for damage limitation and no collapse requirement respectively.10%, and 2% probability of exceedance in 50 years or corresponding return periods of 475, and 2,475 years respectively.

Disaggregation identifies the source, distance, and ground motion percentiles that contribute most strongly to the computed hazard. Dividing the total hazard into contributions based on distance and magnitude for the rate of an earthquake by the rate of all earthquakes Bazzurro and Cornell, (1999), McGuire, (1995).

The parameters involved in the distribution of magnitudes and distance are discretized so that it will be described in terms of percentage contribution to PGA>x as (Baker, 2008)

$$P(M = m, R = r/PGA > x \frac{\lambda(PGA>x, M=m, R=r)}{\lambda(PGA>x)} \quad 3.27$$

$$\lambda(PGA > x, M = m, R = r) = P(M_i = m)P(R_i = r)\sum_{k=1}^{n_s} \lambda(M_i > m_{min})P(PGA > x/\, m_j, r_k) \quad 3.28$$

There are two types of deaggregations are usually implemented. The first one is the magnitude, distance, and epsilon (Harmsen et.al 1999). The second is azimuth, distance, and magnitude (Bazurro and Cornell, 1999; Harmsen and Frankel, 2001) this deaggregation process is called as 3D hazard deaggregation.

In this thesis, 2D hazard deaggregation applicable by using the M-R distribution and excluding the number of standard deviation from the median. In this method, the magnitude range is discretized within an equal space of 0.1.

Table 3.17 Disaggregation

Distance		R=rk	Magnitude																					
Rjb			5	5.1	5.2	5.3	5.4	5.5	5.6	5.7	5.8	5.9	6	6.1	6.2	6.3	6.4	6.5	6.6	6.7	6.8	6.9	7	7.1	7.2
18			0.166	0.139	0.116	0.097	0.082	0.068	0.057	0.048	0.040	0.034	0.028	0.024	0.020	0.017	0.014	0.012	0.010	0.008	0.007	0.006	0.005	0.004	0.001
RX	Rrup		P(M=mj, R=rk|x>0.13) = [λ(Mj>mmin)P(x>0.13|mj,rk)P(M=mj)P(R=rk)]/λ(x>0.13)																						
15.265	22.19	0.0435	2.4E-06	5.5E-06	1.1E-05	1.8E-05	2.8E-05	4.0E-05	5.3E-05	6.6E-05	7.8E-05	8.9E-05	9.8E-05	1.0E-04	1.1E-04	1.1E-04	1.1E-04	1.1E-04	1.0E-04	9.6E-05	9.0E-05	8.3E-05	7.5E-05	6.9E-05	1.9E-05
15.3834	22.32	0.0435	2.4E-06	5.6E-06	1.1E-05	1.9E-05	2.9E-05	4.1E-05	5.4E-05	6.7E-05	8.0E-05	9.1E-05	1.0E-04	1.1E-04	1.1E-04	1.1E-04	1.1E-04	1.1E-04	1.0E-04	9.8E-05	9.1E-05	8.4E-05	7.7E-05	7.0E-05	1.9E-05
15.5107	22.46	0.0435	2.5E-06	5.7E-06	1.1E-05	1.9E-05	2.9E-05	4.1E-05	5.5E-05	6.8E-05	8.1E-05	9.3E-05	1.0E-04	1.1E-04	1.1E-04	1.1E-04	1.1E-04	1.1E-04	1.1E-04	1.0E-04	9.3E-05	8.5E-05	7.8E-05	7.1E-05	1.9E-05
15.6476	22.62	0.0435	2.6E-06	5.8E-06	1.1E-05	1.9E-05	3.0E-05	4.2E-05	5.6E-05	7.0E-05	8.3E-05	9.5E-05	1.0E-04	1.1E-04	1.2E-04	1.2E-04	1.2E-04	1.1E-04	1.1E-04	1.0E-04	9.4E-05	8.7E-05	7.9E-05	7.2E-05	1.9E-05
15.7946	22.78	0.0435	2.6E-06	6.0E-06	1.2E-05	2.0E-05	3.1E-05	4.3E-05	5.7E-05	7.2E-05	8.5E-05	9.7E-05	1.1E-04	1.1E-04	1.2E-04	1.2E-04	1.2E-04	1.1E-04	1.1E-04	1.0E-04	9.6E-05	8.8E-05	8.0E-05	7.3E-05	2.0E-05
15.9524	22.95	0.0435	2.7E-06	6.1E-06	1.2E-05	2.0E-05	3.1E-05	4.5E-05	5.9E-05	7.3E-05	8.7E-05	9.9E-05	1.1E-04	1.2E-04	1.2E-04	1.2E-04	1.2E-04	1.2E-04	1.1E-04	1.1E-04	9.8E-05	9.0E-05	8.2E-05	7.4E-05	2.0E-05
16.1215	23.14	0.0435	2.7E-06	6.3E-06	1.2E-05	2.1E-05	3.2E-05	4.6E-05	6.0E-05	7.5E-05	8.9E-05	1.0E-04	1.1E-04	1.2E-04	1.2E-04	1.2E-04	1.2E-04	1.2E-04	1.1E-04	1.1E-04	1.0E-04	9.1E-05	8.3E-05	7.6E-05	2.0E-05
16.3025	23.34	0.0435	2.8E-06	6.4E-06	1.3E-05	2.1E-05	3.3E-05	4.7E-05	6.2E-05	7.7E-05	9.2E-05	1.0E-04	1.1E-04	1.2E-04	1.3E-04	1.3E-04	1.3E-04	1.2E-04	1.2E-04	1.1E-04	1.0E-04	9.3E-05	8.5E-05	7.7E-05	2.1E-05
16.4962	23.56	0.0435	2.8E-06	6.6E-06	1.3E-05	2.2E-05	3.4E-05	4.8E-05	6.4E-05	7.9E-05	9.4E-05	1.1E-04	1.2E-04	1.3E-04	1.3E-04	1.3E-04	1.3E-04	1.2E-04	1.2E-04	1.1E-04	1.0E-04	9.5E-05	8.6E-05	7.8E-05	2.1E-05
16.703	23.79	0.0435	2.9E-06	6.7E-06	1.3E-05	2.3E-05	3.5E-05	5.0E-05	6.5E-05	8.2E-05	9.7E-05	1.1E-04	1.2E-04	1.3E-04	1.3E-04	1.3E-04	1.3E-04	1.3E-04	1.2E-04	1.1E-04	1.1E-04	9.7E-05	8.8E-05	8.0E-05	2.1E-05
16.9234	24.04	0.0435	3.0E-06	6.9E-06	1.3E-05	2.3E-05	3.6E-05	5.1E-05	6.7E-05	8.4E-05	1.0E-04	1.1E-04	1.2E-04	1.3E-04	1.4E-04	1.4E-04	1.4E-04	1.3E-04	1.2E-04	1.2E-04	1.1E-04	9.9E-05	9.0E-05	8.1E-05	2.2E-05
17.158	24.30	0.0435	3.0E-06	7.0E-06	1.4E-05	2.4E-05	3.7E-05	5.2E-05	6.9E-05	8.6E-05	1.0E-04	1.2E-04	1.3E-04	1.4E-04	1.4E-04	1.4E-04	1.4E-04	1.3E-04	1.3E-04	1.2E-04	1.1E-04	1.0E-04	9.1E-05	8.3E-05	2.2E-05
17.407	24.57	0.0435	3.1E-06	7.2E-06	1.4E-05	2.4E-05	3.8E-05	5.4E-05	7.1E-05	8.9E-05	1.1E-04	1.2E-04	1.3E-04	1.4E-04	1.4E-04	1.4E-04	1.4E-04	1.4E-04	1.3E-04	1.2E-04	1.1E-04	1.0E-04	9.3E-05	8.4E-05	2.3E-05
17.6708	24.87	0.0435	3.1E-06	7.3E-06	1.4E-05	2.5E-05	3.9E-05	5.5E-05	7.3E-05	9.1E-05	1.1E-04	1.2E-04	1.3E-04	1.4E-04	1.5E-04	1.5E-04	1.5E-04	1.4E-04	1.3E-04	1.2E-04	1.2E-04	1.1E-04	9.5E-05	8.6E-05	2.3E-05
17.9492	25.18	0.0435	3.2E-06	7.5E-06	1.5E-05	2.6E-05	4.0E-05	5.7E-05	7.5E-05	9.4E-05	1.1E-04	1.3E-04	1.4E-04	1.5E-04	1.5E-04	1.5E-04	1.5E-04	1.4E-04	1.4E-04	1.3E-04	1.2E-04	1.1E-04	9.7E-05	8.8E-05	2.4E-05
18.2422	25.51	0.0435	3.2E-06	7.6E-06	1.5E-05	2.6E-05	4.1E-05	5.8E-05	7.7E-05	9.6E-05	1.1E-04	1.3E-04	1.4E-04	1.5E-04	1.6E-04	1.6E-04	1.5E-04	1.5E-04	1.4E-04	1.3E-04	1.2E-04	1.1E-04	9.9E-05	9.0E-05	2.4E-05
18.549	25.85	0.0435	3.3E-06	7.7E-06	1.5E-05	2.7E-05	4.2E-05	5.9E-05	7.9E-05	9.9E-05	1.2E-04	1.3E-04	1.5E-04	1.5E-04	1.6E-04	1.6E-04	1.6E-04	1.5E-04	1.4E-04	1.3E-04	1.2E-04	1.1E-04	1.0E-04	9.1E-05	2.4E-05
18.8686	26.21	0.0435	3.3E-06	7.8E-06	1.6E-05	2.7E-05	4.3E-05	6.1E-05	8.1E-05	1.0E-04	1.2E-04	1.4E-04	1.5E-04	1.6E-04	1.6E-04	1.6E-04	1.6E-04	1.5E-04	1.5E-04	1.4E-04	1.3E-04	1.1E-04	1.0E-04	9.3E-05	2.5E-05
19.1993	26.58	0.0435	3.3E-06	7.9E-06	1.6E-05	2.8E-05	4.3E-05	6.2E-05	8.3E-05	1.0E-04	1.2E-04	1.4E-04	1.5E-04	1.6E-04	1.7E-04	1.7E-04	1.6E-04	1.6E-04	1.5E-04	1.4E-04	1.3E-04	1.2E-04	1.1E-04	9.5E-05	2.5E-05
19.5384	26.95	0.0435	3.3E-06	8.0E-06	1.6E-05	2.8E-05	4.4E-05	6.3E-05	8.5E-05	1.1E-04	1.3E-04	1.4E-04	1.6E-04	1.7E-04	1.7E-04	1.7E-04	1.7E-04	1.6E-04	1.5E-04	1.4E-04	1.3E-04	1.2E-04	1.1E-04	9.7E-05	2.6E-05
19.8822	27.34	0.0435	3.3E-06	8.0E-06	1.6E-05	2.8E-05	4.5E-05	6.5E-05	8.6E-05	1.1E-04	1.3E-04	1.5E-04	1.6E-04	1.7E-04	1.8E-04	1.8E-04	1.7E-04	1.7E-04	1.6E-04	1.5E-04	1.3E-04	1.2E-04	1.1E-04	9.8E-05	2.6E-05
20.225	27.72	0.0435	3.3E-06	8.0E-06	1.6E-05	2.9E-05	4.5E-05	6.6E-05	8.8E-05	1.1E-04	1.3E-04	1.5E-04	1.6E-04	1.7E-04	1.8E-04	1.8E-04	1.8E-04	1.7E-04	1.6E-04	1.5E-04	1.4E-04	1.2E-04	1.1E-04	1.0E-04	2.7E-05
20.5586	28.10	0.0435	3.3E-06	8.0E-06	1.6E-05	2.9E-05	4.6E-05	6.6E-05	8.9E-05	1.1E-04	1.3E-04	1.5E-04	1.7E-04	1.8E-04	1.8E-04	1.8E-04	1.8E-04	1.7E-04	1.6E-04	1.5E-04	1.4E-04	1.3E-04	1.1E-04	1.0E-04	2.7E-05

3.10 Ground Motion Selection

Ground motions are selected and scaled to enable response-history analysis that supports either design or performance assessment. Seismic design analysis requires time history analysis to apply seismic load on structural and geotechnical analysis and design. To define seismic load as input to dynamic analysis the selection of ground motion is the main stage in defining the seismic load input of structural analysis. There are no accelerogram records for Ethiopian earthquakes, other records should be adapted so that ground motion selection is required. Ground motion selection utilizes deaggregation results of magnitude and distance to identify causal events for a given target spectra value associated with an annual rate of exceedance (Lin and Baker, 2011).

The parameters that affect to select Ground motion records and have influence ground motion spectral shape (Graizer and Kalkan 2009):

-Earthquake Magnitude

- Source to site distance
- Site-condition (shear wave velocity in the upper 30-meters -Vs30)
- Rupture mechanism

Ground motion scaling and spectral matching are generally used to adjust the earthquake records to match a specific target response spectrum. These could be actual time history or artificial time history. To generate artificial earthquake ground motions whose characteristics are consistent with both the physical condition of interest and the characteristics of the actual recorded ground motions. There are typical practices in structural engineers to select seven ground motions (Haselton et al., 2012).

The Pacific Earthquake Engineering Research (PEER) Center, NGA strong motion database was used for this study due to the absence of recorded accelerogram data for Ethiopia. In this study earthquakes from subduction zones are rejected because Ethiopia is located in the shallow crustal Zone. Magnitude and distance of the design earthquake along with shear velocity of the top 30m and fault mechanism of the specified area are the input factor for the selection of acceleration time history from PEER ground motion database. In this thesis, the selection was carried out with magnitudes between 5.5 to 5.7 and rupture distance (Rrup) range from 15 to 30 km as obtained from disaggregation calculation.

The selection and scaling of earthquake ground motions play a big role to apply seismic load on the model during structural analysis. Acceleration time histories have been selected from previously recorded database. Even though it is necessary to have seven motions for nonlinear analysis, PEER ground motion database gives four recorded ground motion for the given input factor.

Four ground motion are selected, the fault mechanism of the three ground motions is normal while one ground motion has been obtained for Normal oblique faulting mechanism. The PGA calculation has been done using normal slip, the dominant fault mechanism is normal fault. Therefore, the ground motion with the normal faulting mechanism is selected. Description of this selected ground motion is provided in Table 3.18.

Table 3.18 selected ground motion from PEER

PEER Ground Motion Database Time Series Search Report NGA -West2-2019-3-18							
Earthquake Name	Year	Station Name	Magnitude	Mechanism	Rjb (km)	Rrup (km)	Vs30 (m/sec)
"Umbria Marche (foreshock)_ Italy"	1997	"Borgo-Cerreto Torre"	5.7	Normal	19.65	21.31	519

The selected ground motion is applied at the base of the model. PGA selected from the recorded earthquake is 0.163g. This PGA is used to scale the calculated PGA from PSHA value 0.13g. The scaling factor of the PGA is becomes

$$\frac{0.13}{0.163} = 0.797$$

The most commonly employed ground motion scaling method involves multiplying all of the acceleration values of the time-acceleration pairs by a scalar value. This time domain scaling modifies the amplitude of the accelerations without affecting the frequency content or phasing.

$$Z = 0.8 * 0.797 * 9.81 \ {}^{m}/_{s^2}/_{g} = 6.25$$

The actual and the scaled time acceleration history are shown in the Figure 3.7 and Figure 3.8 respectively.

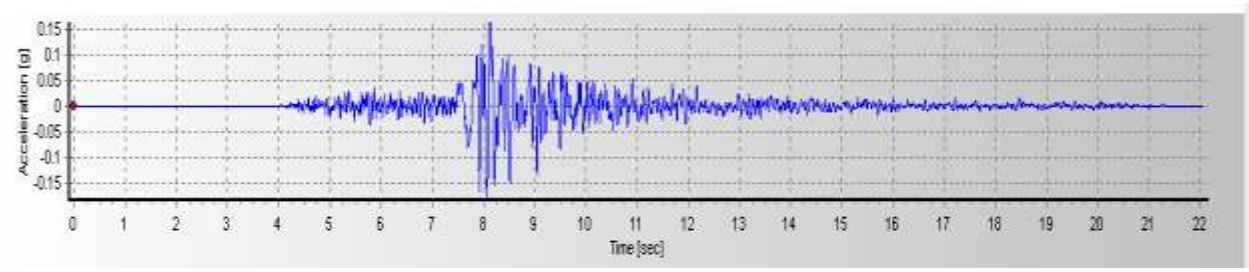

Figure 3.7: Time acceleration history of selected ground motion (PEER Database 2019)

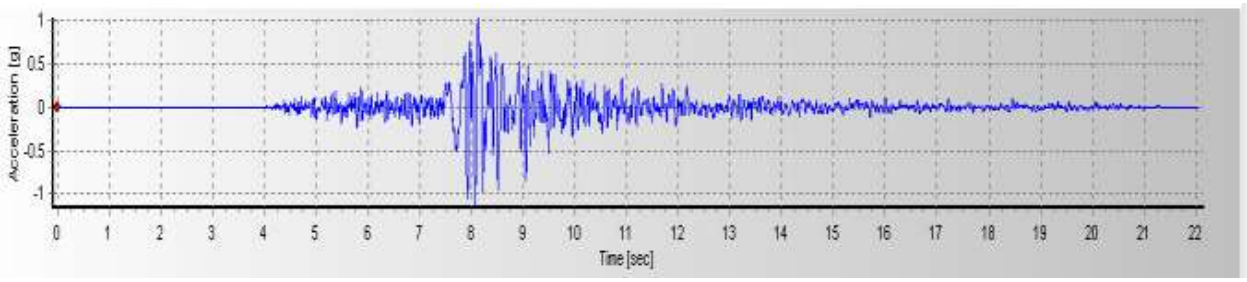

Figure 3.8: Scaled or artificial time acceleration history

CHAPTER 4 NUMERICAL MODELING

4.1 Introduction

In this thesis, the Finite Element Method (FEM) software ABAQUS is used to model three dimensional soil-pile system to investigate the behavior of pile under seismic excitation. Finite Element Method is used to select the proper techniques on pile-soil system under dynamic loading condition. To develop load-displacement curve of pile-soil system the important components of numerical model are, pile and soil element, mesh size, constitutive models to represent material behavior of soil and pile, soil-pile interface behavior, damping, boundary conditions, and loading steps.

4.2 Soil Geometry and Properties

In this study, four layered silt clay soil with Mohor-Coloumb constitutive model is used. The soil parameters, as obtained from the geotechnical investigation of the site, are given in Table 4.1. The soil is assumed to be in dry state to avoid liquefaction problem. As shown in Figure 4.1 the selected soil is equal to 20 times diameter of pile (20D) and 30 m tall (Sun & Mintaek, 2019).

Table 4.1 Soil properties on different layers

	Thickness	**Unit Weight**	**Young's modulus**	**Poisson's ratio**	**Friction Angle**	**Cohesion**
Symbol		**ɣ**	**E**	**V**	**Φ**	**c**
Unit	m	kN / m^3	MPa	0.3	Degree	kPa
Layer 1	4.5	17	8	0.3	18	12
Layer 2	6	19	15	0.3	22	15
Layer 3	4.5	20	35	0.3	24	20
Layer 4	15	21	40	0.3	26	25

4.3 Pile Geometry and Properties

In ABAQUS there are two ways of pile modeling: beam and volume pile. Volume pile type is used for this study. 0.6 m and 0.8 m diameters of pile with length of 15 m have been considered. Pile parameters are tabulated in Table 4.2.

Table 4.2: Properties of pile

No	Parameters	Unit	Value
1	Unit Weight	kN /m^3	25
2	Young's modulus	GPa	30
3	Poisson's ratio	NA	0.15
4	Pile diameter	m	0.6 and 0.8
5	Pile length	m	15
6	Pile head	NA	Free

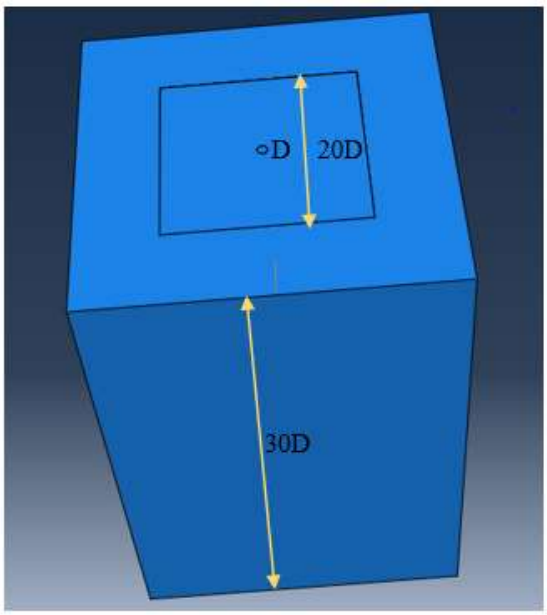

Figure 4.1: Soil and pile is modeled as a solid cylinder

4.4 Selection of Element Types

To assess the accuracy of element types, the following verification study is conducted. A cantilever beam fixed at the base with a point load acting at its free tip, is taken as the analysis subject (Figure 4.2). To verify the study, static deflection using ABAQUS model and analytical exact solution has been compared. This verification study is also reported in (ABAQUS Documentation, 2010)

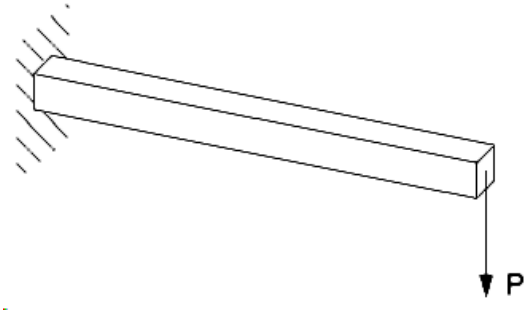

Figure 4.2: Cantilever beam under a point load P at its free end (ABAQUS Documentation, 2010)

$$y = \frac{PL^3}{3EI} \qquad 4.1$$

y= Deflection at the point considered
E= Young's modulus of the beam
I= Second moment of area of the beam
L= length of the beam
P= Applied load at the free end

Elastic parameters are selected as, elasticity modulus E = 30 GPa, Poisson's ratio ν = 0.15. Dimensions of the beam are selected as 150 mm long, 2.5 mm wide, and 5 mm deep. Magnitude of the point load at free end is selected as 5 N. Hence, exact solution for vertical deflection of the free tip is found as 7.2 mm from Equation 4.1.

The element types C3D8R and C3D8I are linear bricks with 8 nodes, with the first type using reduced integration and the second type utilizes something called incompatible modes, which improves the bending behavior by introducing internal deformation modes to the elements (ABAQUS Documentation, 2010) . This prevents shear locking and correctly estimates the stiffness of the elements, leading to a more accurate stress prediction compared to regular linear element types, such as C3D8R

and C3D8. Fully integrated elements will always give a better result than reduced integrated, but at a higher computational cost.

In Table 4.3 it can be observed that the deflection results when using C3D8I, C3D20, and C3D20R elements have given accurate results as compared to the exact solution, and for the C3D8R-elements the deflection is somewhat larger. All elements except C3D8R yield results with less than 1% error. Closest result to the exact solution is obtained from analyses utilizing C3D20R elements with error less than 0.1%.

Table 4.3: Element selection with two different mesh size

Mesh Type	C3D8R	C3D8I	C3D20	C3D20R
6x2x1	94.74	0.976	0.954	0.57
12x2x1	95.06	0.69	0.628	0.44

For all mesh types, the order of elements yielding closest result to the exact solution does not change. This order, from most accurate to least accurate, is C3D20R - C3D20 - C3D8I -C3D8R. The order of element types from most expensive to the cheapest, from computational cost point of view, is reported by (ABAQUS Documentation, 2010) as C3D20 - C3D20R - C3D8I- C3D8R. Note that although C3D20R is computationally cheaper than C3D20, it provides better accuracy.

The pile was modeled C3D8I solid element, meaning linear brick elements with 8 nodes with incompatible modes.

The soil was modeled into two regions, near field region and a far-field region. In Table 4.3 it can be observed that the result when using C3D8I, C3D20, and C3D20R are good results and the errors are less than 1%. The linear C3D8I elements will be used instead of C3D20R elements to improve the computational time.

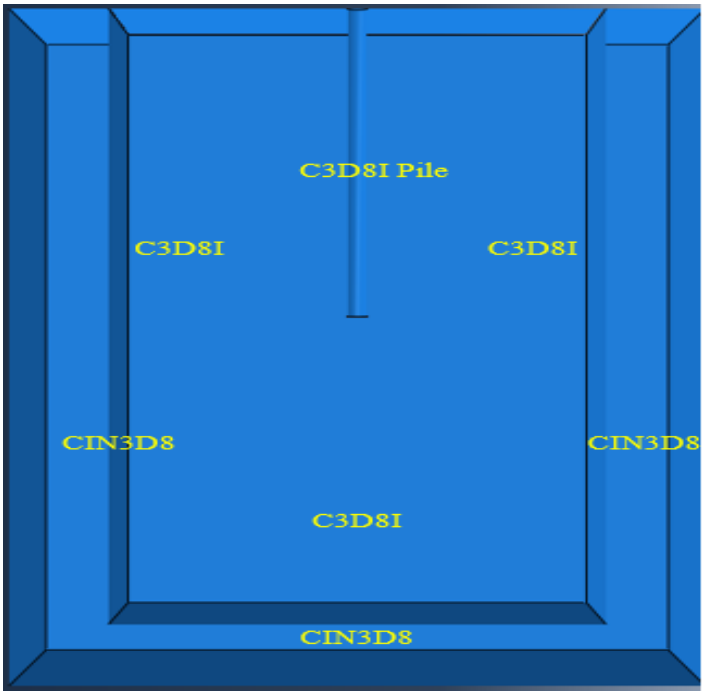

Figure 4.3: Assembly of soil and pile element type (section view)

4.5 Material Models

The proper selection of constitutive models for material behavior is important in numerical modeling. The pile is modeled using linear elastic model (Bentley & Naggar, 2000). A simple elastic-perfectly plastic model can simulate the behavior of soil with a sufficient accuracy though there are different ways to incorporate the plastic behavior of soil (Bentley & Naggar, 2000). The Mohr-Coulomb model suggests that the yielding begins when the shear stress τ and normal stress σ_n satisfy Equation 4.2 was used in this study.

$$\tau = c + \sigma_n \tan \emptyset \qquad 4.2$$

In Equation 4.2, c is the cohesion and $\emptyset$ is the friction angle of the soil. The yield criterion of the Mohr-Coulomb model is defined by Equation 4.3 as:

$$f = (\sigma_1 - \sigma_3) - (\sigma_1 + \sigma_3) \sin \emptyset - 2c \cos \emptyset = 0 \qquad 4.3$$

Where σ_1 and σ_3 are maximum and minimum principal stresses.

In section 2.6.7, this material model is discussed in detail.

4.6 Soil-Pile Interface

In finite element analysis, relative movement of a pile element with respect to the adjacent soil element at the soil-pile interface is prohibited. There are two mechanical contacts on ABAQUS between two surfaces (bodies): the node based interaction and surface based interaction. In node based interaction, mechanical contact between two nodes is modeled using contact elements, whereas in surface based interaction surfaces directly interact with each other. Surface based interaction has the advantage over node based interaction because of its capability to model both normal and tangential interaction behavior whereas node based interaction facilitates only the normal interaction behavior.

There are two contact areas for the soil and the pile. They are the circumferential boundary of the pile in contact with the surrounding soil and the bottom boundary of the pile in contact with the soil below the pile.

The circumferential boundary is modeled by defining the surface to surface contact between the pile and the surrounding soil. The two surfaces are to be defined based on their rigidities. The more deformable surface is defined as a slave surface while the one with the greater rigidity is defined as the master surface. Master and slave surfaces for this study are surfaces of the pile and the soil respectively. Pile-soil interaction is defined by tangential and normal contact behavior.

For the normal behavior, it was decided to use a “hard” contact together with the penalty constraint enforcement method. This approach allows any pressure to be transmitted between surfaces if they are in contact (Figure 4.4). If the contact surface is separate the contact pressure reduces to zero. Separated surfaces come into contact when the clearance between them reduces to zero.

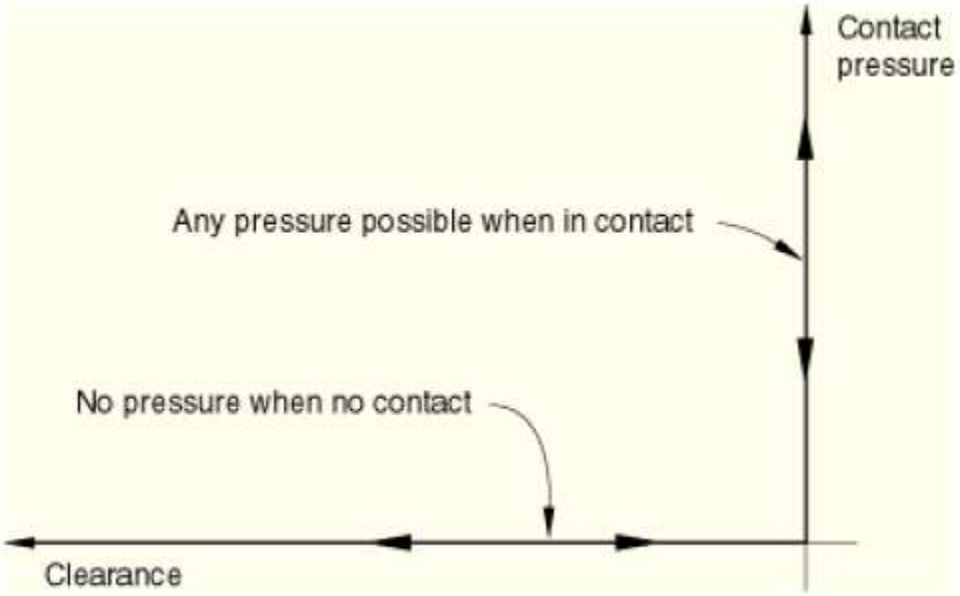

Figure 4.4: Hard contact behavior (ABAQUS Documentation, 2010)

Regarding the tangential behavior, the shear behavior between two surfaces is defined by the Coulomb frictional law (Figure 4.5). The Coulomb friction model states that two contacting surfaces can carry shear stresses up to a certain magnitude across their interface before they start sliding relative to one another. The Coulomb friction model defines this critical shear stress, τ_{crit}, at which sliding of the surfaces starts as a fraction of the contact pressure, P , between the surface, as given in Equation 4.4.

$$\tau_{crit} = \mu\, p \qquad 4.4$$

Where τ_{crit} the critical shear stress at contact surface is, μ is the coefficient of friction and, p is the contact pressure between two surfaces. ABAQUS requires a coefficient of friction between the surfaces in contact but this is unknown. The directionality of the friction was assumed to be isotropic and a value of μ = 0.5 was used. All other settings for the tangential behavior were set to default.

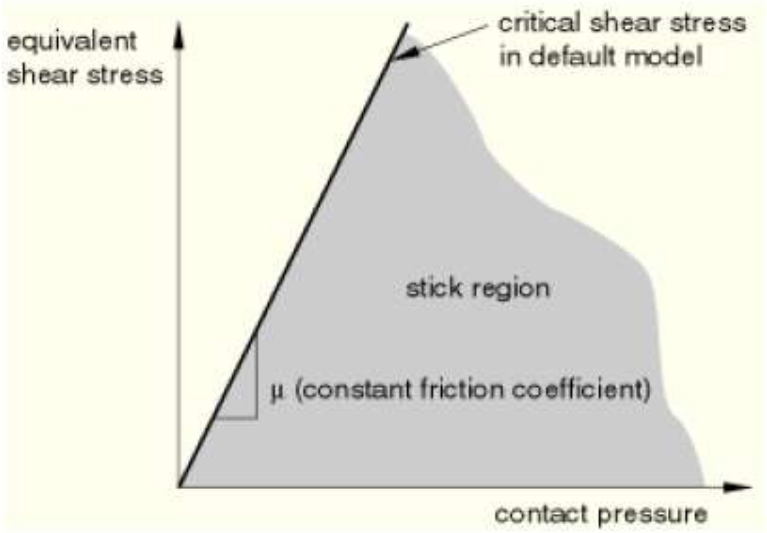

Figure 4.5: Slip regions for the basic Coulomb friction model (ABAQUS Documentation, 2010)

The bottom boundary contact is between the bottom part of the pile and underlying soil. This contact is modeled by tie constraints. Tie constraint is used to make the translational and rotational motion equal for a pair of surfaces. In this contact bottom part of the pile is the master surface and the soil is the slave surface.

4.7 Numerical Accuracy and Stability

As discussed in section 2.6.4 the numerical simulation of dynamic SSI is controlled by two main parameters. There are the spacing of the nodes and the length of the time step. Assuming that the numerical method converges toward the exact solution as Δt and Δh go toward zero the desired accuracy of the solution can be obtained as long as sufficient computational resources are available. In order to represent a traveling wave of a given frequency accurately about 10 nodes per wavelength are required. Fewer than 10 nodes can lead to numerical damping as the discretization errors certain peaks of the wave (Jeremic & Preisig, 2005). The value of the highest relevant frequency is 8.5 from Fourier amplitude analysis of input motion but to determine the appropriate maximum grid spacing (Jeremic & Preisig, 2005) recommended f_{max} is about 10 Hz for seismic analysxis. In this thesis 8.5 Hz is the maximum relevant frequency and it is on acceptable range seismic analysis is shown Figure 4.6.

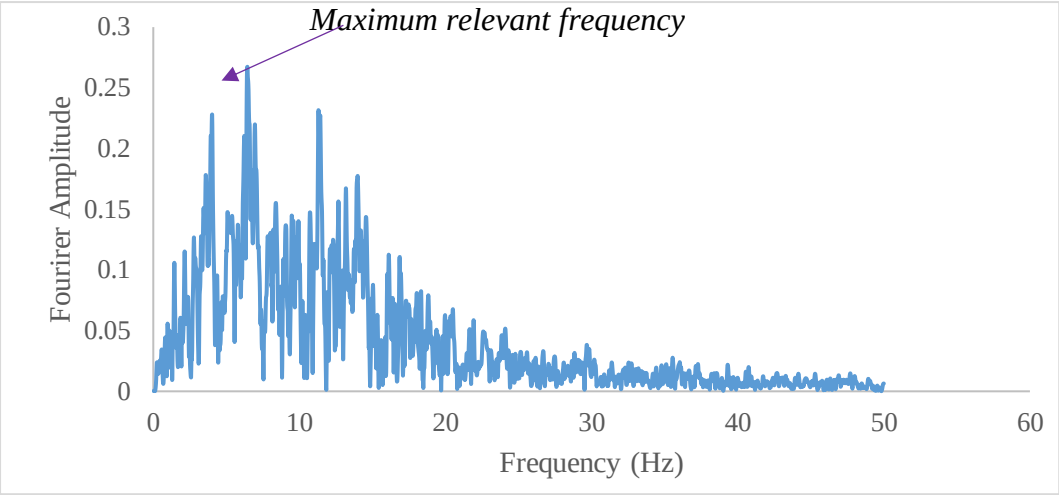

Figure 4.6: Fourier Transformations of the Earthquakes

In this study, shear wave velocity is chosen from geotechnical report seismic surface wave (ReMi, one of the seismic equipment) conducted for the project. Seismic equipment records data depending on the material properties of the subsurface. The investigation on the above mentioned report determines shear wave velocities down to a minimum of 5 meters and a maximum of 40 meters depth shown in Figure 4.7.

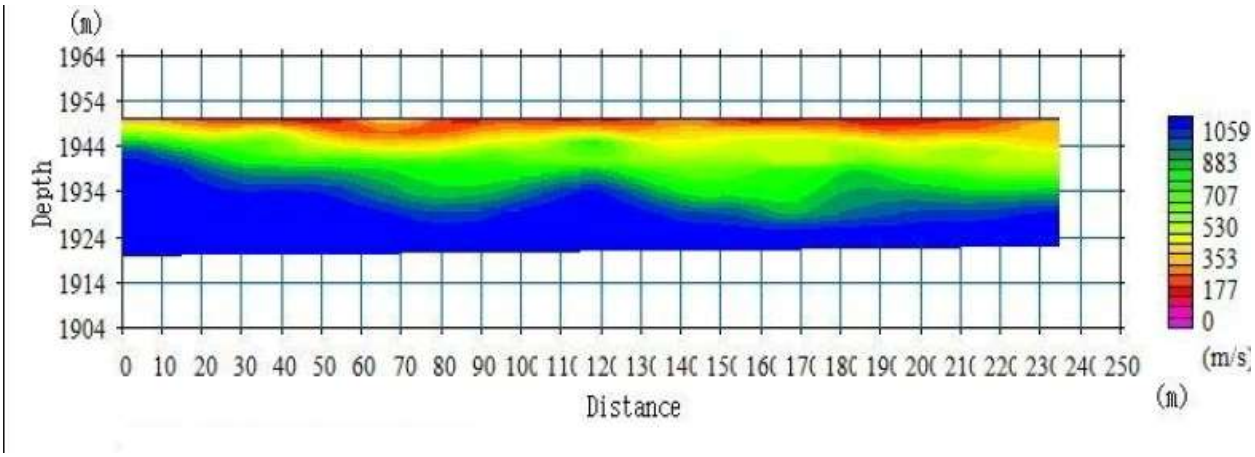

Figure 4.7: Shear wave with depth

Layer -1

Therefore, $\Delta h \leq \frac{v}{10\ f_{max}} = \frac{110}{10*8.5}$ =1.29 m

Layer -2

Therefore, $\Delta h \leq \frac{v}{10\ f_{max}} = \frac{177}{10*8.5}$ =2 m

For nonlinear numerical model of wave propagation problems the time step Δt has to be limited for two reasons they are accuracy and stability for all modes. If the time step in the finite element analysis is too large the wave front can reach two consecutive elements at the same moment. This would violate a fundamental property of wave propagation and can lead to instability. The time step, therefore, needs to be limited. In this model, the smallest grid space Δh= 1.29 m and the maximum time step is estimated as:

$$\Delta t = \frac{\Delta h}{v_{max}} = \frac{1.29}{110} = 0.012\ s$$

4.8 Mesh

The dynamic loading of a single pile is simulated for the analysis of pile and wave propagation in soils using the finite element method. The pile was considered as a cylindrical solid element for the purpose of determining the pile mesh size. It has been subjected to a lateral earthquake load applied at the base of the model. The pile is considered to be fully embedded in soil.

The element sizes are chosen very carefully, on seismic analysis, choosing the right element size for the finite elements is essential to capture the motion of waves accurately. The maximum element size for soil was maintained at a value less than one-fifth to one-eighth the shortest wavelength (λ_s) to acquire the required accuracy. Here, V_s/f in which V_s is the shear wave velocity and f is excitation frequency.

Layer -1

The shear wave velocity is 110 m/s

$$\lambda = \frac{v}{f} = \frac{110}{45} = 2.44$$

$$minimum\ \ element\ size\ = 0.31$$

$$maximum\ element\ size\ = 0.48$$

Layer -2

The shear wave velocity is 117 m/s

$$\lambda = \frac{v}{f} = \frac{177}{45} = 3.93$$

$$minimum\ \ element\ size\ = 0.49$$

$$maximum\ element\ size\ = 0.78$$

In finite element modeling, minimum mesh sizes that give accurate results and remove excessive calculation time and high computer memory requirements should be calculated. Accordingly, the mesh sizes of the finite element calculation result in a size of 0.4 m.

4.9 Loading Steps

4.9.1 Initial

The state of stress in the pile-soil system in actual in-situ conditions was simulated as an initial loading condition (in-situ stress conditions) before any dynamic or static external load. Geostatic stress was modeled by applying a gravitational load.

To avoid excessive settlements when applying gravity loads define the stress field of the soil mesh. In ABAQUS the Geostatic step applies to approve the in-situ condition. In defining the stress field, vertical stress at two points should be defined and the variation between those two points is considered linear. Here, vertical stress at a point
(σ_v) , is determined by considering the number of soil layers that lie above the point considered (n),

$$\sigma_v = \sum_i^n \gamma_n h_n \qquad 4.5$$

Where, γ_n = unit weight of the nth soil layer
h_n = soil layer thickness of the nth layer with respect to the point considered

After defining the vertical stress distribution, the lateral earth pressure coefficient should be defined to calculate the horizontal stress (σ_h) distribution of the soil as follows.

$$\sigma_h = k_o \sigma_v \qquad 4.6$$

Where, k_o is defined as the lateral earth pressure coefficient at rest and calculated using the following equation and the internal friction angle of soil

$$k_o = 1 - sin\,\emptyset \qquad 4.7$$

At initial step of the model, define the geometry and properties of the soil, to define boundary conditions and the interaction between the soil and the pile at the beginning.

4.9.2 Dynamic Loading

In a seismic analysis, seismic load can be applied either as a displacement, velocity, or acceleration time history at the base of the model. The proposed design earthquake for 475 year return period and 2475 years horizontal component of seismic acceleration time history corresponding to 475 years return period for Wolaita Sodo site is shown in Figure 4.8.

Dynamic loading step is applied after geostatic load step. Seismic load is applied at the base of the soil-pile system model as acceleration time history after the selection and scaling of the designed time history. The seismic load is applied in both horizontal and vertical directions for electric tower supported foundation due to the lightweight of the superstructure. The amplitude of the vertical component is assumed to be 2/3 of the horizontal component (Feng, et al., 2011).

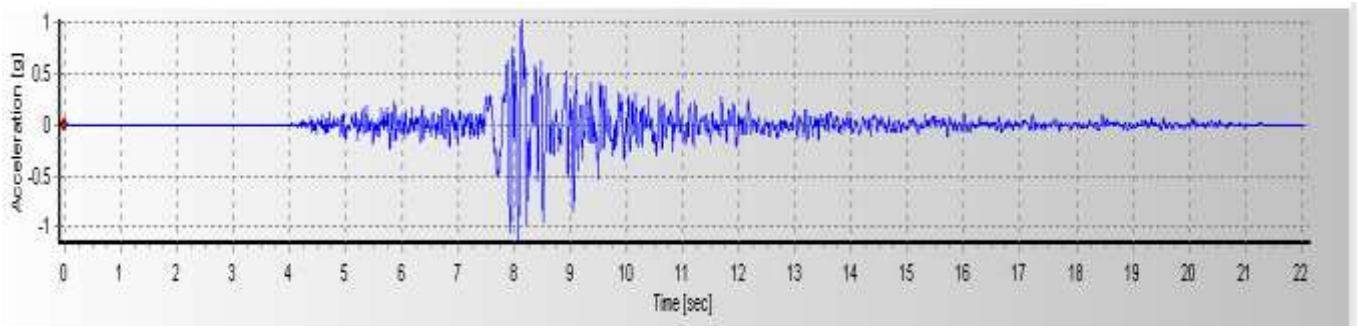

Figure 4.8: Acceleration time history

4.10 Damping

In dynamic analysis of soil-pile interaction system damping occurs in both pile foundation and soil. Damping in pile is negligible as compared to soil damping (Bentley & Naggar, 2000). In this thesis also only the damping occurrence of soil is assumed, neglect the damping in pile foundation.

In soil dynamics, damping is satisfied in two scenarios namely; geometric damping and material damping. See the detail of damping in section 2.6.5

Material damping in soils is considered to be succeeded mainly through viscous damping. Therefore, traditionally, when computing material damping in soils, mass proportional damping is neglected and damping of the soil is achieved through stiffness proportional material damping. Damping matrix is hence reduced to a single matrix, which is proportional to the stiffness matrix as shown in Equation 4.8.

$$[C] = \beta[K] \qquad 4.8$$

In which damping coefficient $\beta = \frac{2\zeta}{\omega_0}$

Where, ω_0 is the predominant circular frequency of loading ζ is the material damping ratio of soil assumed to be 5 % (Bentley & Naggar, 2000). Predominant frequency is obtained from a Fourier spectrum drawn for the input wave from the analyzed time history as shown in Figure 4.9. The frequency that gives the maximum Fourier amplitude is selected as the predominant frequency.

$$\beta = \frac{2 * 5\%}{8.5} = 0.012$$

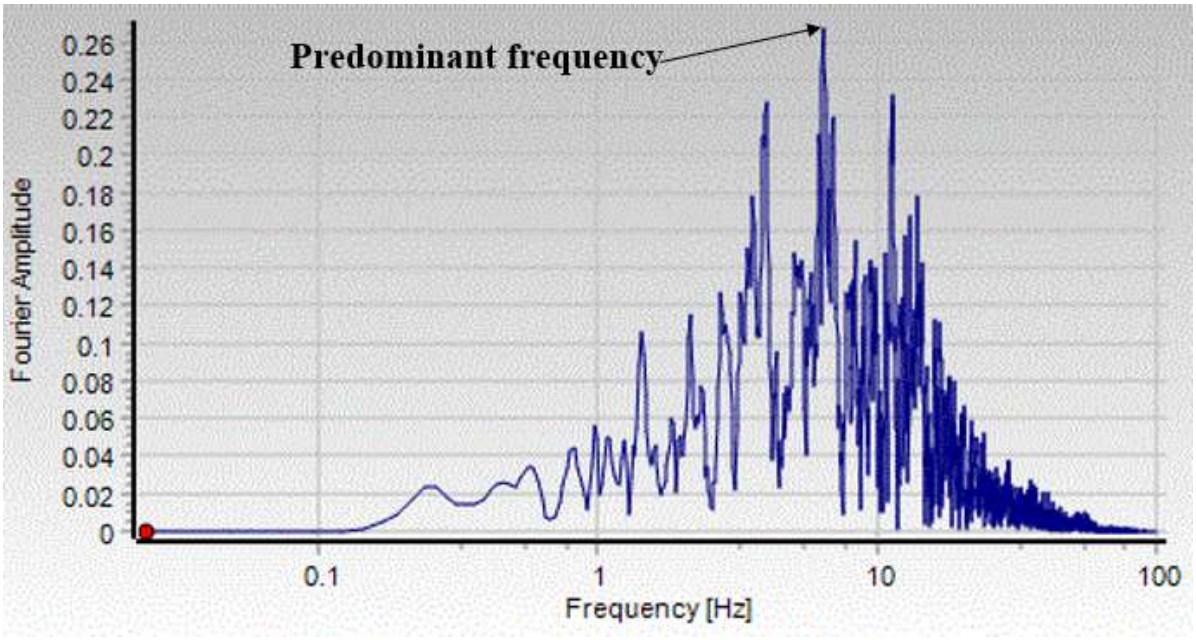

Figure 4.9: A typical Fourier transformations graph to find the predominant frequency of an earthquake wave

4.11 Boundary Condition

The important aspects of boundary conditions on dynamic analysis are to avoid wave reflection. The use of FEM for this purpose dictates that infinite medium be reduced along artificial boundaries and thus be reduced to finite region (near field). Artificial boundaries do not transmit waves from near field to far-field without reflections, or at least the wave reflection back into near field should be minimized.

In ABAQUS there are linear infinite elements that can be used to simulate the infinite extent of the soil (ABAQUS Documentation, 2010). In this thesis CIN3D8, a three-dimensional linear brick with 8 nodes element is used. When using infinite elements the region modeled with finite elements is called near-field region and the far-field region consists of infinite elements. The mesh size of the infinite elements must be larger than the finite elements when using infinite element on the model. The nature of infinite elements is such that the displacement tends to zero at the boundary of the far-field region and therefore the size of infinite elements must be large enough for this to be imposed.

The soil was modeled into two regions, near field region and far-field region. The near field region discuss in detail on section 4.4. The far-field element is modeled as an infinite element but the infinite element is not available in element definition on ABAQUS, due to this first define the far-field region by a three–dimensional acoustic elements with 8 node linear brick elements is defined AC3D8 element type. After meshing define the job right click on defined job select write input goes “inp” file replace AC3D8 element with CIN3D8 element. The boundary applied as the extent of the near-field zone was determined as 10D from the pile center where D is the pile diameter.

The advantage of using a combination with finite and infinite elements instead of only finite elements is that the geometry of the soil could be smaller while still preventing the soil boundaries to affect the pile soil response. Another benefit is that infinite element boundaries serve as the boundary conditions, and no external boundary conditions need to be specified, as stated in (ABAQUS Documentation, 2010). The boundary condition for an infinite element is that the displacement will decrease linearly within the element, to zero just at the infinite boundary.

Regarding the combination of finite and infinite elements, the near-field region is modeled with C3D8I elements whereas CIN3D8 is the element type in the far-field region, Figure 4.10. In the far-field region, one infinite element in the radial direction was used. The lower region of the soil is also modeled with infinite elements and an element length of 3 meters was assumed. The mesh setup for the combination of finite and infinite elements is shown in Figure 4.11.

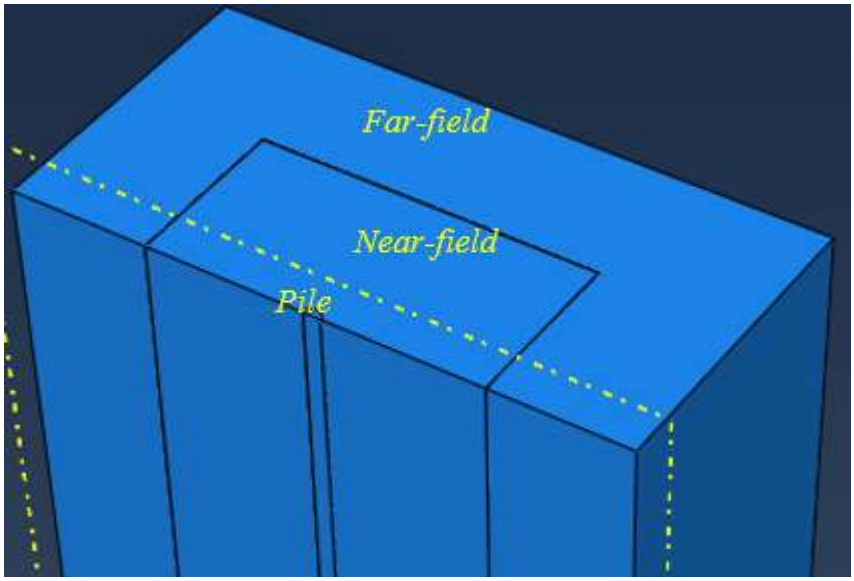

Figure 4.10: Definition of near-field and far-field region

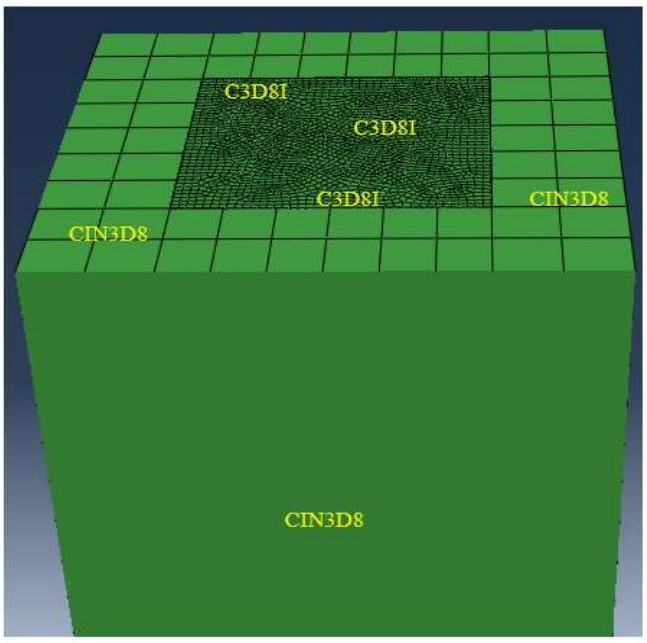

Figure 4.11: Mesh setup for a combination of finite and infinite elements

Figure 4.12 show section view of detail the model half three-dimensional representations of model size and element type

Detail pile element types

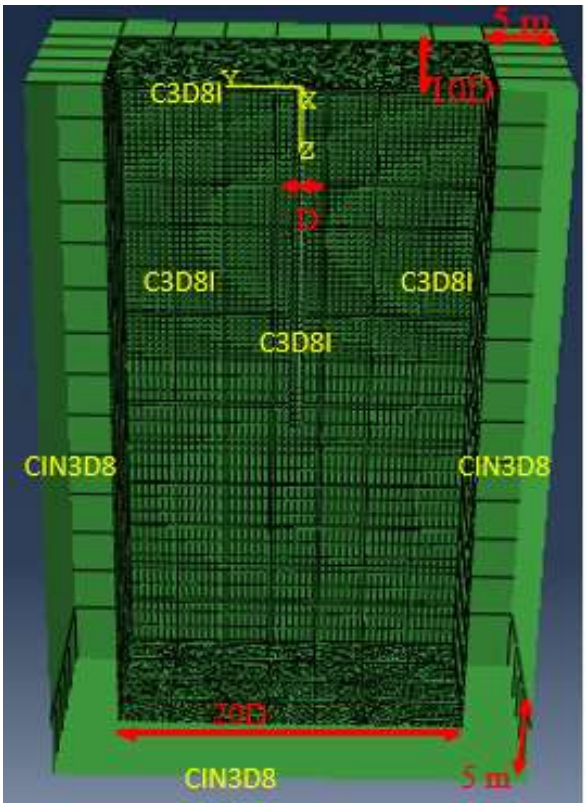

Figure 4.12: Three-dimensional representations of model size and element type

CHAPTER 5 RESULTS AND DISCUSSION

5.1 Ground Motion Analysis

Peak amplitude, representing the peak ground acceleration (PGA), is an important design parameter. The probabilistic seismic hazard analysis (PSHA) result in a horizontal PGA value of 0.13g and 0.223g for design basis earthquake and maximum considered earthquake respectively. The PGA value of the design basis earthquake is within the range of recommendations stated on the seismic hazard map of Ethiopia return periods of 475 years by (Worku, 2011). Worku prepared new seismic hazard map for Ethiopia which has five distinct zones with different values of PGA as shown in Figure 5.1. Wolaita Sodo converter station is located on Worku's seismic hazard map with PGA value ranging from 0.1g to 0.16g.

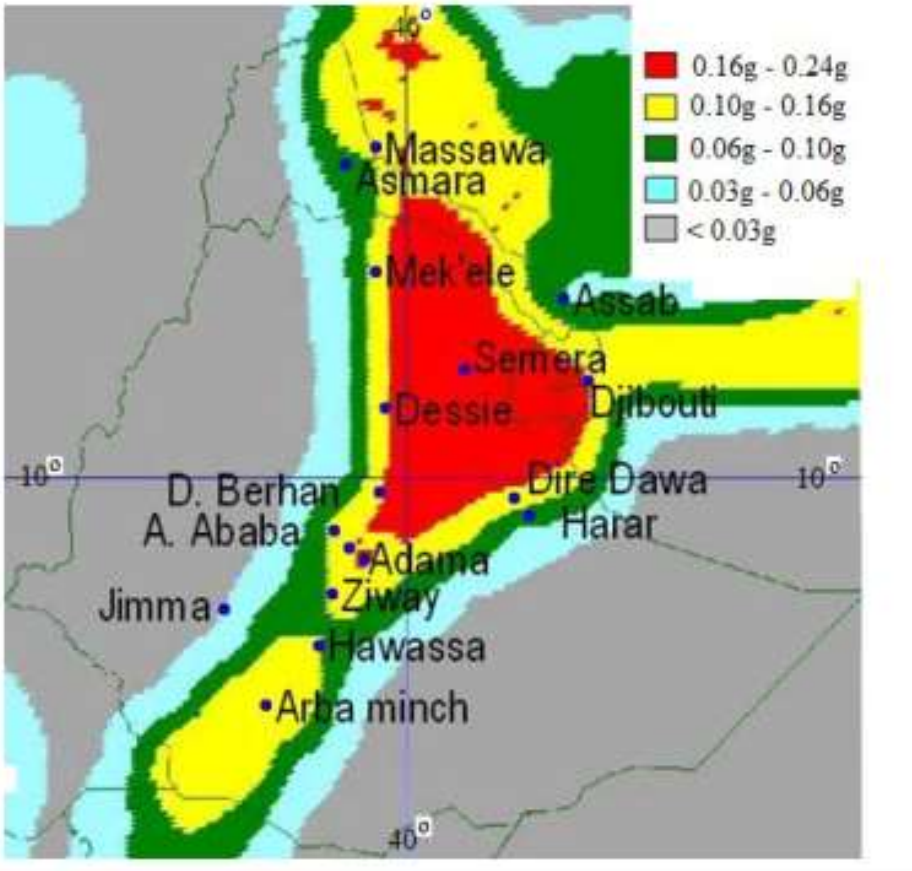

Figure 5.1: The seismic hazard map of Ethiopia based on the GSHAP data for a return period of 475 years (Worku, 2011)

Using the above PGA values, deaggregation result in the most dominant magnitude of earthquake to be 5.5 and 5.7 and source to site distance of 20.23km and 15.27km, respectively. PEER ground motion database has been searched for an earthquake magnitude ranging from 5.5-5.7 and distance range of 15-30km. Top 30m shear wave velocity of 557m/s has been used from the geotechnical report as an input on PEER ground motion database. The fault type was selected to be normal fault as it is the dominant fault type for Ethiopia.

Umbria Marche earthquake has been selected from the database using the above mentioned inputs to characterize the area. The PGA value of this earthquake is 0.163g which arises the need for scaling. After scaling, the acceleration time history that is going to be applied on the base of the model is shown in Figure 5.2.

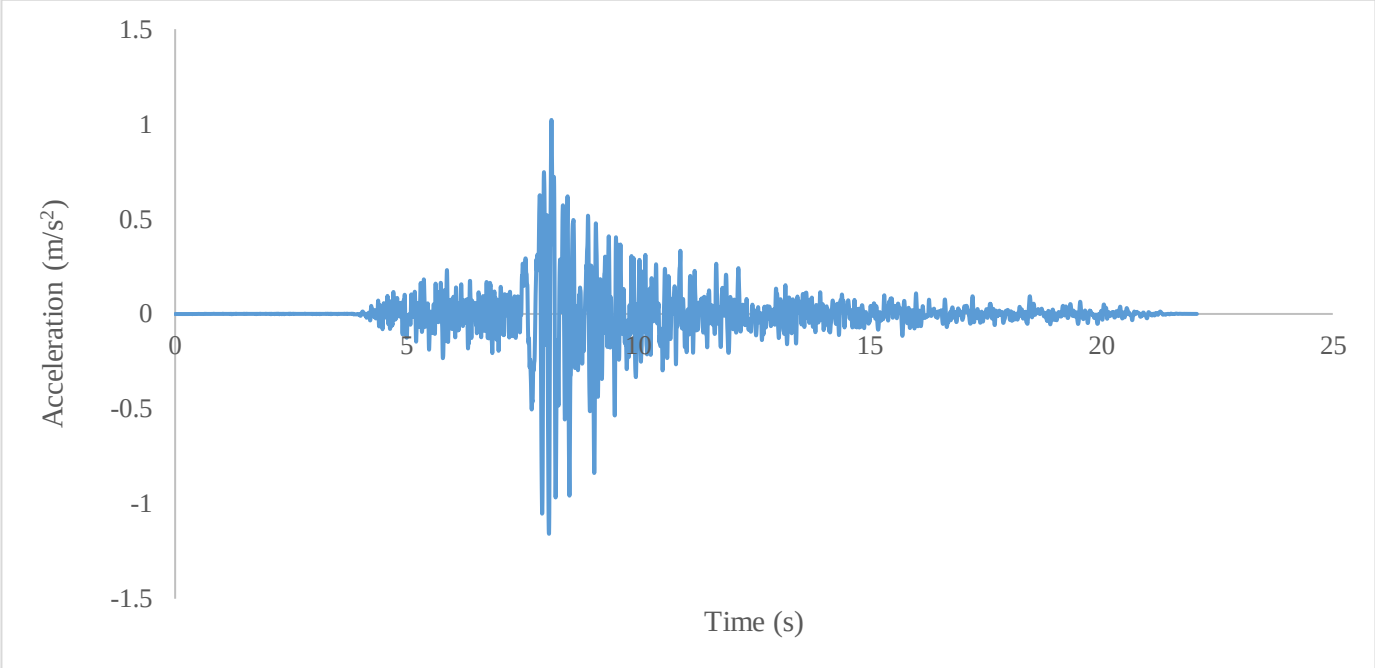

Figure 5.2: Scaled Earthquake

5.2 Pile Head Response

Figure 5.3 and Figure 5.4 show pile head responses of displacement and acceleration with dynamic time for 0.6 m diameter pile, respectively, subjected to seismic excitations at the base of the model.

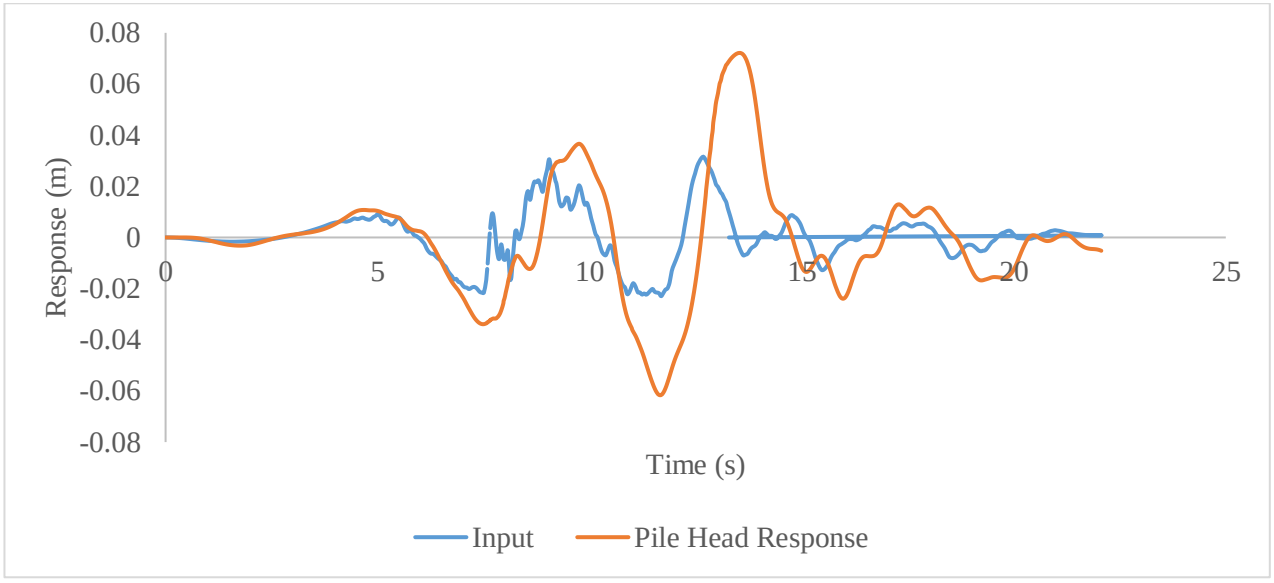

Figure 5.3: Lateral displacement of diameter 0.6 m at pile head with dynamic time under kinematic interaction

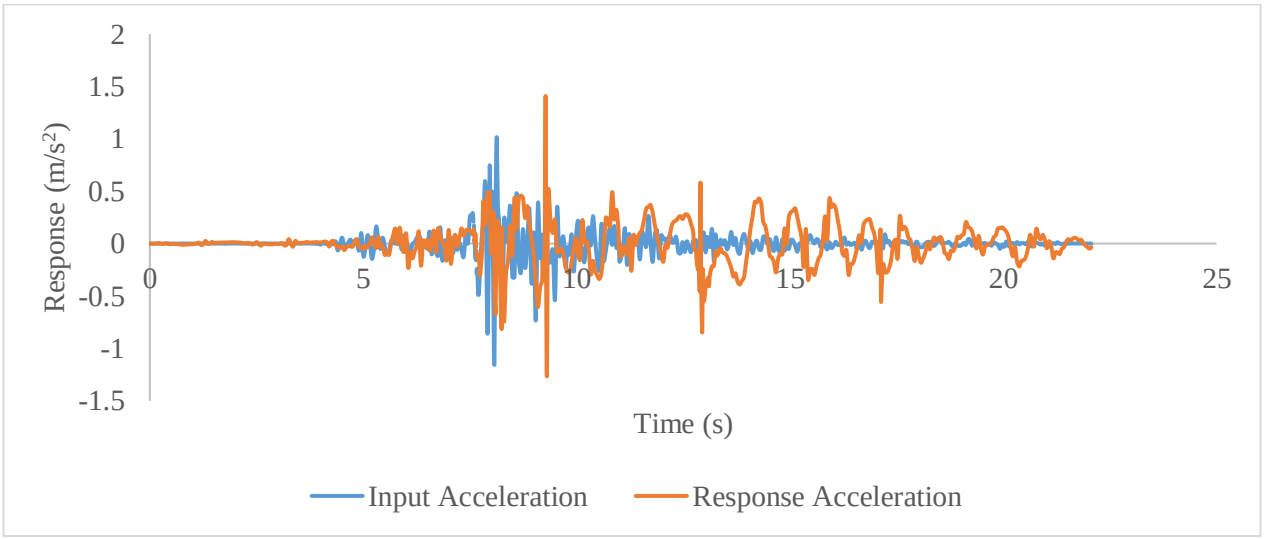

Figure 5.4: Acceleration response of diameter 0.6 m at pile head with dynamic time under kinematic interaction

Figure 5.5 and Figure 5.6 show pile head responses of displacement and acceleration with dynamic time for 0.8 m diameter pile, respectively, subjected to seismic excitations at the base of the model.

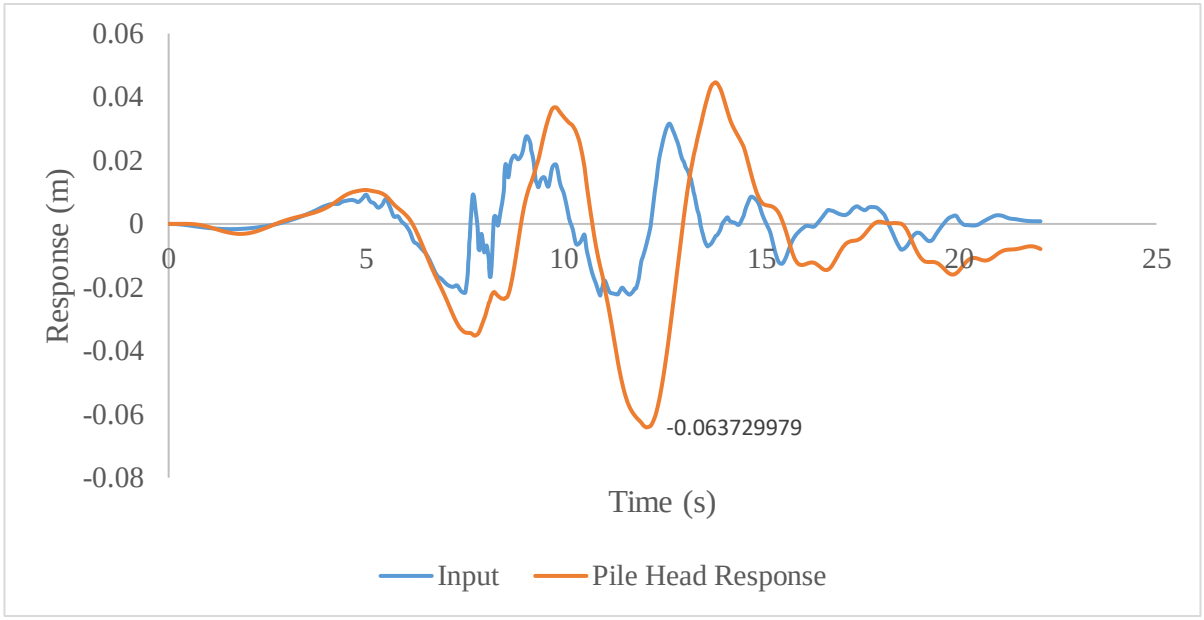

Figure 5.5: Lateral displacement of diameter 0.8 m at pile head with dynamic time under kinematic interaction

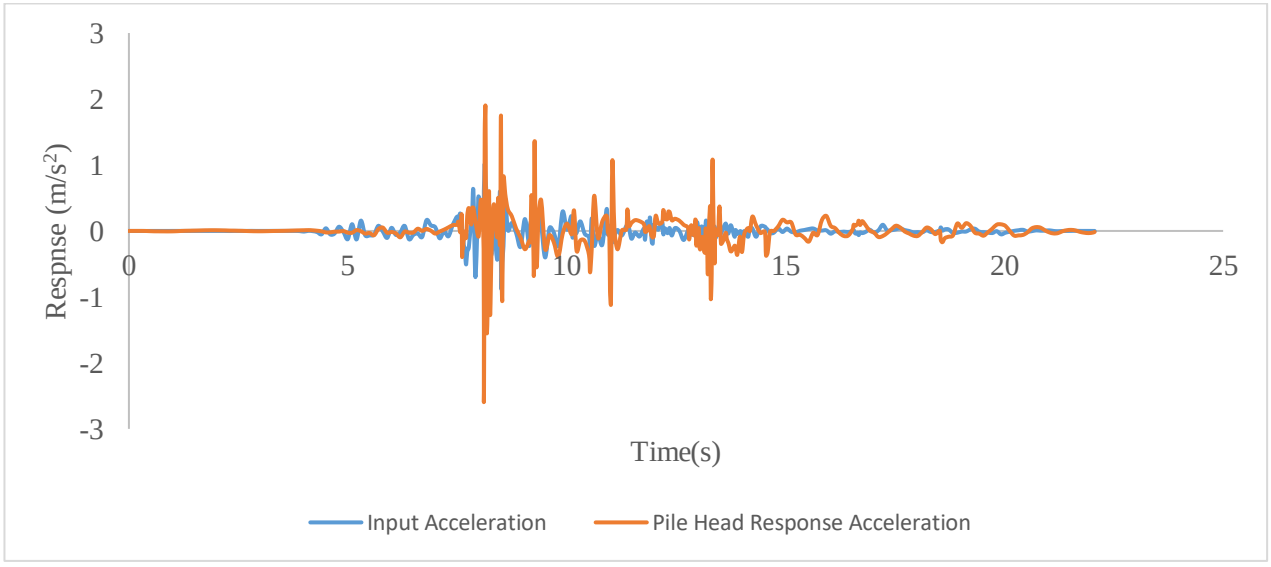

Figure 5.6: Acceleration response of diameter 0.8 m at pile head with dynamic time under kinematic interaction

As shown in Figures 5.3-5.6, the responses show similar pattern as that of the input. It is shown that the input motions were amplified on the response diagrams, both for the acceleration and displacement. The maximum lateral deflections of the piles are 72.02 mm and 63.7 mm for 0.6 m and 0.8 m diameter piles, respectively. Bouzid et.al. 2013 cited in API (2001) state allowable head deflection to be up to 5% of the pile diameter. Accordingly, the obtained pile deflections in this thesis exceed the acceptable range, the thresholds being 30 and 40 mm for diameter 0.6 m and 0.8 m respectively. While modeling the pile, stiffness of plain concrete has been considered and the stiffness contribution of reinforcements has not been incorporated. The above exceedence of deflection thresholds might be attributed to this effect.

To determine the effect of pile size on pile head response, two pile diameters, 0.6 m and 0.8 m, have been considered while keeping pile properties, pile element, mesh sizes, and pile length constant. Comparison of the displacement of the two piles shows reduction of pile displacement with the increase of pile diameter. As shown in Figure 5.5, the displacement of the 0.8 m diameter pile is lower than the displacement of 0.6 m diameter pile throughout the dynamic time.

5.3 Embedment Depth Effect

Figure 5.7 and Figure 5.8 shows the kinematic pile response at different embedment depth from the top head of the pile to the bottom of pile with interval of 3 m. The lateral displacement of the pile shows decrement with the increase of embedment depth. This is attributed for the increase of stiffness of soil as depth increases.

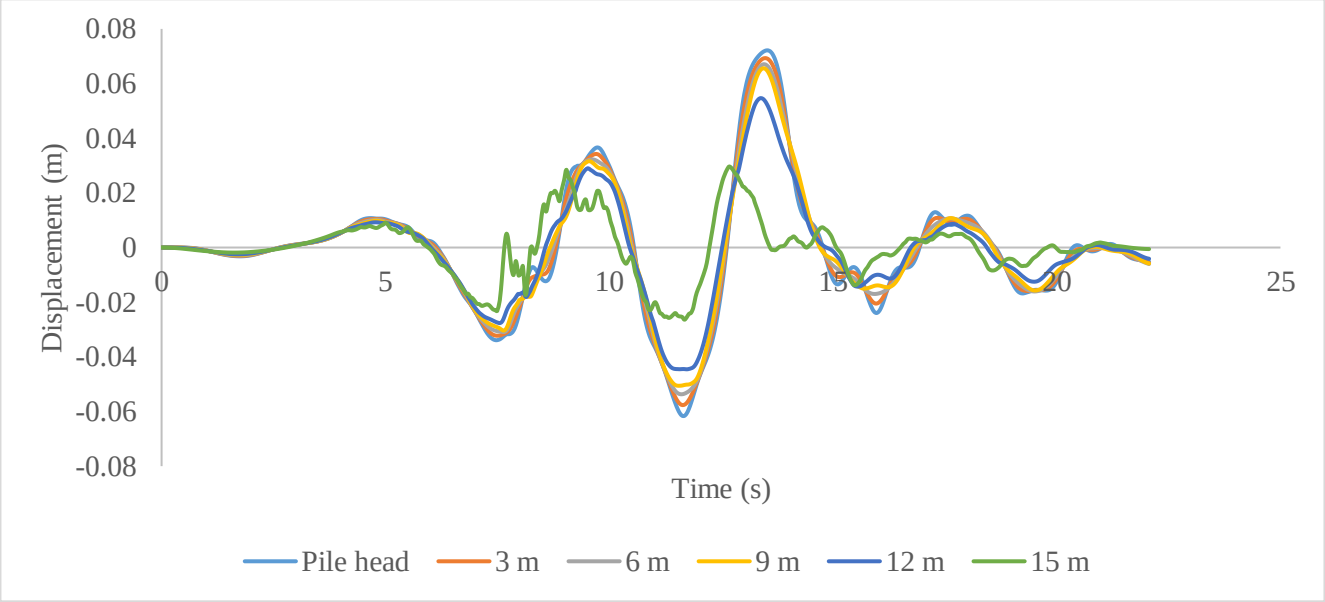

Figure 5.7: *Lateral displacement of 0.6 m pile for different depths under kinematics interaction*

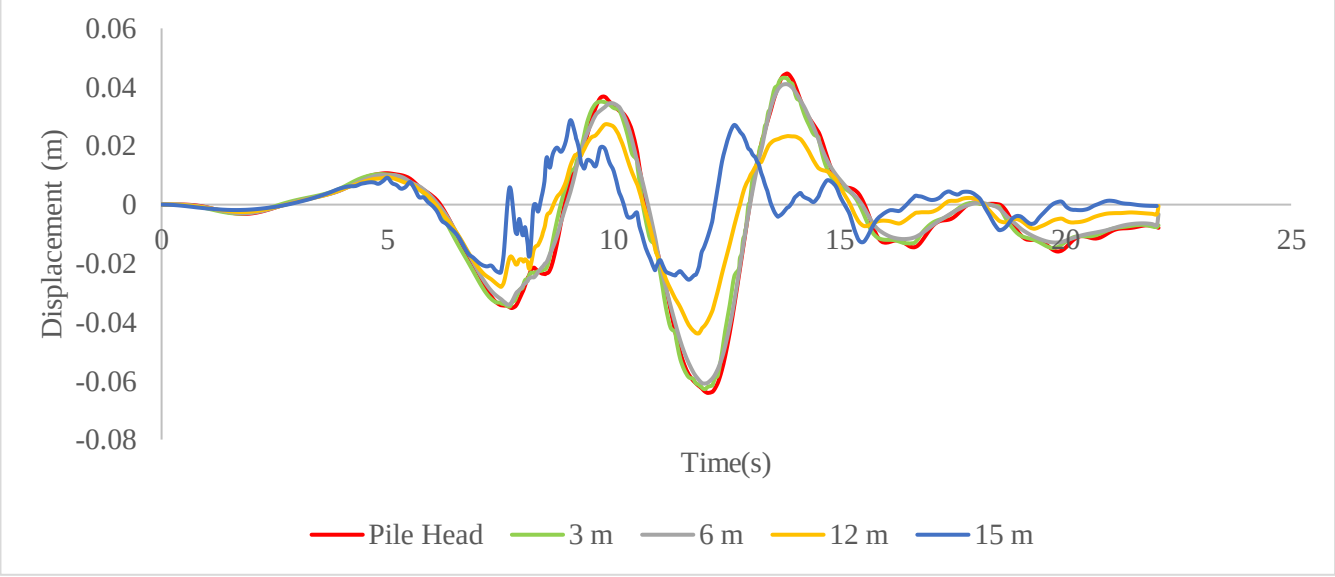

Figure 5.8: *Lateral displacement of 0.8 m pile for different depths under kinematics interaction*

Figure 5.9 shows the pile deflection along the length of pile for diameter 0.6 m and 0.8 m respectively. When long slender piles are embedded in layered soil, the deformation along the pile can be governed by the stiffness of the surrounding soil and the amount of deflection can be influenced by the stiffness difference between pile and soil. Lateral deflection of pile decreased while going down along the pile length for both diameter 0.6 m and 0.8 m.

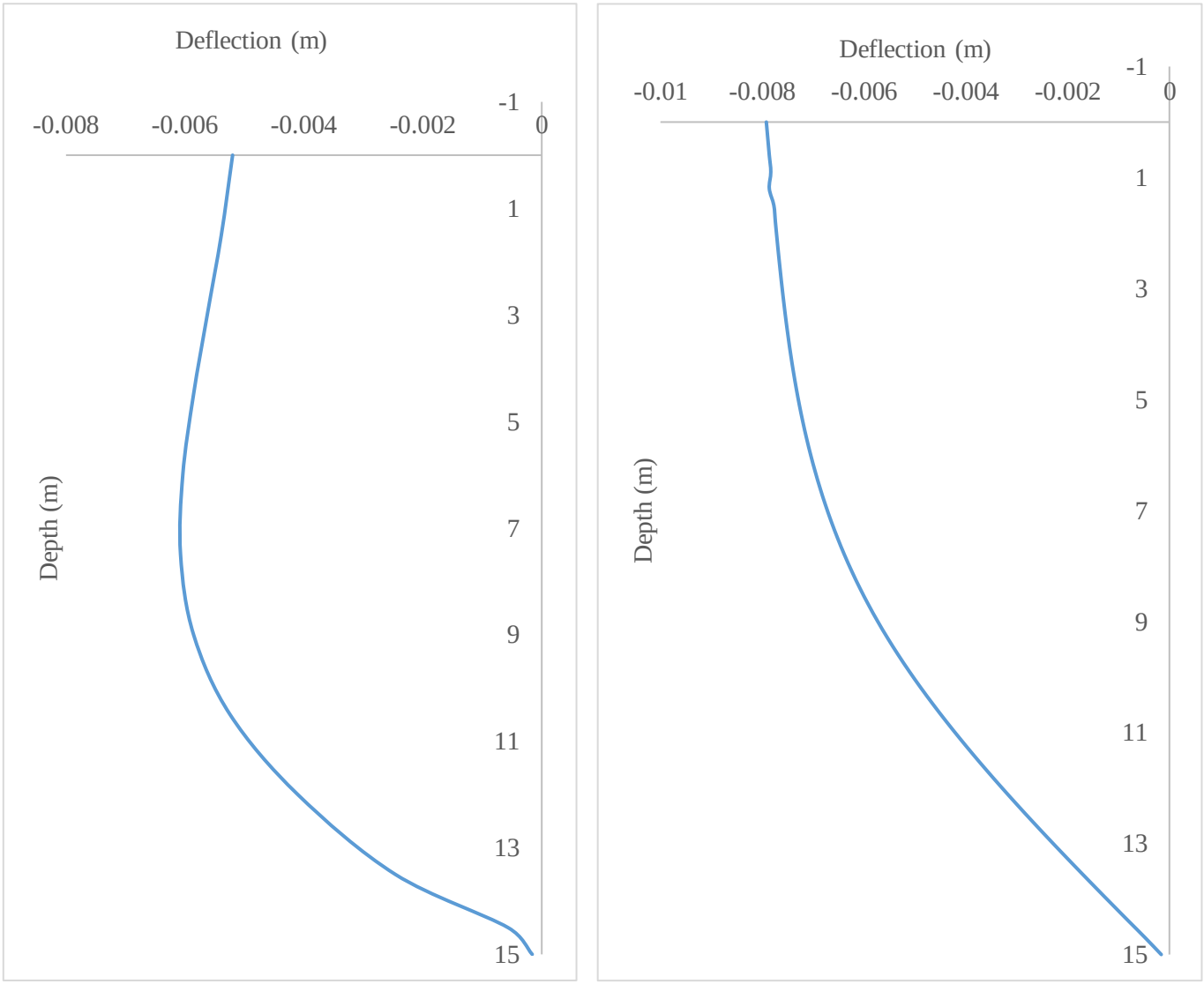

Figure 5.9: Pile deflection along the pile length a) Diameter 0.6 m b) Diameter 0.8 m

The shear force in each horizontal pile section was calculated by multiplying the x-direction horizontal shear stress of each element by its plan surface area using Equation 5.1.

Mathematically,

$$F = \sum_{i=1}^{n} \tau_{xy} A_i \qquad 5.1$$

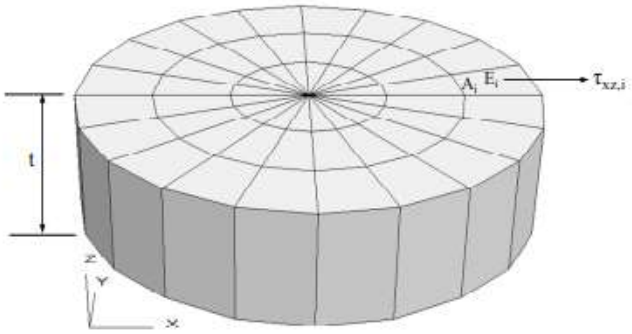

Figure 5.10: A section showing stress in x-direction in an element

Where,

F = shear force in each horizontal pile section

$\tau_{xy,i}$ = horizontal shear stress in element

Ai = plan area of element

N = total number of elements in a horizontal pile section

The bending moment (M) developed in each pile section was obtained by summation of the product of the vertical stress at each element, the plan area of that element, and the x-distance from the center of the pile to the centroid of the element using Equation 5.2 to calculate bending moment.

$$M = \sum_{i=1}^{n} \sigma_{yy,i} * A_i * xc_i \qquad 5.2$$

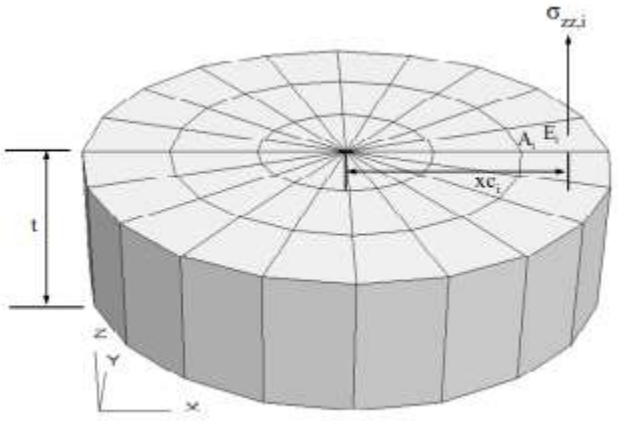

Figure 5.11: A section showing stress in z-direction in an element

Where,

M = bending moment in each horizontal pile section

$\sigma_{yy,i}$= vertical normal stress in the element

A_i = plan area of element Ei

xc_i = centroid distance of element Ei from the center of the pile, in the x-direction

n = total number of elements in a horizontal pile section

Figure 5.12 shows shear force diagram along the pile length for diameter 0.6 m and 0.8 m respectively.

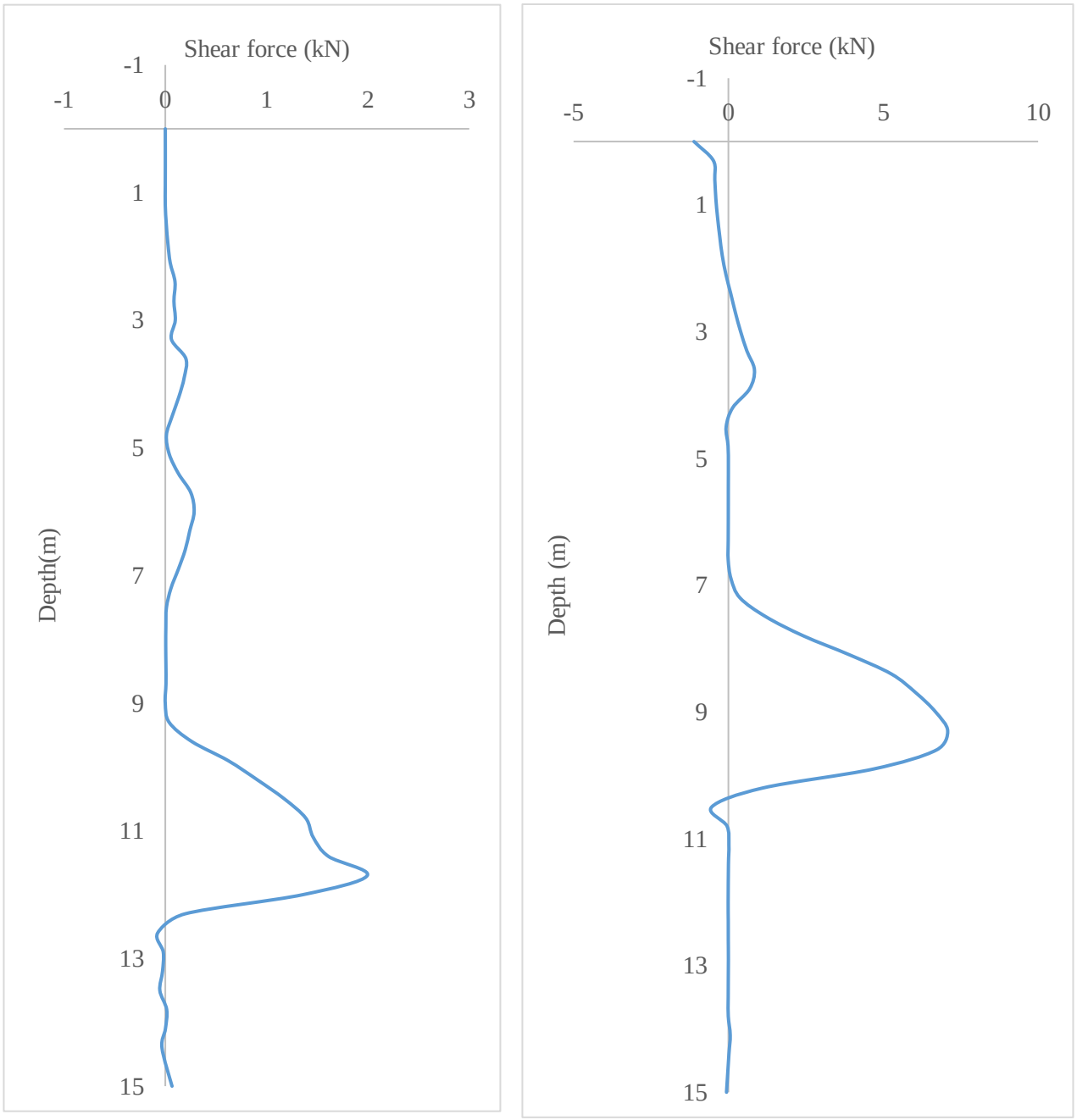

Figure 5.12: Shear force along the pile length a) Diameter 0.6 m b) Diameter 0.8 m

Figure 5.13 shows bending moment diagram along the pile length for diameter 0.6 m and 0.8 m respectively. In this model maximum bending moment is attained at the bottom of pile. The pile diameter affect the amplitude of the bending moments at the bottom of pile. The bending moment increases as the pile diameter increases .The pattern of bending moment under dynamic load for both diameters are the same and this result is similar to literature (Francesca , et al., 2009).

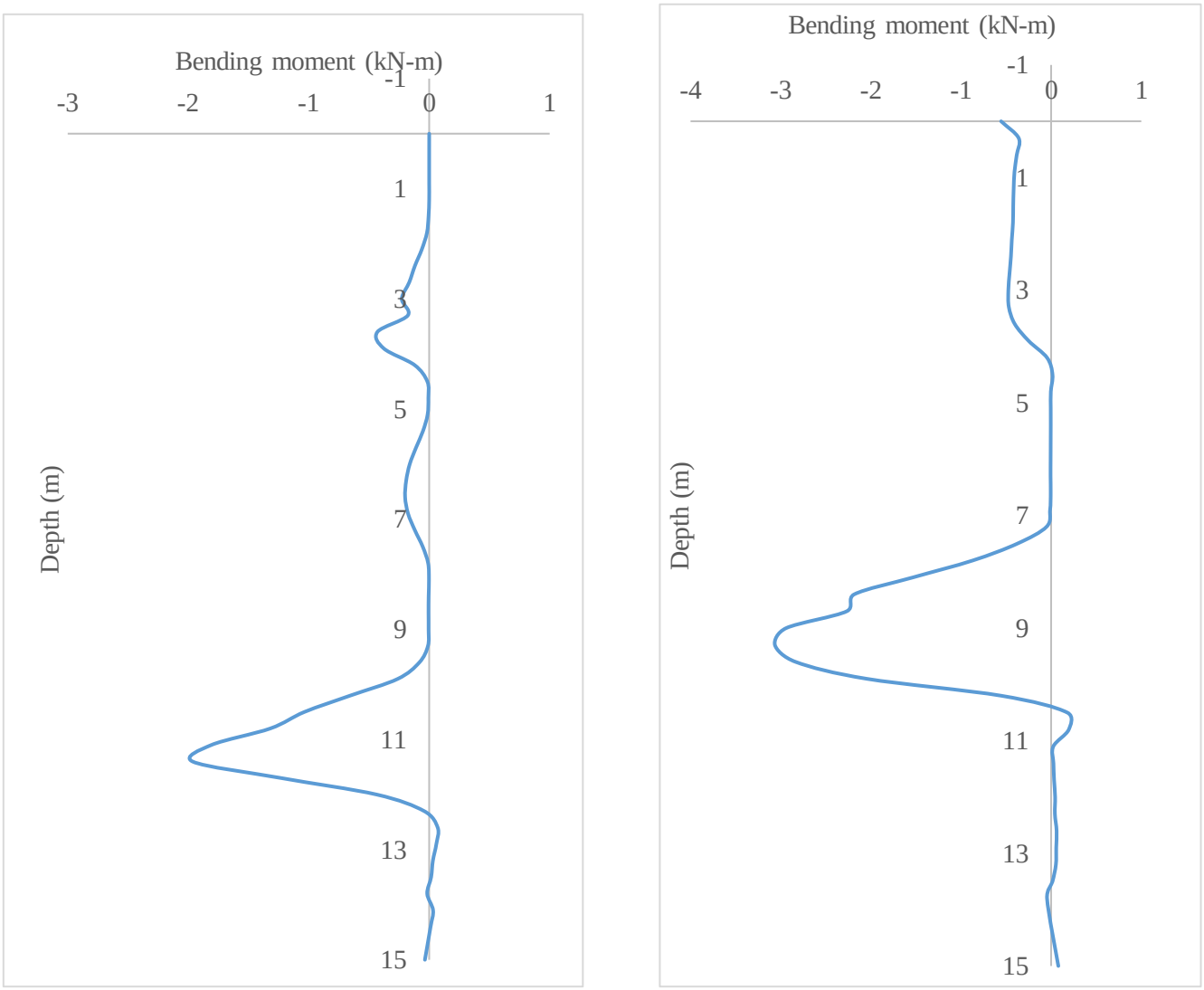

Figure 5.13: Bending moment along the pile length a) Diameter 0.6 m b) Diameter 0.8 m

As the cross section of pile increases the bending moment also increases and depth of soil subjected to bending moment increases with increase in cross sectional area. This is because of increased surface area and Stiffness of the pile.

5.4 Lateral Soil Resistance and Displacement at Different Depth and Diameter

Lateral soil resistance per unit length, p, is the sum of the lateral forces applied to the entire interface nodes per unit length along with the pile. Lateral displacement, y, can be obtained from the nodal displacements. The x-direction (horizontal) components of normal stress ($\sigma_{x,i}$) and shear stress ($\tau_{x,i}$) at interface node,i, were calculated using Equation 5.3 and the lateral soil resistance, p, was calculated by summing all p_i at the desired elevation Kanagasabai (2010).

$$P_{x,i} = \frac{(\sigma_i n_{x,i} + \tau_{xy} n_{y,i}) A_i}{L_i} \qquad 5.3$$

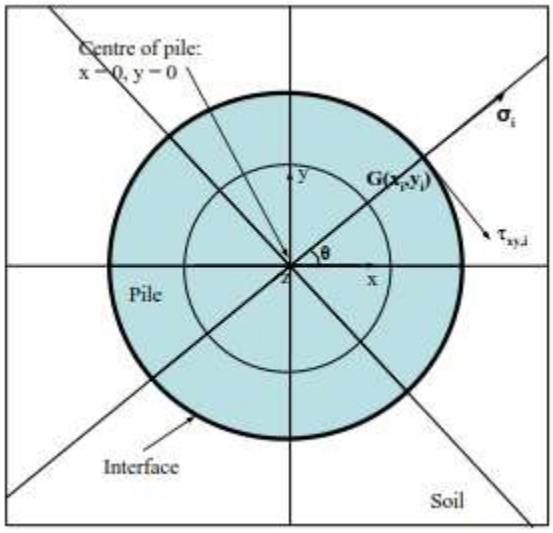

Figure 5.14: Interface between soil and pile system

Where,

σ_i= normal stress at the interface node at point G

$P_{x,i}$= the x- components of lateral soil pressure

$\tau_{xy,i}$= shear stress at the interface node at point G

x_i= x-coordinate of the interface node at point G

y_i= y-coordinate of the interface node at point G

A_i= representative area of interface node

L_i =is the pile length between two neighboring interface nodes along the pi

5.4.1 Displacement and Soil Resistance for Diameter 0.6 m

Figure 5.15 to 5.18 shows displacement and soil resistance with dynamic time for diameter 0.6 m by varying pile depth.

a) b)

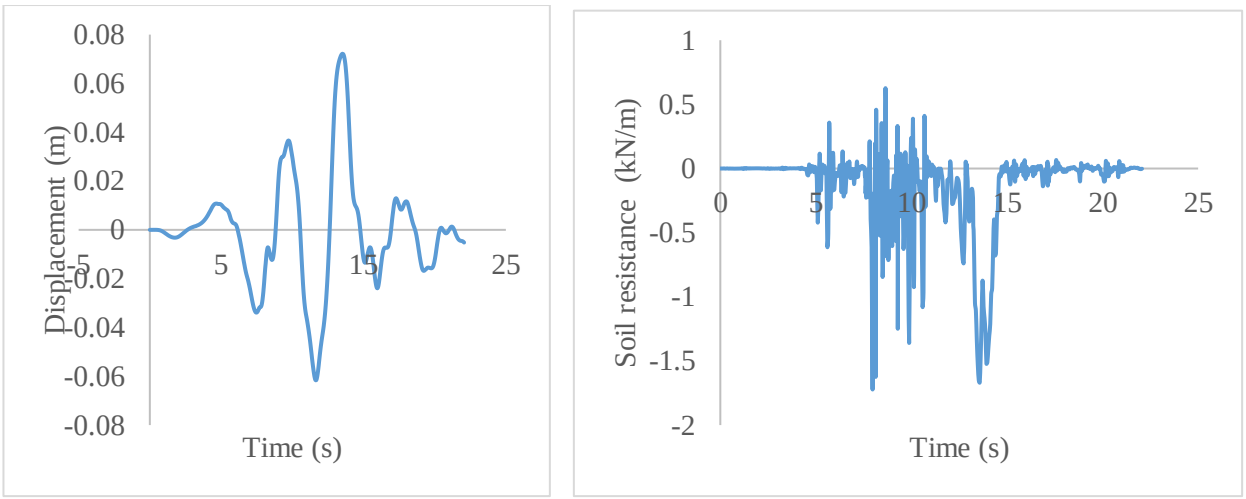

Figure 5.15: Effect of seismic load at pile head a) displacement with time b) soil resistance with time

a) b)

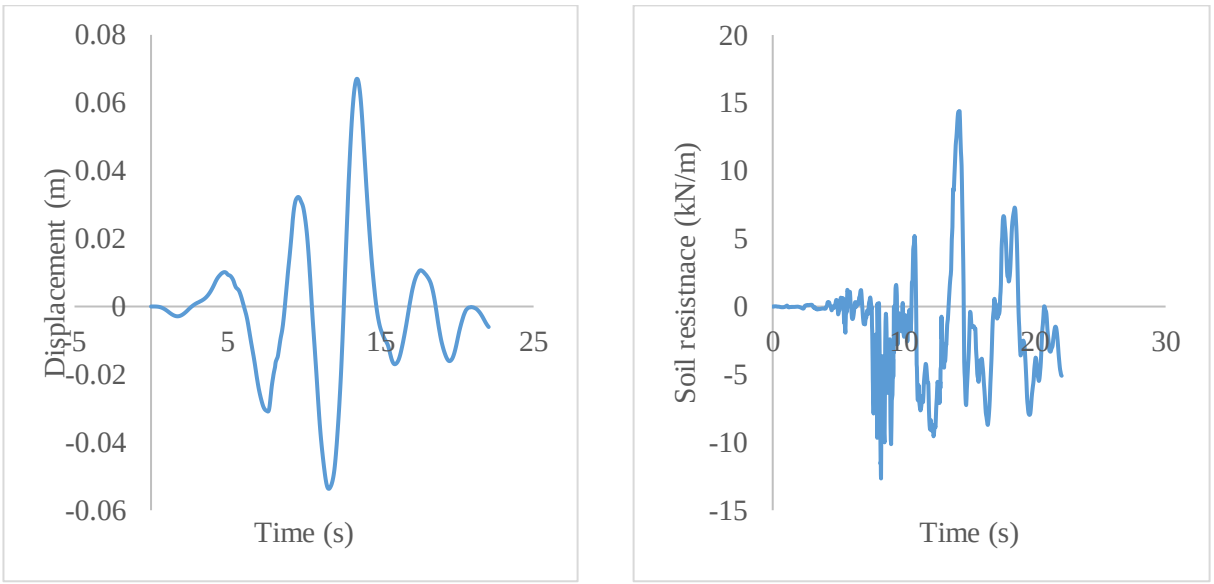

Figure 5.16: Effect of seismic load at depth 6 m a) displacement with time b) soil resistance with time

a) b)

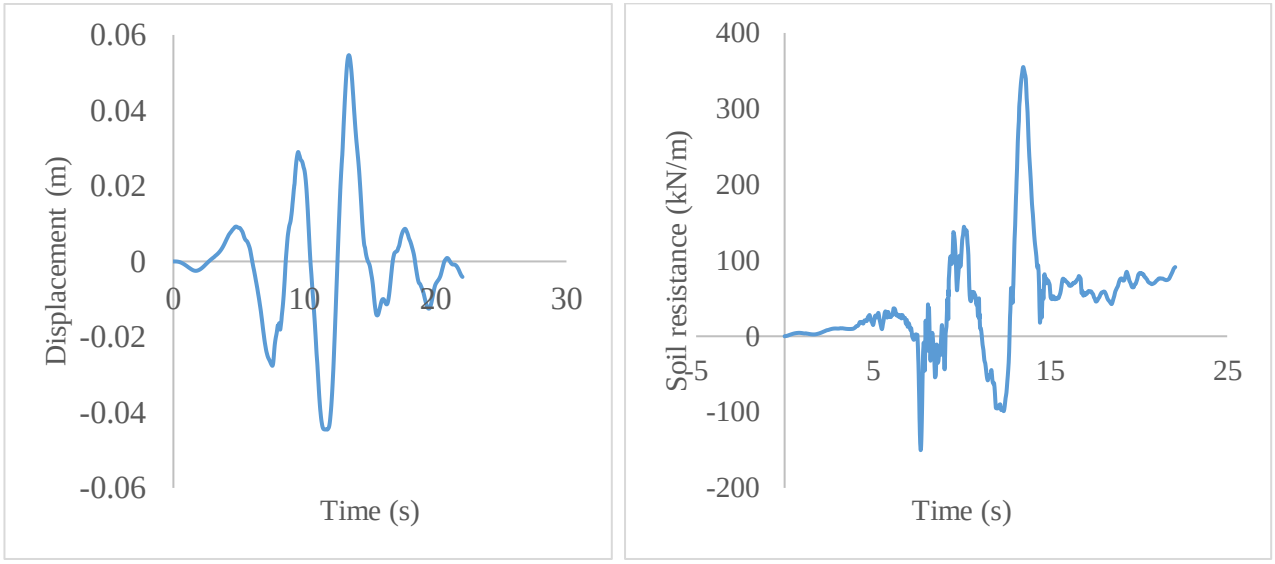

Figure 5.17: Effect of seismic load at depth 12 m a) displacement with time b) soil resistance with time

a) b)

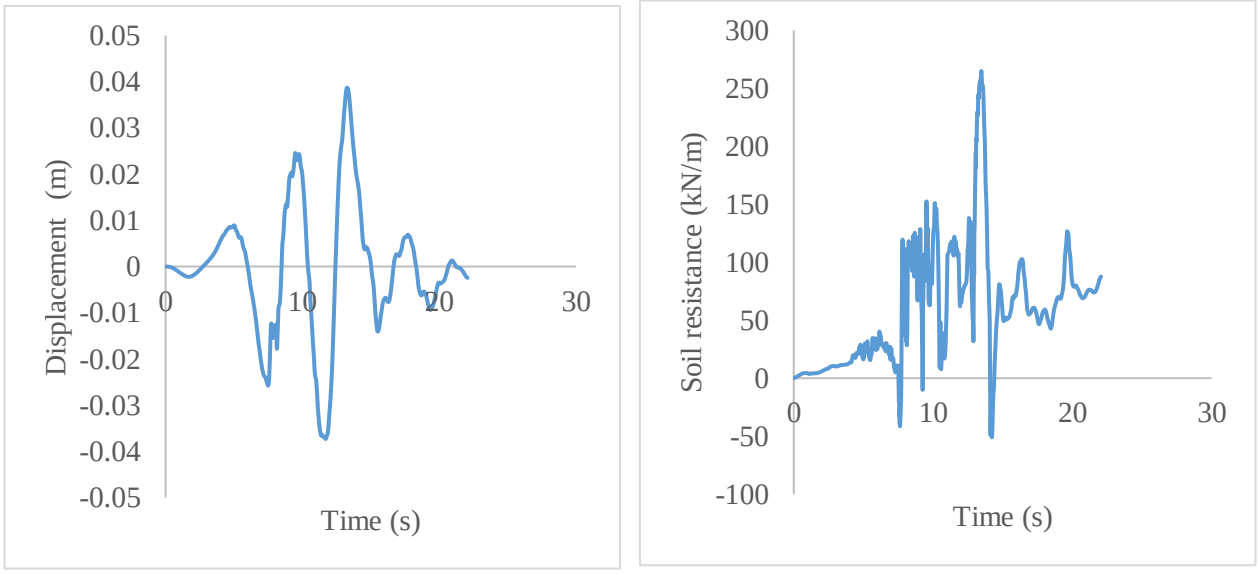

Figure 5.18: Effect of seismic load at depth 15 m a) displacement with time b) soil resistance with time

5.4.2 Displacement and Soil Resistance for Diameter 0.8 m

Figure 5.19 to 5.21 shows displacement and soil resistance with dynamic time for diameter 0.8 m by varying pile depth.

a) b)

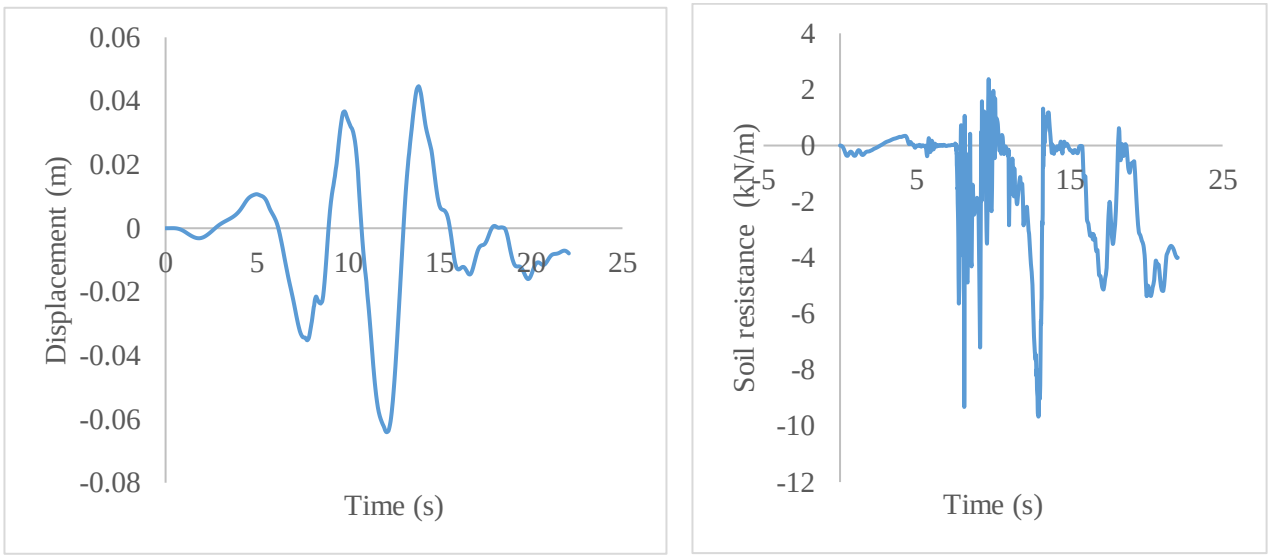

Figure 5.19: Effect of seismic load at pile head a) displacement with time b) soil resistance with time

a) b)

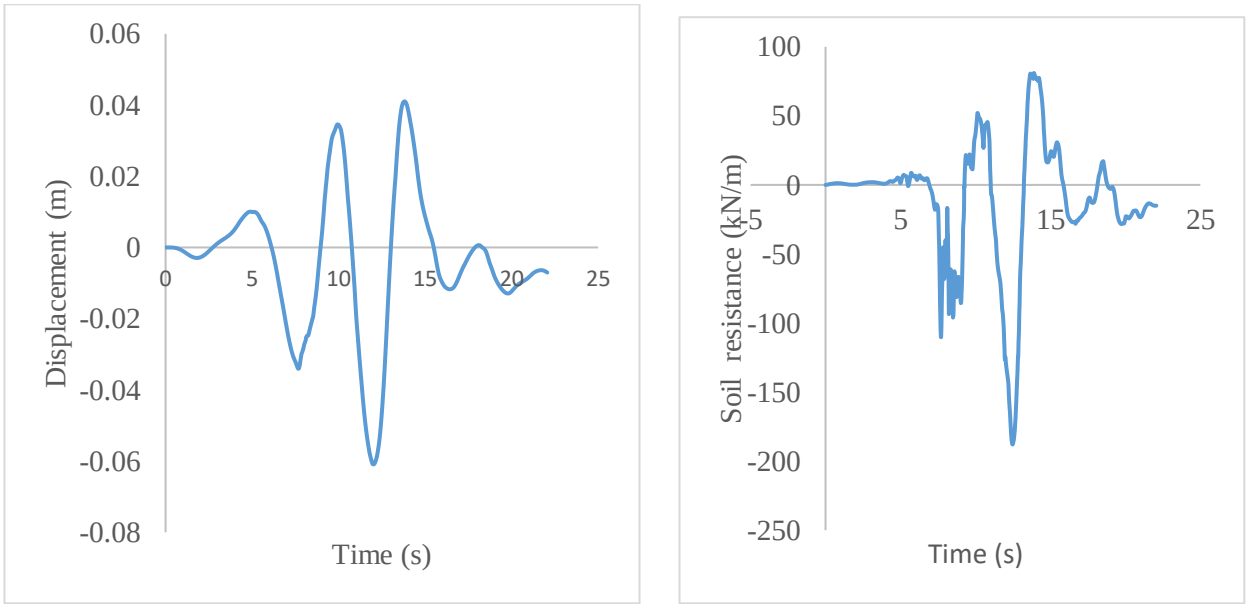

Figure 5.20: Effect of seismic load at depth 6 m a) displacement with time b) soil resistance with time

a) b)

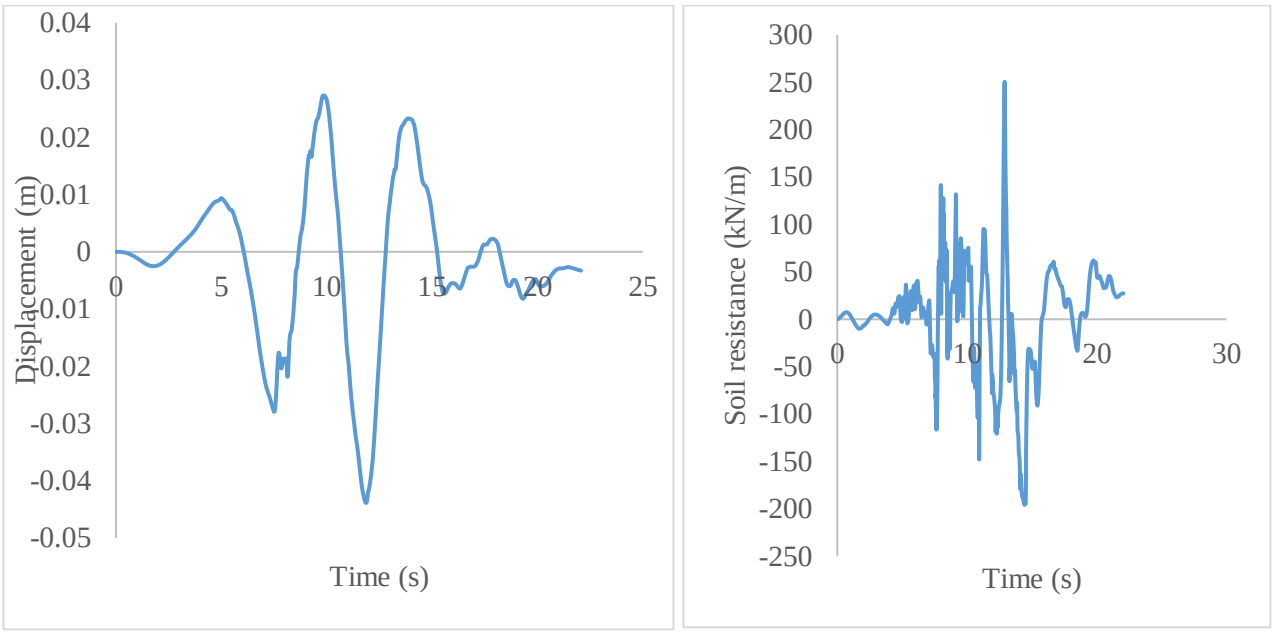

Figure 5.21: Effect of seismic load at depth 12 m a) displacement with time b) soil resistance with time

a) b)

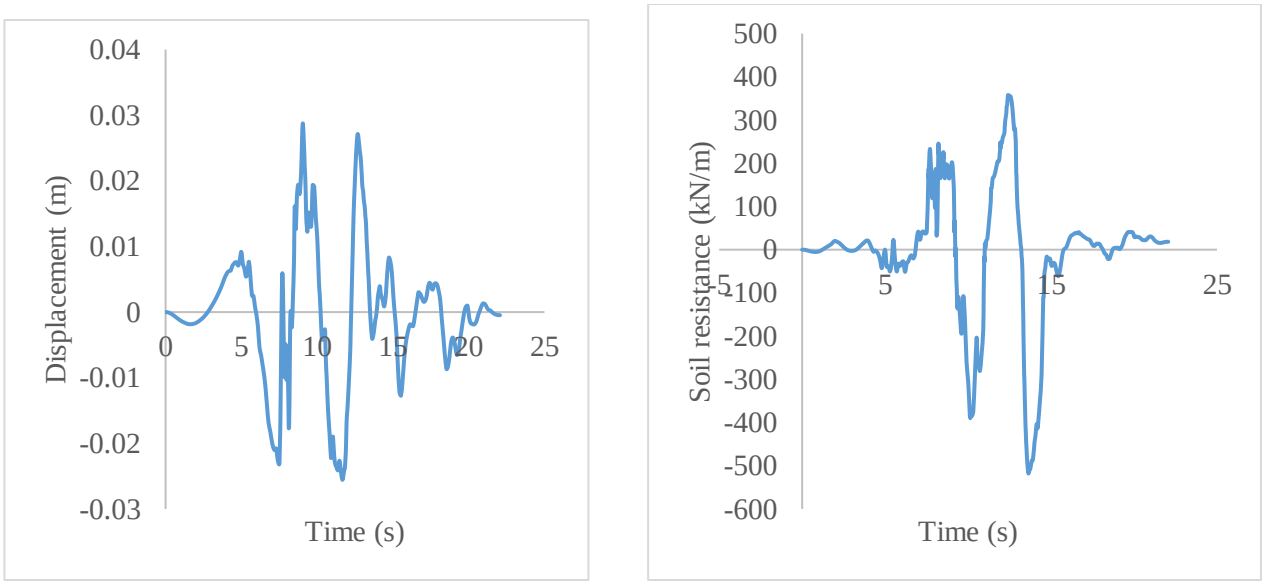

Figure 5.22: Effect of seismic load at depth 15 m a) displacement with time b) soil resistance with time

On site, the transmission tower is constructed using 0.6 m diameter pile. To assess the effect of pile size, analysis has been performed both on 0.6 m and 0.8 m diameter pile. Result shows that approximately 10 mm deflection reduction for an increase of 200 mm in pile diameter. For the load resistance, 0.8 m diameter pile shows significant increase on load resistance as compared to 0.6 m diameter of pile. Therefore, deflection and load resistance of pile show reduction and increment, respectively, along with increasing pile diameter.

CHAPTER 6 CONCLUSION AND RECOMMENDATION

6.1 Conclusion

During ground shaking, pile foundations are subjected to lateral forces. Even though the primary function of a pile foundation is to carry and transfer the vertical loads from the superstructure, it has to withstand lateral forces due to seismic actions or any other lateral forces as well. The seismic response of the soil is affected by an interaction between the structure and surrounding soil.

One of the major portions of this research is seismic hazard analysis for the specified electric converter station area. Probabilistic seismic hazard analysis has been carried out for return period of both 475 years and 2475 years. For both design basis earthquake, corresponding to 475 years of return period, and for maximum considered earthquake, corresponding to 2475 years of return period, peak ground accelerations have been calculated. 0.16g and 0.233g are the peak ground acceleration values for design basis earthquake and for maximum considered earthquake, respectively and these PGA values fall in the range of PGA values determined by Worku (2011).

In this thesis, ABAQUS software was used for three dimensional analysis of pile soil system to determiner pile response under seismic load in layered soil. The dynamic simulation systems are used to develop the response of pile under seismic excitation. Acceleration time history with duration of 22.065 seconds was used to assess the pile deflection, p-y curve pattern and kinematic effects on the pile.

The maximum deflections for diameter 0.6 m and 0.8 m pile were 72.02 mm and 63.7 mm respectively. These values exceed the recommended threshold values, which is given as 5% of pile diameter (Bouzid .et.al. ,2013). In this thesis, the reinforcements were not considered. Therefore, this much exceedance of the pile deflections might be attributed to the fact that strength from rebar has not been considered.

Deflection values of each pile at different depths decrease while going from top to bottom, as it is expected. Increasing the pile diameter by 200 mm shows reduction of 10 mm lateral deflection of pile. However, such an increase in pile size shows significant amount of increment on soil resistance.

6.2 Recommendation for Future Work

- It is recommended to use various diameter of piles for better comparison.
- It is recommended to consider large super structural load in order to see inertial effect.
- It is recommended to consider group of piles.
- It is recommended to consider the reinforcement of the pile.

CHAPTER 7 REFERENCES

ABAQUS Documentation, 2010. Dassault Systems.

Abrahamson, N. A. & Somerville, P. G., 1996. Effects of the hanging wall and footwall on the ground motions recorded during the Northridge earthquake. *Bulletin of the Seismological Society of America,* Volume 86, pp. 93-99.

Ayele, A., 2017. Probabilistic seismic hazard analysis (PSHA) for Ethiopia and neighboring region. *Journal of African Earth Sciences,* Volume 134, pp. 257-264.

Baker, J. W., 2008. *An Introduction to Probabilistic Seismic Hazard Analysis (PSHA),* s.l.: s.n.

Balendra, S., 2005. Numerical Modeling of Dynamic Soil-Pile-Structure Interaction. *Department of Civil and Environmental Engineering.*

Balendra, S., 2005. *Numerical Modeling of Dynamic Soil-Pile-Structure Interaction,* s.l.: Washington State University.

Basile, F., 2003. "Analysis and design of pile groups" extract from "Numerical Analysis and Modelling in Geomechanics". *Spon press (eds J. W. Bull), London, 2003,* Volume Chapter 10, pp. 278-315.

Ben Jamma, S. & Shiojiri, H., 2000. " A Method for Three Dimensional Interaction Analysis of Pile-Soil System in Time Domain ". *Transactions of the Japan Society for Computational Engineering and Science ,* p. Paper No.20000013.

Benjamin, J. R. & Cornell, C. A., 1970. *Probability, Statistics, and Decision for Civil Engineers.* , New York., s.n.

Bentley, K. J. & Naggar, M. H., 2000. Numerical Analysis of Kinematic Response of Single Piles. *Canadian Geotechnical Journal.*

Bhowmik, S. & Long, J., n.d. *An analytical investigation of the behavior of laterally loaded piles.* s.l., s.n., pp. 1307-1318.

Bommer, J. J. & Bommer, N. A., 2006. Why Do Modern Probabilistic Seismic-Hazard Analyses Often Lead to Increased Hazard Estimates?. Volume 96, pp. 1976-1977.

Bransby, M. F., 1999. Selection of p-y Curves for the design of single laterally loaded piles. *International Journal for Numerical and Analytical Methods In Geomechanics,* pp. 1909-1926.

Brown, D. et al., 2001. *"Static and Dynamic Lateral Loading of Pile Groups",* Washington, D.C: National Cooperative Highway Research Program , NCHRP Report 461: Transportation Research Board – National Research Council, National Academy Press.

Chiou, B. J. & Youngs, R. R., 2008. An NGA model for the average horizontal component of peak ground motion and response spectra. *Earthquake Spectra,* Volume 24, pp. 173-216.

David, R. B. & Haiganoush, K. P., 1984. An exploratory of the Joyner Borre attenuation data. *Bulletin of the Seismological Society of America,* Volume 74, pp. 1441-1450.

Desai, C. & Appel, G., 1976. *"3-D Analysis of Laterally Loaded Structures".* Blacksburg, Virginia, s.n.

Desai, C. S., Zaman, M. M., Lightner, J. G. & Siriwardane, H. J., 1984. Thin-Layer Element for Interfaces and Joints. *International Journal for Numerical and Analytical Methods in Geomechanics.*

Feng, L. B., Hong, H., Kai, M. B. & Hong, N. L., 2011. Seismic Response analaysis of transmission tower linesystem on a Heterogeneous Site to Multi-Component Saptial Ground Motions. *ResearchGate,* Volume 14(3).

Francesca , D., Sandro , C. & Graziano Leoni, 2009. Kinematic bending moment in pile foundation. *Soil Dyanmics and Earthquake Engineering.*

Gazetas, G. & Dobry, R., 1984a. "Horizontal Response of Piles in Layered Soils". *Journal of Geotechnical Engineering, ASCE,* Volume Vol. 110 (1), pp. 20-40.

Gazetas, G. & Dobry, R., 1984b. " Simple Radiation Damping Model for Piles and Footings ". *Journal of Engineering Mechanics, ASCE,* Volume Vol. 110 (6), pp. 937-956.

Hall, W. J. & Green , R. A., 1994. *An overview of selected seismic hazard analysis methodologies,* s.l.: Urbana.

Hetenyi, 1946. Beams on Elastic Foundations. *University of Michigan Press.*

Hutchinson, T., Chai, Y., Boulanger, R. & Idriss, I., 2004. " Inelastic Seismic Response of Extended Pile-Shaft-Supported Bridge Structures ". *Earthquake Spectra,EERI,* Volume Vol. 20 (4), pp. 1057-1080.

Huyse, L. C. & Stamatakos, J. A., 2003. Application of Generalized Pareto Distribution to Constrain Uncertainty in Low-Probability Peak Ground Accelerations. *Bulletin of Seismological Society of America.*

James Kaklamanos, Laurie , G. & David, M. B., 2011. Estimating Unknown Input Parameters when Implementing the NGA Ground-Motion Prediction Equations in Engineering Practice. *Earthquake Engineering Research Institute,* 27(4), p. 1219–1235.

Jeremic, B. & Preisig, M., 2005. *Nonlinear Finite Element Analysis of Dynamic Soil-Foundation-Structure Interaction..*

Julyk, L. J. et al., 1993. Continuum Soil Modeling in the Static Analysis of Buried Structures. *U.S. Department of Energy.*

Kagawa, T., 1992. “Modeling Soil Reaction to Laterally Loaded Piles”. *Transportation Research Record No 1336 – Foundations Engineering Seismic Design Drilled Shafts and other Issues,* pp. 81-89.

Kagawa, T. & Kraft, L., 1980. "Lateral Load Deflection Relationship of Piles
Subjected to Dynamic Loadings". *Soil and Foundation, Japanese Society of Soil Mechanics and Foundation Engineering,* Volume Vol. 20(4), pp. 19-35.

Kagawa, T. & Kraft, L., 1981. "Lateral Piles Response During Earthquakes". *Journal of the Geotechnical Engineering Division, ASCE,* Volume Vol. 107 (12), pp. 1713-1731.

Kijko, A., 2003. Estimation of the Maximum Earthquake Magnitude, mmax. *Pure and Applied Geophysics,* Volume 161(8), pp. 1655-1681.

Kooijman, A. & Vermeer, P., 1988. *Elastoplastic analysis of laterally loaded pile.* s.l., Proc. 6th Int. Conf. Num. Meth.Geomech., Innsbruck, pp. 1033-1042.

Kramer, S., 1996. "Geotechnical Earthquake Engineering". *Prentice-Hall:Newjersey.*

Li, H. N. & Bai, H. F., 2006. High Voltage transmission tower line system subjected to disaster loads. *Progress in Natural Science.*

Lysmer, J. & Kuhlemeyer, R. L., 1969. Finite dynamic model for infinite media. *Journal of the Engineering Mechanics Division, ASCE,* pp. 859-877.

Maheshwari, B., Truman, K., El Naggar, M. & Gould, P., 2004. Three
Dimensional Finite Element Nonlinear Dynamic Analysis of Pile Groups for Lateral Transient and Seismic Ex citations. *Canadian Geotechnical Journal,* Volume 41, pp. 118-133.

Mamoon, S. M. & Ahmad, S., 1991. *Seismic Response of Floating Piles.* s.l., University of Missouri-Rolla Publication, pp. 805-814.

Martin, J. & Perez, C. J., 2009. Application of a generalized lognormal distribution to engineering data fitting. *Researchgate.*

Matlock, H., 1970. *"Correlations for Design of Laterally Loaded Piles in Soft Clay".* s.l., s.n.

Matlock, H., Foo, S. & Bryant, L., 1978. *"Simulation of Lateral Pile Behavior".* s.l., s.n.

Mylonakis, G. & Gazetas, G., 2000. Seismic Soil-Structure Interaction Beneficial or Detrimental?. *Journal of Earthquake Engineering, 2000.*

Nogami, T. & Novak, M., 1980. "Coefficients of Soil Reaction to Pile Vibration". *Journal of Geotechnical Engineering, ASCE,* Volume Vol. 106(5), pp. 565-570.

Nogami, T. & Konagai, K., 1988. "Time Domain Flexural Response of Dynamically Loaded Single Piles". *Journal of Geotechnical Engineering, ASCE,* Volume Vol. 144(9), pp. 1512-1525.

Nogami, T., Otani, J., Konagai, K. & Chen, H. L., 1992. " Nonlinear Soil-Pile Interaction Model for Dynamic Lateral Motion". *Journal of Geotechnical Engineering, ASCE,* Volume Vol. 118(1), pp. 89-106.

Novak, M., 1974. "Dynamic Stiffness and Damping of Piles". *Canadian Geotechnical Journal,* Volume Vol. 11, pp. 574-598.

Novak, M. & Mitwally, H., 1988. Transmitting boundary for axisymmetrical dilation problems. *Journal of Engineering Mechanics, ASCE.*

Polam, I., Kapuskar, M. & Chaudhuri, D., 1998. *"Modeling of Pile Footings and Drilled Shafts for Seismic Design ",* s.l.: Buffalo: Technical Report MCEER-98-0018 .
Multidisciplinary Center for Earthquake Engineering Research , State University of New York at Buffalo.

Poulos, H. G., 2013. *Practical approaches to seismic design of deep foundations.* s.l., Proc. 19th NZGS Geotechnical Symposium.

Randolph, M., 1981. "The response of flexible piles to lateral loading". *Géotechnique,* Volume Vol.31(2), pp. 247-259.

Reese, L., Cox, W. & Koop, F., 1974. *"Analysis of Laterally Loaded Piles in Sand".* s.l., s.n., pp. 473-483.

Rodriguez, M. A. & Bray, J. D., 2005. Seismic Site Response for Near-Fault Ground Motions. *Journal of Geotechnical and Geoenvironmenatl Engineering, submitted onJournal of Geotechnical and Geoenvironmenatl Engineering, submitted on June 2005.*

Scherbaum , F., Schmedes, J. & Cotton, F., 2004. On the conversion of source-to-site distance measures for extended earthquake source models. *Bulletin of the Seismological Society of America,* Volume 94, pp. 1053-1069.

Somerville, P. G. & Abrahamson, N. A., 1995. *Prediction of Ground Motions for Thrust Earthquakes,* s.l.: Report to the California Strong Motion Instrumentation Program (CSMIP).

Song, F. J., 2018. Performance based seismic assesment of large concrete framed structure supporting multi-units of heavy compressors. *journal of Vibroengineering,* Volume 20.

Steven, L. K., Pedro , A. & Hyung, S. S., 2008. Using OpenSees for Performance-Based Evaluation of Bridges on Liquefiable Soils. *PACIFIC EARTHQUAKE ENGINEERING RESEARCH CENTER.*

Sun, Y. K. & Mintaek, Y., 2019. Evaluation of Dynamic Soil-Pile-Structure Interactive Behavior in Dry Sand by 3D Numerical Simulation. *Applied Science.*

Tajimi, H., 1966. *"Earthquake response of Foundation Structures (in Japanese) ",* s.l.: Tokyo: Faculty of Science and Engineering, Nihon University Tokyo .

Terzaghi, K., 1955. “Evaluation of Coefficients of Subgrade Reaction”. *Geotechnique,5(4),* pp. 297-326.

Vesic, A., 1961. “Bending of Beams Resting on Isotropic Elastic Solid”. *Journal of the Engineering Mechanics Division, ASCE,* Volume Vol 87(2), pp. 35-53.

Villaverde, R., 2009. Fundamental Concepts of Earthquake Engineering. *CRC Press.*

Wang , S. et al., 1998. “Nonlinear Soil-Pile Structure Interaction”. *Earthquake Spectra, EERI,* Volume Vol. 14(2), pp. 377-396.

Wells, D. L. & Coppersmith, K. J., 1994. New empirical relationships among magnitude rupture length, rupture width, rupture area, and surface displacement. *Bulletin of the Seismological Society of America,* Volume 84, p. 974–1002.

Whitman, R. V., 197. Analysis of Soil-Structure Interaction: State-of -the-Art Review. In: s.l.:Massachusetts Institute of Technology, Soils publication.

Wilson, D. W., Boulanger, R. W. & Kutter, B. L., 2000. Observed seismic lateral resistance of liquefying sand. *Journal of Geotechnical and Geoenvironmental Engineering, ASCE.*

Worku, A., 2011. Recent Developments in the definitions of design eartquake ground motion. *Journal of EEA,* Volume Vol.28.

Wu, G. & Finn, W., 1977. "Dynamic nonlinear analysis of pile foundations using finite element method in the time domain". *Canadian Geotechnical Journal,* Volume Vol.34, pp. 44-52.

Zienkiewicz, O. C., Emson, C. & Bettess, P., 1983. Novel boundary infinite element. *International Journal for Numerical Methods in Engineering,* Volume 19, pp. 393-404.

APPENDIX - A

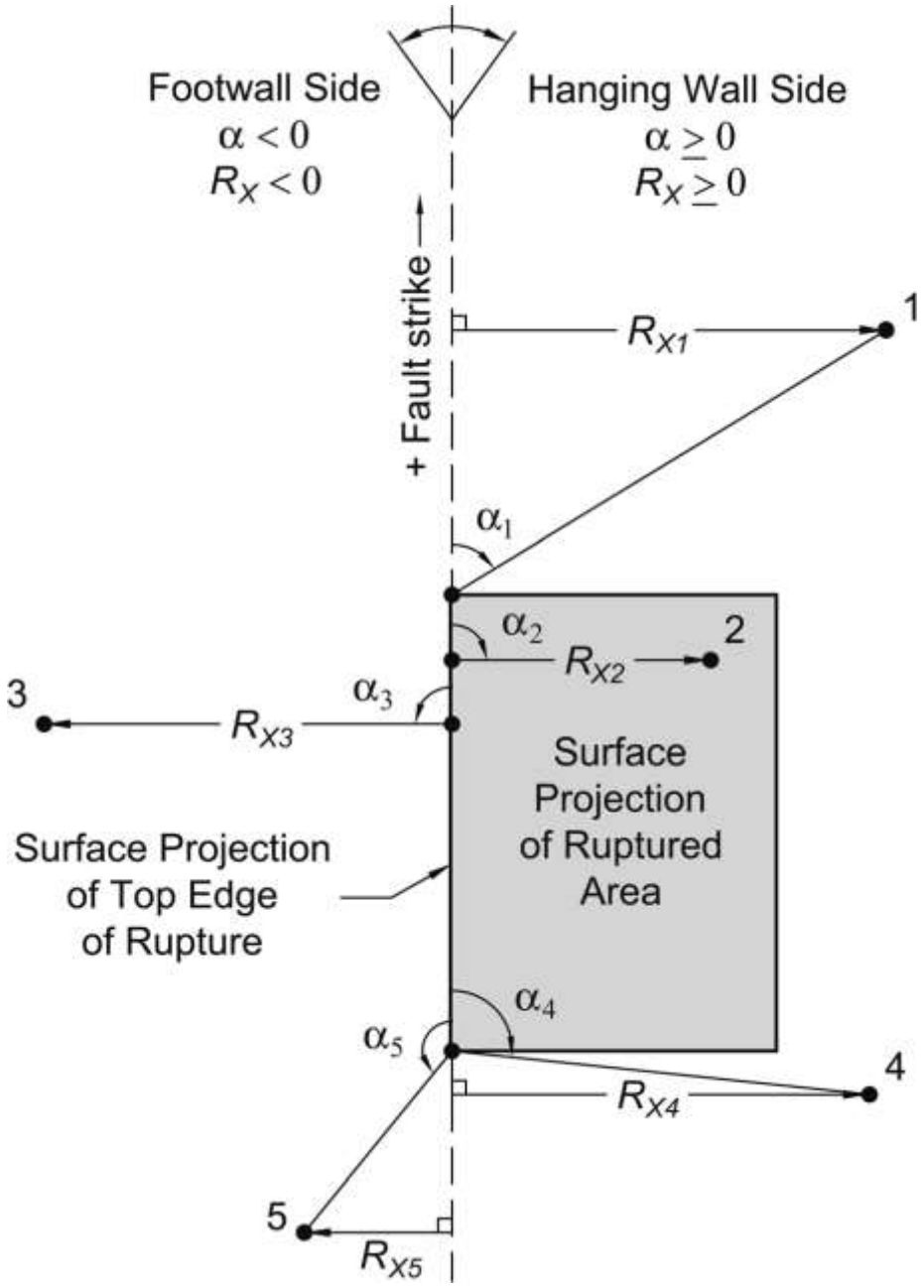

Plan view of a fault rupture, giving the definition and sign convention of the source-to-site azimuth (α).

APPENDIX - B

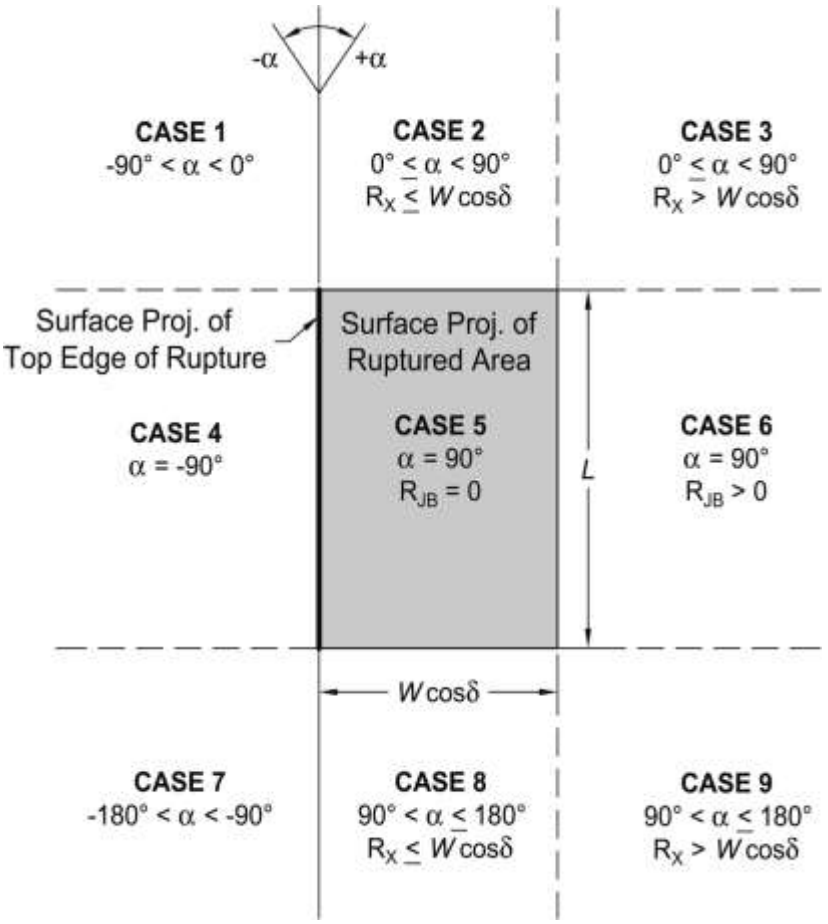

Plan view of the nine geometric cases for the location of a site with respect to the fault strike and surface projection of ruptured area, used in the calculation of RX.